IntechOpen

Solar Panels and Photovoltaic Materials

Edited by Beddiaf Zaidi

SOLAR PANELS AND PHOTOVOLTAIC MATERIALS

Edited by **Beddiaf Zaidi**

Solar Panels and Photovoltaic Materials
http://dx.doi.org/10.5772/intechopen.72061
Edited by Beddiaf Zaidi

Contributors

Tahereh Nemati Aram, Didier Mayou, Richard Corkish, Marina Monteiro Lunardi, Juan Pablo Alvarez-Gaitan, Jose I. Bilbao, Lei Zhang, Masatoshi Uno, Toru Nakane, Toshiki Shinohara, Miguel De Simon-Martin, Ana-María Diez-Suárez, Laura Álvarez-De Prado, Alberto González-Martínez, Álvaro De La Puente-Gil, Jorge Blanes-Peiró, Ming-Chung Wu, Yin-Hsuan Chang, Evgenii Terukov, Andrey Kosarev, Alexey Abramov, Eugenia Malchukova, Beddiaf Zaidi, Muhammad Burhan, Muhammad Wakil Shahzad, Kim Choon Ng

Notice

First published in London, United Kingdom, 2018 by IntechOpen
eBook (PDF) Published by IntechOpen, 2019
IntechOpen is the global imprint of INTECHOPEN LIMITED, registered in England and Wales, registration number: 11086078, The Shard, 25th floor, 32 London Bridge Street
London, SE19SG – United Kingdom
Printed in Croatia

British Library Cataloguing-in-Publication Data
A catalogue record for this book is available from the British Library

Additional hard and PDF copies can be obtained from orders@intechopen.com

Solar Panels and Photovoltaic Materials
Edited by Beddiaf Zaidi

p. cm.

Print ISBN 978-1-78923-434-3

Online ISBN 978-1-78923-435-0

eBook (PDF) ISBN 978-1-83881-647-6

Meet the editor

Dr. Beddiaf Zaidi is working as an assistant professor in the Department of Physics at the University of Batna 1. He obtained his doctorate degree in Physics at the University of Annaba in 2014. He has published a number of research papers in reputed journals and has written one book on solar cells. He acted as an editor in chief of the *International Journal of Mathematical Sciences and Applications (IJMSA)*. He is a potential reviewer for reputed journal papers. He participated in many international conferences serving as a referee, PC member, etc. He is also an editorial board member of numerous journals and a lead guest editor of many special issues.

Contents

Preface XI

Chapter 1 **Introductory Chapter: Introduction to Photovoltaic Effect 1**
Beddiaf Zaidi

Chapter 2 **A Review of Recycling Processes for Photovoltaic Modules 9**
Marina Monteiro Lunardi, Juan Pablo Alvarez-Gaitan, José I. Bilbao and Richard Corkish

Chapter 3 **Quantum Two-Level Model for Excitonic Solar Cells 29**
Tahereh Nemati Aram and Didier Mayou

Chapter 4 **Effects of the Novel Micro-Structure on the Reflectance of Photovoltaic Silicon Solar Cell 47**
Lei Zhang

Chapter 5 **From 11% Thin Film to 23% Heterojunction Technology (HJT) PV Cell: Research, Development and Implementation Related 1600 × 1000 mm2 PV Modules in Industrial Production 61**
Eugenii Terukov, Andrey Kosarev, Alexey Abramov and Eugenia Malchukova

Chapter 6 **Perovskite-Structured Photovoltaic Materials 77**
Ming-Chung Wu and Yin-Hsuan Chang

Chapter 7 **Degradation Monitoring of Photovoltaic Plants: Advanced GIS Applications 93**
Miguel de Simón-Martín, Ana-María Diez-Suárez, Laura-Álvarez de Prado, Alberto González-Martínez, Álvaro de la Puente-Gil and Jorge Blanes-Peiró

Chapter 8 **Multicell Design for Concentrated Photovoltaic (CPV) Module 111**
Muhammad Burhan, Muhammad Wakil Shahzad and Kim Choon Ng

Chapter 9 **Single-Switch Differential Power Processing PWM Converter to Enhance Energy Yield of Photovoltaic Panels under Partial Shading 131**
Masatoshi Uno, Toru Nakane and Toshiki Shinohara

Preface

Renewable energy resources and significant opportunities for energy efficiency exist over wide geographical areas in contrast to other energy sources that are concentrated in a limited number of countries. Rapid deployment of renewable energy and energy efficiency and technological diversification of energy sources would result in significant energy security and economic benefits.

Solar power is the conversion of energy from sunlight into electricity, either directly using photovoltaic (PV) or indirectly using concentrated solar power, or a combination of both. Concentrated solar power systems use lenses or mirrors and tracking systems to focus a large area of sunlight into a small beam. Photovoltaic cells convert light into an electric current using the photovoltaic effect. Photovoltaic materials include silicon (most prominent), semiconductor compounds (thin film), and combinations thereof in multi-junction cells.

We wish to thank everyone who, whether in a professional or personal field, showed patience, understanding, and helpfulness during the intensive phase of the creation of this book.

Dr. Beddiaf Zaidi
PRIMALAB Laboratory
Department of Physics
Faculty of Materials Science
University of Batna 1
Batna, Algeria

Chapter 1

Introductory Chapter: Introduction to Photovoltaic Effect

Beddiaf Zaidi

Additional information is available at the end of the chapter

http://dx.doi.org/10.5772/intechopen.74389

1. Spectral characteristics of solar radiation

Solar radiation is a radiant energy emitted by the Sun as a result of its nuclear fusion reactions. Spectral characteristics of solar radiation, both external to the Earth's atmosphere and at the ground, can be seen in **Figure 1**. Over 99% of the energy flux from the Sun is in the spectral region of 0.15–4 μm, with approximately 50% in the visible light region of 0.4–0.7 μm. The total amount of energy emitted by the Sun and received at the extremity of the Earth's atmosphere is constant, that is, 1370 W/m^2/s. The amount of energy received per unit area of the

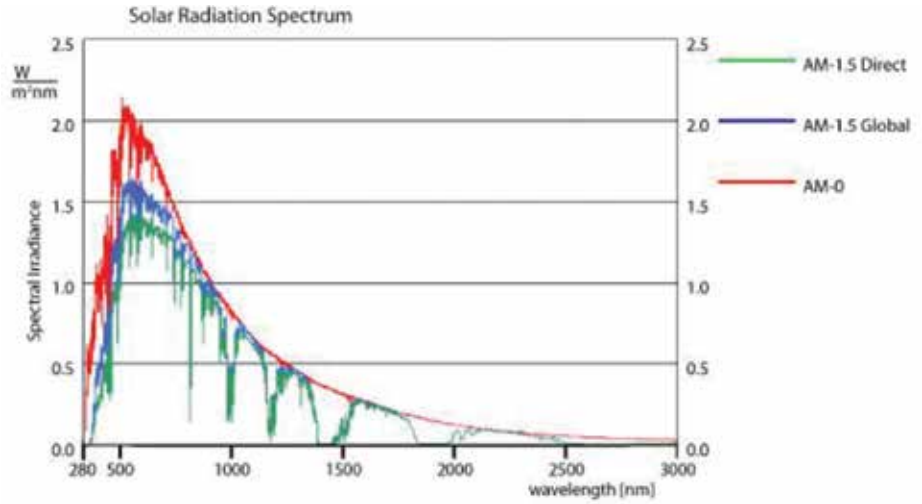

Figure 1. Spectral distribution of radiation intensity [1].

Earth's surface is 343 W/m²/s. The standard spectrum for space applications is referred to as AM_0. It has an integrated power of 1366.1 W/m². Two standards are defined for terrestrial use: (1) the $AM_{1.5}$ global spectrum is designed for flat plate modules and has an integrated power of 1000 W/m² and (2) the $AM_{1.5}$ direct spectrum is defined for solar concentrator work. It includes the direct beam from the Sun and the circumsolar component in a disk of 2.5° around the sun. The direct and circumsolar spectra have an integrated power density of 900 W/m² (**Figure 1**).

2. History of photovoltaic effect

The photovoltaic effect was discovered in 1839 by the French physicist, Alexandre Edmond Becquerel. While experimenting with metal electrodes and electrolyte, he discovered that conductance increases with illumination. Willoughby Smith discovered the photovoltaic effect in selenium in 1873. Albert Einstein described the phenomenon in 1904. The first silicon monocrystalline solar cell was constructed in 1941. In 1951, the first germanium solar cells were made. Bell's Laboratories published the results of the solar cell operation with 4.5% efficiency. The efficiency was increased to 6% within a few months. In 1957, Hoffman Electronics introduced a solar cell with 8% efficiency. A year later, in 1958, the same company introduced a solar cell with 9% efficiency. The first radiation-proof silicon solar cell was produced for the purposes of space technology in the same year. In 1960, Hoffman Electronics introduced another solar cell with 14% efficiency. In 1977, the world production of photovoltaic modules exceeded 500 kW. In 1984, ARCO Solar introduced the first amorphous modules. In 1985, researchers at the University of New South Wales in Australia constructed a solar cell with more than 20% efficiency. In 1996, BP Solar purchased APS announced a commercial CIS solar cells production. During 2000 and 2001, the production by Japanese manufacturers increased significantly.

3. Solar cell structure

When a solar cell is illuminated by sunlight, photon energy of the incident light is converted to direct current electricity through the process of photovoltaic effect of the solar cell. Incident light causes electron–hole pairs to be generated in the semiconductor, and there is an increase in the concentration of minority carriers (electrons in the p-type region and holes in the n-type region) in the depletion region. This increase in the concentration of minority carriers results in the flow of the minority carriers across the depletion region into the quasineutral regions. These photo-generated carriers cause the flow of photo-generated current. When the junction is in the open-circuit condition, no net current can flow inside the p-n junction; thus, the current resulting from the flux of photo-generated and thermally generated carriers is balanced by the opposite recombination current (**Figure 2**).

If a load is connected between the electrodes of the illuminated p-n junction, some fraction of the photo-generated current will flow through the external circuit. The potential difference between the n-type and p-type regions will be lowered by a voltage drop over the load. Also, the electrostatic potential difference over the depletion region will be decreased, which results in an increase in the recombination current [2].

http://dx.doi.org/10.5772/intechopen.74389

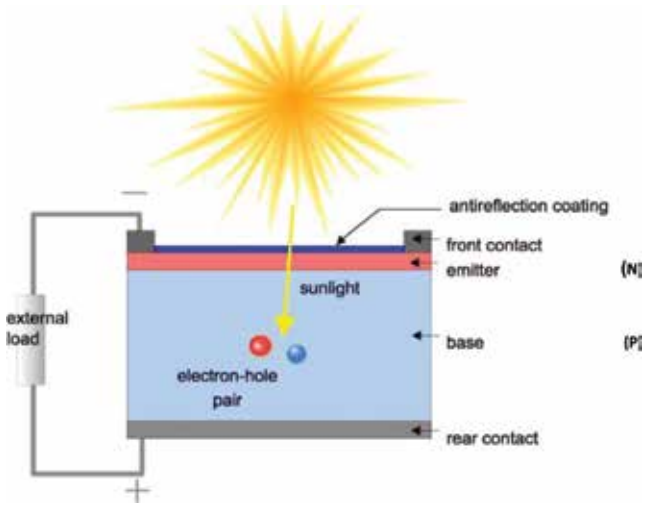

Figure 2. Incident light on a typical PN solar cell.

4. Basic structure of a solar cell

Most solar cell technologies [3] have:

- Anti-reflecting coating (ARC), which is a very important part in solar cell fabrication. It is usually sprayed over bare silicon cell because silicon has a high surface reflection.
- Front contacts that are necessary to collect the current generated by a solar cell. They are usually made of metals.
- An emitter that absorbs the incoming photons and transports their energies to the excited state of charge carries. Pentavalent-doped silicon (n-type) has a higher surface quality than trivalent doped silicon (p-type), so it is placed at the front of the cell, where majority of the light is absorbed.
- In p-n junction, in its simplest form, the base (p-type) region is joined at a junction with emitter (n-type) region leading to majority electrons in the n-type side close to the junction to diffuse of to the p-type side and majority hole from the p-type to diffuse n-type side.
- Rear contact is a less important than the front contact because it is much way from the junction and does not need to be transparent.

5. Equivalent circuit of a solar cell

To understand the electronic behavior of a solar cell, it is useful to create a model, which is electrically equivalent and is based on discrete electrical components whose behavior is well known. An ideal solar cell may be modeled by a current source in parallel with a diode;

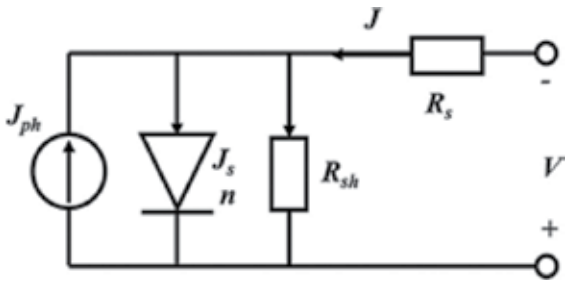

Figure 3. The equivalent circuit of a solar cell.

in practice, no solar cell is ideal, so a shunt resistance and a series resistance component are added to the model (**Figure 3**) [4, 5].

5.1. Characteristic equation

From the equivalent circuit, it is evident that the current produced by the solar cell is equal to that produced by the current source, minus that which flows through the diode, minus that which flows through the shunt resistor:

$$J = J_{ph} - J_s - J_{sh}$$

where J is the output current, J_{ph} is the photo-generated current, J_s is the diode current, and J_{sh} is the shunt current.

The current through these elements is governed by the voltage across them:

$$V_j = V + JR_S$$

where V_j is the voltage across both diode and resistor R_{sh} and V is the voltage across the output terminals.

By the Shockley diode equation, the current diverted through the diode is:

$$J_s = J_0\left[exp\left(\frac{V + J R_s}{n V_T}\right) - 1\right]$$

where J_0 is the diode reverse saturation current (A), R_S is the series resistance (Ω), R_{sh} is the shunt resistance (Ω) and n is the diode ideality factor. Here, the shunt current is:

$$J_{sh} = \frac{(V + J R_s)}{R_{sh}}$$

Combining this and above equations results in the complete governing equation for the single-diode model:

$$J = J_{ph} - J_0\left[exp\left(\frac{V + J R_s}{n V_T}\right) - 1\right] - \frac{(V + J R_s)}{R_{sh}}$$

http://dx.doi.org/10.5772/intechopen.74389

The output power is given by:

$$P = V\left(J_{ph} - J_0\left[exp\left(\frac{V + JR_s}{nV_T}\right) - 1\right] - \frac{(V + JR_s)}{R_{sh}}\right)$$

5.2. Solar cell characteristics in practice

The J-V characteristic of a solar cell in practice usually differs to some extent from the ideal characteristic. The solar cell may also contain series (R_s) and parallel (or shunt, R_p) resistances, leading to a characteristic of the form where the light-generated current J_{ph} may, in some instances, depend on the voltage, as we have already noted (**Figure 4**) [6].

5.3. Fill factor

As always in electrical engineering, optimal power output requires a suitable load resistor that corresponds to the ratio (V_m/J_m). V_m and J_m are, by definition, the voltage and current at the optimal operating point, and M_{pp} is the maximum achievable power output [7]. We now form the ratio of peak output ($V_m . J_m$) to the variable ($V_{oc}.J_{sc}$) and call this ratio the fill factor (FF) of a solar cell:

$$FF = \frac{V_m . J_m}{V_{oc} . J_{sc}}$$

5.4. Efficiency

The efficiency of a solar cell is defined as the ratio of the photovoltaic-generated electric output of the cell to the luminous power falling on it [8]:

$$\eta = \frac{V_m . J_m}{P_{light}} = \frac{FF . V_{oc} . J_{sc}}{P_{light}}$$

The silicon solar cells have dominated the PV market for so many years. They have been produced to be used for both research and commercial purposes. They have dominated the

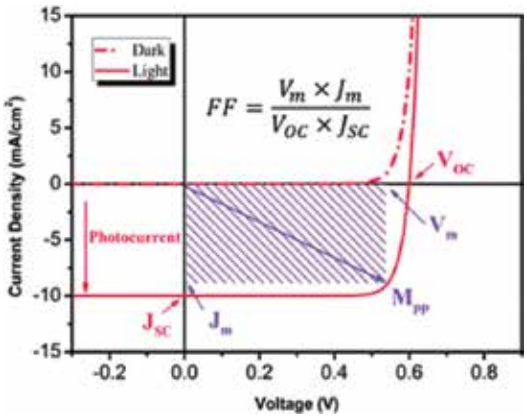

Figure 4. The superposition principle for solar cells.

Cell	Area (cm^2)	V_{oc} (v)	J_{sc} (mA/cm^2)	FF (%)	η (%)
c-Si	143.7	0.740	41.8	82.7	25.6 ± 0.5
Poly-Si	243.9	0.663	39.03	80.3	20.8 ± 0.6
a-Si:H	1.001	0.896	16.36	69.8	10.2 ± 0.3
CIGS/CdS	0.988	0.752	35.3	77.2	20.5 ± 0.6
CdTe/CIS	1.062	0.876	30.25	79.4	21.0 ± 0.4
Organic	0.993	0.793	19.40	71.4	11.0 ± 0.3

Table 1. Current operational data of compared technologies based on modules.

market because of the abundance of silicon, nontoxicity, module efficiency, and excellent cell stability. There are various levels of skills for production of the evaluated technologies (monocrystalline [9], polycrystalline [10–13], amorphous [14], and inorganic and organics cells). The current operating data of the evaluated cells in their module state are compared in **Table 1**. These data were measured under the global AM1.5 spectrum (1000 W/m^2) at 25°C.

Author details

Beddiaf Zaidi

Address all correspondence to: zbeddiaf@gmail.com

PRIMALAB Laboratory, Department of Physics, Faculty of Material Sciences, University of Batna 1, Batna, Algeria

References

[1] Luque S et al. Handbook of Photovoltaic Science and Engineering. Chichester: John Wiley and Sons; 2003

[2] Tang Y et al. N+ emitters realized using Ammonium Dihydrogen Phosphate for silicon solar cells. Solar Energy. 2013;**95**:265-270

[3] Wolf S, et al. Towards industrial application of isotropic texturing for multi-crystalline silicon solar cells. Proc. of the 16th European PV Solar Energy Conference. Glasgow, United Kingdom. 2000

[4] Zaidi B et al. Simulation of single-diode equivalent model of polycrystalline silicon solar cells. International Journal of Materials Science and Applications. 2018;**7**:8-10

[5] Sze SM. Semiconductor Devices. New York: John Wiley; 1981

[6] Zaidi B et al. Matlab/Simulink based simulation of monocrystalline silicon solar cells. International Journal of Materials Science and Applications. 2016;**5**:11-15

[7] Honsberg C et al. Photovoltaics: Devices, Systems and Applications [CDROM]. Sydney (Aus): University of New South Wales; 1998

[8] Zaidi B. Cellules Solaires Éditions Universitaire Européennes. 2016

[9] Beaucarne G. Silicon thin-film solar cells. Advances in Optoelectronics. 2007

[10] Zaidi B et al. Hydrogenation effect on electrical behavior of polysilicon thin films. Silicon. 2015;**7**:275-278

[11] Zaidi B et al. Effet des Traitements Thermiques sur le Comportement Électrique des Couches de Silicium Polycristallin pour des Applications Photovoltaïques. Revue de Métallurgie. 2011;**108**:443-446

[12] Zaidi B et al. Influence of doping and heat treatments on carriers mobility in polycrystalline silicon thin films for photovoltaic application. Turkish Journal of Physics. 2011; **35**:185-188

[13] Zaidi B et al. Optimum parameters for obtaining polycrystalline silicon for photovoltaic application. American Journal of Nanosciences. 2015;**1**:1-4

[14] Zaidi B et al. Electrical energy generated by amorphous silicon solar panels. Silicon. DOI: 10.1007/s12633-017-9555-8

Chapter 2

A Review of Recycling Processes for Photovoltaic Modules

Marina Monteiro Lunardi,
Juan Pablo Alvarez-Gaitan, José I. Bilbao and
Richard Corkish

Additional information is available at the end of the chapter

http://dx.doi.org/10.5772/intechopen.74390

Abstract

The installations of photovoltaic (PV) solar modules are growing extremely fast. As a result of the increase, the volume of modules that reach the end of their life will grow at the same rate in the near future. It is expected that by 2050 that figure will increase to 5.5–6 million tons. Consequently, methods for recycling solar modules are being developed worldwide to reduce the environmental impact of PV waste and to recover some of the value from old modules. Current recycling methods can recover just a portion of the materials, so there is plenty of room for progress in this area. Currently, Europe is the only jurisdiction that has a strong and clear regulatory framework to support the PV recycling process. This review presents a summary of possible PV recycling processes for solar modules, including c-Si and thin-film technologies as well as an overview of the global legislation. So far, recycling processes of c-Si modules are unprofitable but are likely to be mandated in more jurisdictions. There is potential to develop new pathways for PV waste management industry development and offer employment and prospects for both public and private sector investors.

Keywords: recycling, life-cycle, photovoltaic, waste, end-of-life

1. Introduction

Photovoltaic (PV) solar modules are designed to produce renewable and clean energy for approximately 25 years. The first substantial PV installations happened in the early 1990s and since early 2000s solar PV electricity distribution has grown extremely fast [1].

The cumulative worldwide PV generation capacity reached 302 GW in the end of 2016 [2] and the predominant technology (90% of the market) is crystalline silicon (c-Si) cells [3]. Also, during the last years there were several advances on renewable energy in general, including significant price decline and a constant increase in attention to environmental impacts from energy sources [4, 5]. Furthermore, the International Technology Roadmap for Photovoltaic (ITRPV) prediction for the installed PV capacity in 2050 is 4500 gigawatts [6].

As a result of the increase in the global market for PV energy, the volume of modules that reach the end of their life will grow at the same rate in the near future. At the end of 2016, the cumulative global PV waste reached 250,000 metric tons, while it is expected that by 2050 that figure will increase to 5.5–6 million tons [7].

Much PV waste currently ends up in landfill. Given heavy metals present in PV modules, e.g. lead and tin, this can result in significant environmental pollution issues. Furthermore, valuable metals like silver and copper are also present, which represents a value opportunity if they can be recovered. Hence, the landfill option cerates additional costs and it does not recover the intrinsic values of the materials present in the PV modules.

Hence, methods for recycling solar modules are being developed worldwide to reduce the environmental impact of end-of-life modules and to recover some of the value from old PV modules. However, current recycling methods are mostly based on downcycling processes, recovering only a portion of the materials and value, so there is plenty of room for progress in this area. Moreover, currently only Europe has a strong regulatory framework in place to support recycling, but other countries are starting to build specific frameworks related to PV waste. It's clear that sustainable development of the PV industry should be supported by regulatory frameworks and institutions across the globe, which is not the case at the moment. There must be adequate management policies for photovoltaic modules when they reach their end-of-life (EoL) or when they are not able to produce electricity any longer.

As mentioned above, the European Union (EU) provides a legislative framework for extended producer responsibility of PV modules in European scale through the Waste Electrical and Electronic Equipment (WEEE) Directive 2012/19/EU [8]. The main objectives of this policy are to preserve, protect and improve the quality of the environment, to protect human health and to utilize natural resources prudently and rationally. Since February 2014, the collection, transport and recycling of PV modules that reached their EoL is regulated in every EU country [8].

On the other hand, countries with fast expanding PV markets such as China [9], Japan [10], India [11], Australia [12] and USA [13] still lack specific regulations for EoL PV modules. These countries treat PV waste under a general regulatory framework for hazardous and non-hazardous solid waste or WEEE. However, there are some exceptions.

In 2012 the Japanese government introduced a "feed-in tariff" [14] that guaranteed the rate for electricity generated from renewable energy and exported to the grid, which supported rapid growth of solar module installation in the country. Once all the installed capacity starts reaching EoL (within 20–30 years) they will create a significant waste problem for Japan. In late 2017, the Japan Photovoltaic Energy Association (JPEA) has published voluntary guidelines on how to properly dispose of EoL photovoltaic modules. Also, manufacturers, importers

and distributors of photovoltaic modules have been invited to provide information on the chemical substances contained in the product and to inform the waste disposal companies. JPEA strongly recommend that industry follow the guidelines [15].

In USA, some states go beyond the Resource Conservation and Recovery Act which regulates hazardous and non-hazardous waste management [13]. California, for example, has additional threshold limits for hazardous materials classification based on the Senate Bill 489 that categorizes end-of-life PV modules as Universal Waste (facilitating easy transport). This bill is currently pending United States Environmental Protection Agency approval [16].

In Australia, governments have recognized the significance of guaranteeing that regulations are in place to deal with the PV waste issue. Ministers agreed that the state of Victoria would lead innovative programs that seek to reduce the environmental impacts caused throughout the lifecycle of photovoltaic systems. These efforts are part of an industry-led voluntary product management arrangement to address the potential emerging risks of PV systems and their waste. PV modules are listed under the National Product Administration Act to signal the intention to consider a scheme to deal with such waste [17].

The non-inclusion of PV residues in waste legislation in some countries is due to different reasons. Solar modules have a lifespan of up to 25–30 years [18] and so there has been limited interest in investigating the aspects of EoL so far. Moreover, the quantity of this type of waste is still considered insignificant compared to the quantity of other WEEE [19], which currently makes setting up specific recycling plants for solar modules uneconomical. In addition, the definition of mandatory requirements for EoL treatment could still be an obstacle to the effective acceptance of these recycling processes [20]. Because of that, there should be a continuous focus on scientific evidences on the potential impacts and benefits related to the treatment of photovoltaic residues.

Furthermore, recycling processes for all the different PV technologies are not yet well developed. The processes are well developed for mono or multicrystalline silicon. FirstSolar [21] has an established recycling process for CdTe, but for other thin films there are still room for improvements. and are being tested and for generation 3 (new materials [22]) the recycling technologies are not well developed yet.

Only about 10% of PV modules are recycled worldwide. The main reason for that is the lack of regulation. Actually, it has been shown that, for the current recycling technologies, silicon-based modules do not have enough valuable materials to be recovered and the cost of the recycling process is always higher than the landfill option (not considering the externalities), making recycling an economically unfavorable option [23]. However, the prediction for 2050 is that the recoverable value could cumulatively exceed 15 billion US dollars (equivalent to 2 billion modules, or 630 GW) [7]. In addition, the recycling of solar PV modules can ensure the sustainability of the long-term supply chain [24], thereby increasing the recovery of energy and embedded materials and, also, reducing CO_2 emissions and energy payback time (EPBT) related to this industry.

For years, the PV industry and researchers have worked intensively in search of different types of efficient and cost-effective materials to manufacture solar PV modules and specific ways of

keeping them adequately bonded to withstand several years of outdoor exposure. The modules are made to minimize the amount of moisture that can come in contact with the solar cells and their contacts while keeping manufacturing costs down. The current standard c-Si module is bonded using two layers of EVA to bond the layers together. Because of that, recycling solar modules is a relatively complex task, since these materials need to be separated. Once the materials/layers of a solar module can be separated, metals such as lead, copper, gallium, cadmium, aluminum and silicon can be recovered and reused in new products.

Originally created by PV CYCLE in 2007 and commercially available in Europe, the process of recycling mono or multicrystalline silicon modules begins with the separation of the aluminum frame and the junction boxes and then a mechanical process is used for the extraction of the remaining materials of the module (a process similar to recycling of glass or electronic waste). The problems with this process are that the value of the material recovered is low (as it is a downcycling process) and that the maximum amount of recovered materials is about 80%, which is not sufficient for future requirements, and the value of recovered materials is smaller than the original [25]. Thin film processes are under development or near implementation in Italy, Japan and South Korea but costs are not yet competitive. Even up to 90% recovery of materials is not sufficient when compared to production costs [26]. Lastly for recycling processes aiming to generate new materials, the aim is to keep the materials intact for reuse or direct recycling, recovering the frame, glass, tabbing and solar cells without breakages and in good condition. The recovery rates can achieve up to 95% and the materials recovered have higher commercial value. However, these processes are complex and are currently just at laboratory scale, being studied by a few research groups [27].

Even with the difficulty of recovering rare, toxic and valuable materials from solar modules, the recycling process has a remarkable environmental advantage [28]. Nevertheless, the need to recycle this type of waste is imminent. The better knowledge of these technologies and growth on the waste amounts that could generate profitable outcomes has supported the development of the first PV recycling plants. Hence, PV manufacturing companies (e.g. First Solar, Pilkington, Sharp Solar, and Siemens Solar) are investing in the research on solar modules at EoL [29].

The challenges to design the ideal PV recycling process are many. The focus should be on the avoidance of damage to the PV cells and module materials, economic feasibility, and high recovery rate of materials that have some monetary value or are scare or are hazardous, that can be reused in the supply chain. Finally, the next step for the industry and researchers is to create module designs that are “recycling-friendly” [29].

2. Photovoltaic technologies

2.1. Crystalline silicon technology

Crystalline Si (c-Si) technologies dominate the current market share of PV modules (more than 90%). The aluminum back surface field (Al-BSF) [30] is the current industry standard technology

but the passivated emitter and rear cell (PERC) [31] is gaining importance in the world market and is expected to replace the Al-BSF technology in the future [3]. The heterojunction (HIT) cells are also expected to gain some space with predictions of 15% of the total market share by 2027 [7]. Besides that, Si-based tandem solar technologies are expected to appear in mass production after 2019 [7].

There are different cell structures for crystalline silicon-based PV cells [32]. The cells are electrically interconnected (with tabbing), creating a string of cells in series (60 or 72 cells are standard numbers used) and assembled into modules to generate electricity (**Figure 1**).

A typical crystalline silicon (c-Si) PV module contains approximately 75% of the total weight is from the module surface (glass), 10% polymer (encapsulant and backsheet foil), 8% aluminum (mostly the frame), 5% silicon (solar cells), 1% copper (interconnectors) and less than 0.1% silver (contact lines) and other metals (mostly tin and lead) [33]. The rest of the components have a small percentages of the module weight [29, 34].

The EU directive [8] established recycling targets in terms of module weight and also expresses the intention to increase the collection rates to allow the progressive recycling of more material and less to be landfilled. Even with targets aiming for 65% recycling product weight, some of the current studied recycling processes can recycle over 80% of the weight of a PV module (**Figure 2**). However there is still incentive to improve, considering that most of the weight is from glass and frame, which are relatively easy to remove, depending on the recycling process.

2.2. Thin-film technologies

Thin-films represent less than 10% of the total PV industry [3]. The currently dominant technologies are cadmium telluride (CdTe), copper indium gallium selenide (CIGS) and amorphous silicon (a-Si) with, approximately, 65%, 25% and 10% of the total thin-film market share, respectively [35].

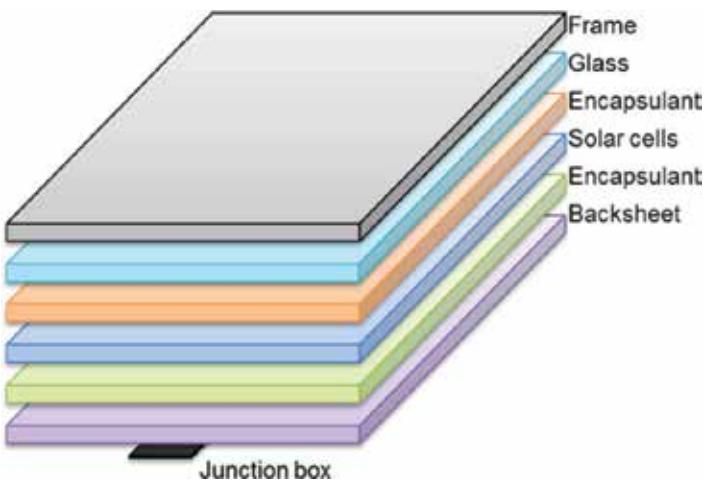

Figure 1. Silicon solar module basic structure [32].

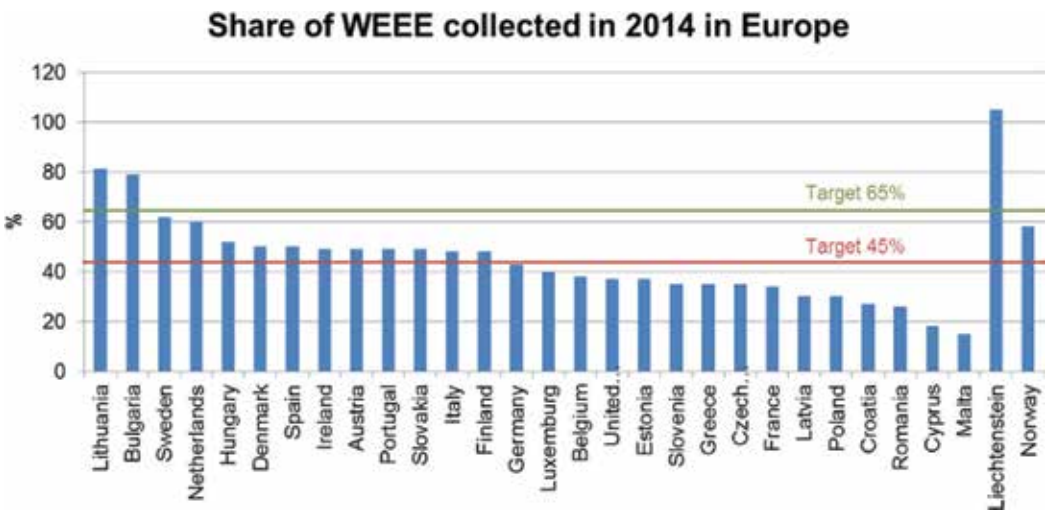

Figure 2. Total collection rate for WEEE in 2014 as a percentage of the average weight of EEE put on the market in the three preceding years (2011–2013) [8].

Thin-film solar cells were developed with the aim of providing low cost and flexible geometries, using relatively small material quantities. CdTe, CIGS and a-Si are the main technologies for thin-film PV modules [36]. CdTe is the most widely used thin-film technology. It contains significant amounts of cadmium (Cd), an element with relative toxicity, which presents an environmental problem that has been studied worldwide [37, 38]. CIGS has a very high optical absorption coefficient because it is a direct band gap material (can be tuned between 1.0 and 2.4 eV by varying the In/Ga and Se/S ratios [39]) and efficiency of approximately 15.7 $\pm$ 0.5% for high bandgap [40]. A-Si has low toxicity and cost but also low durability and it is less efficient compared with the other thin-film technologies [41]. Current projections expect the a-Si module market to disappear in the near future, since they cannot compete on costs or efficiency [3].

Basically, thin-film modules consist of thin layers of semiconducting material (CdTe, CIGS or a-Si) deposited on a substrate (glass, polymer or metal) (**Figure 3**).

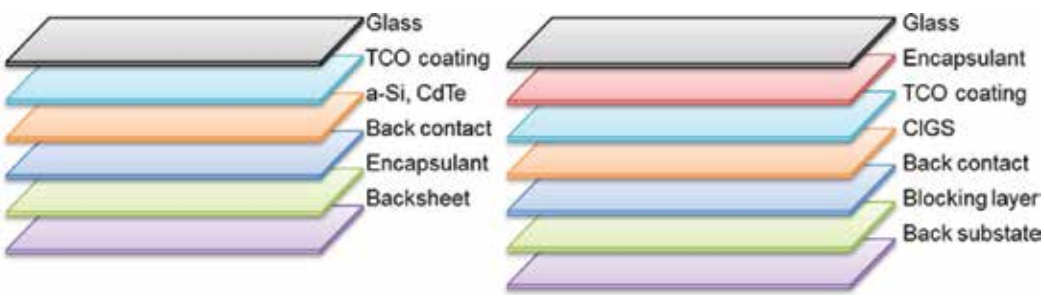

Figure 3. Thin-film solar module basic structures [36].

3. Photovoltaic recycling technologies

PV modules are largely recyclable. Materials such as glass, aluminum and semiconductors can, theoretically, be recovered and reused. Hence it is vital that consumers, industry and PV producers take responsibility for the EoL of these modules. So far, the most common methods for recycling c-Si PV modules are based on mechanical, thermal and chemical processes.

Although thin-film solar cells use far less material than c-Si cells, there are concerns about the availability and toxicity of materials such as tellurium (Te), indium (In), and cadmium (Cd), for example. Furthermore, the production processes also generates greenhouse gases emissions during some reactor-cleaning operations. Because of these issues, it is very important to focus on the recycling of PV modules for all the technologies.

PV Cycle is a not-for-profit organization which goal is to manage PV waste through their waste management programme for solar PV technologies [42]. PV Cycle was the first to establish a PV recycling process and PV waste logistics throughout the EU. In 2016 their process of recycling PV achieved a record recycling rate of 96% for c-Si PV modules (fraction of solid recycled) [25], which is a percentage that surpasses the current European WEEE standards. The process begins with the removal of the cables, junction box and frame from the PV module. Then, the module is shredded, sorted and separated. The separation of the materials allows them to be sent to specific recycling processes associated with each material. The summary of this process is shown in **Figure 4**.

FirstSolar [21] developed a recycling process for CdTe modules. The company manages the collection and transportation of EoL modules to the recycling centre; however, the recycling process itself must be financed. This is made by setting aside funds by the company itself at the time of the module sale, which also happens with WEEE. The summary of this process is shown in **Figure 5**.

The recycling process starts with the shredding of the modules into large pieces and subsequently in to small fragments (5 mm or less) by a hammer mill. During the next 4–6 h the semiconductor films are removed in a slow leaching drum. The remaining glass is exposed to a mixture of sulfuric acid and hydrogen peroxide aiming, to reach an optimal solid–liquid ratio. After that process, the glass is separated again. The next step is to separate the glass from the larger ethylene vinyl acetate (EVA) pieces, via a vibrating screen. The glass is cleaned and sent to recycling. Sodium hydroxide is used to precipitate the metal compounds, after which they are sent to another company where they can be processed to semiconductor grade raw materials for use in new solar modules. This process recovers 90% of the glass for use in new products and 95% of the semiconductor materials for use in new solar modules [21].

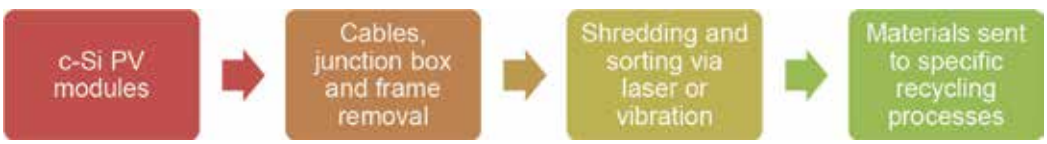

Figure 4. Summary of PV cycle recycling process for c-Si modules [25].

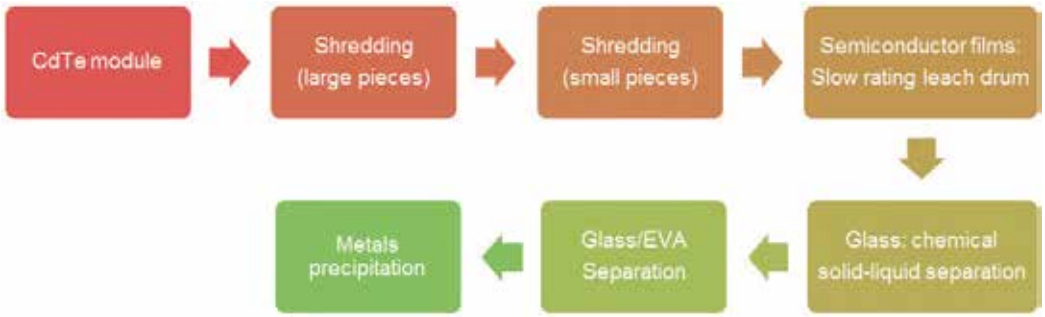

Figure 5. Summary of first solar recycling process for CdTe modules [21].

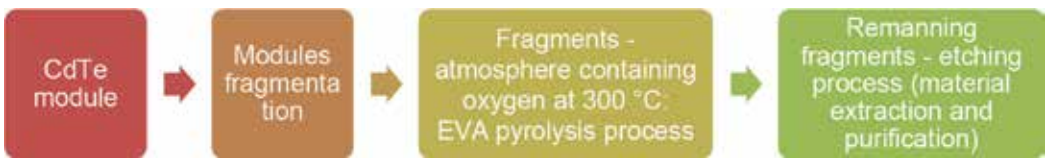

Figure 6. Summary of ANTEC solar GmbH recycling process for CdTe modules [43].

Also, for recycling CdTe modules, ANTEC Solar GmbH designed a pilot plant with a similar technology to the First Solar process. It starts with a physical fragmentation of the modules. After that, these small pieces are exposed to an atmosphere containing oxygen at 300°C. These conditions result in the delamination of the EVA. Subsequently, these fragments are taken to a 400°C atmosphere containing chlorine gas which causes an etching process. This step of the process generates $CdCl_2$ and $TeCl_4$ that are condensed and precipitated afterwards [43]. The summary of this process is shown in **Figure 6**.

A company that has a well stablished c-Si recycling process is the SolarWorld [44]. This company started recycling in 2003 with a pilot plant using a thermal process. Today, the take-back of modules is organized via a "bring-in" system [44]. Their process is based on a thermal process, which starts by pyrolising the modules. During this process, the plastic components are burnt at 600°C. The solar cells, glass and metals are separated manually after that. The glass and some metals are sent to other companies for recycling and the solar cells can be turned into wafers again. The outcomes of this process are the recovery of more than 84% of the module weight, being 90% of the glass and 95% of the semiconductor materials [44]. This process can recover up to 98% unbroken cells depending on the conditions of the module and the thickness of the cells. The summary of this process is shown in **Figure 7**.

A pilot project was funded by the Japanese Government via the New Energy and Industrial Technology Development Organization (NEDO). The recycling process for Si or CIS is based on pyrolysis of the polymers in a furnace. The process starts with the removal of the frames and the backsheet foil before the thermal process begins. After that, for CIS only, the EVA resin

Figure 7. Summary of SolarWorld recycling process for Si modules [44].

Figure 8. Summary of NEDO recycling process for Si modules (pilot project).

Figure 9. Summary of "hot knife" recycling process for PV modules [46].

is burned and the CIS layer is grated. For the c-Si modules, the semiconductor materials are recovered as well as the glass cullet [45]. The summary of these processes is shown in **Figure 8**.

In 2014 the Environment Ministry of Japan, through NEDO, together with private companies, began working on new technologies to pry the PV modules apart. The new technology appeared to solve a clear problem, the firm attachment of the glass and the cells to the EVA, and the consequent difficulty to separate them simply by smashing them to pieces and sorting them out [46].

NPC incorporated is one of the companies that make solar module recycling equipment. The process, called the "hot knife method", can separate the cells of a module from the glass in about 40 seconds. It places the module between two rollers, which move it along and hold it steady until it runs into a 1 meter-long steel blade ("hot knife") that is heated to 180–200°C and slices the cell and the glass apart (**Figure 9**) [46].

In Japan, the scrap glass can be sold for 0.5–1 Yen/kg. At that price, the 10–15 kg of glass in a solar module is worth about 15 Yen (approximately 0.14 US D). Their goal was to develop a recycling technology that can cost less than 5 yen/watt (1000 yen for a 200-watt module, not including transportation cost) by the end of April 2018, which they already did by January 2018 [46].

Furthermore, some innovative treatment processes for recycling PV solar modules have been developed.

Loser Chemie has some collection points from where they gather several types of photovoltaic systems (c-Si, CdTe, CIGS and GaAs). The company has developed and patented original

Figure 10. Summary of loser Chemie recycling process for PV modules (pilot project).

processes using mechanical and chemical treatment to recycle solar cells [47]. The first step is to crush and separate the materials mechanically. In the next stage, they use chemical treatment to recover the semiconductor metals. After that, the aluminum metallisation is also recovered and can be used for producing wastewater treatment chemicals as aluminum oxide [47]. The summary of these processes is shown in **Figure 10**.

Reclaim PV has teamed up with major solar module manufacturers who distribute in Australia and is refining its processes. The company is developing a process of reclaiming efficient cells from damaged solar modules. Their cell recycling system is able to extract efficient components (but not unbroken cells) from end-of-life solar modules in order to develop new green products or be reintroduced into the PV industry as new solar modules [48].

4. Photovoltaic recycling technologies studied worldwide

Table 1 summarizes the recycling possibilities for silicon solar modules, as well as the advantages and disadvantages of each process.

Studies show that the impurity levels are an important issue during the recycling processes. For example, high temperature thermal processes and mechanical processes can create impurities. Also, low temperature processes that are used with specific mechanical or chemical steps can generate impurities as well. Hence, the ideal outcome can only be achieved with a combination of thermal, chemical or metallurgical steps [29, 61]. Once materials can be recovered without impurities, then they will have a higher market value, which is one of the main obstacles to the growth of the PV recycling industry with the current technologies.

An overview of possible thin-film recycling processes is show in **Table 2**.

The large-scale recycling of thin-film PV modules is well advanced and, as well as the Si solar cells, thin-film PV modules are currently processed and recycled using a combination of mechanical and chemical treatments to achieve meaningful outcomes.

Process	Advantages	Disadvantages	Status	Ref.
Organic solvent dissolution	• Easy access to the EVA • Less cell damage • Recovery of glass	• Delamination time depends on area • Harmful emissions and wastes	Research	[49]
Organic solvent and ultrasonic irradiation	• More efficient than solvent dissolution process • Easy access to the EVA	• Expensive equipment • Harmful emissions and wastes	Research	[50]
Electro-thermal heating	• Easy removal of glass	• Slow process	Research	[51]
Mechanical separation by hotwire cutting	• Low cell damage • Recovery of glass	• Other separation processes required for full removal of EVA	Research	[52]
Pyrolysis (conveyer belt furnace and fluidised bed reactor)	• Separate 80% of wafers and almost 100% of the glass sheets • Cost-effective industrial recycling process	• Slightly worse texturisation (damage to cell surface)	Research (pilot)	[53]
Solvent (Nitric acid) dissolution	• Complete removal of EVA and metal coating on the wafer • It is possible to recover intact cells	• It can cause cell defects due to inorganic acid • Generates harmful emissions and wastes	Research (pilot)	[54]
Physical disintegration	• Capable of treating waste	• Other separation processes required for full EVA removal • Dusts containing heavy metals • Breakage of solar cells • Equipment corrosion	Commercial	[55]
Dry and wet mechanical process	• No process chemicals • Equipment widely available • Low energy requirements	• No removal of dissolved solids	Commercial	[56]
Thermal treatment (Two steps heating)	• Full removal of EVA • Possible recovery of intact cell • Economically feasible process	• Harmful emissions • High energy requirements • Cell defects and degradation due to high temperature	Commercial	[57]
Chemical etching	• Recover high purity materials • Simple and efficient process	• Use of chemicals	Commercial	[58–60]

Table 1. Silicon solar modules recycling processes.

Process	Advantages	Disadvantages	Status	Ref.
Organic solvent dissolution	• Easy access to the encapsulant • Less cell damage • Recovery of glass	• Time for delamination depends on area • Harmful emissions and wastes	Research	[62]
Irradiation by laser	• Easy access to the encapsulant	• Slow process • Very expensive equipment	Research	[63]
Mechanical separation by hotwire cutting	• Low cell damage • Recovery of glass	• Other separation processes required for encapsulant	Research	[52]
Vacuum blasting	• Removal of semiconductor layers without chemicals • Recovery of clean glass	• Relatively slow process • Emission of metals • Further chemical/mechanical treatments	Research (pilot)	[55]
Attrition	• No usage of chemicals • Recovery of clean glass	• Further chemical or mechanical treatments needed	Research (pilot)	[55]
Flotation	• Relatively simple process • Low use of chemicals	• High losses of valuables during rinsing and sieving process • Flotation process required	Research (pilot)	[55]
Dry etching	• Simple process	• High energy demand • High effort for purification	Commercial	[43]
Physical disintegration	• Capable of treating waste	• Other separation processes required for encapsulant • Dusts containing heavy metals • Breakage of solar cells • Equipment corrosion	Commercial	[55]
Dry and wet mechanical process	• No process chemicals • Equipment widely available • Low energy requirements	• No removal of dissolved solids	Commercial	[56]
Chemical etching	• High purity materials • Simple and efficient process	• Use of chemicals	Commercial	[58–60]
Thermal treatment	• Full removal of encapsulant • Recovery of intact cell • Simple and economical	• Harmful emissions • High energy requirements • Cell defects and degradation	Commercial	[55]
Leaching	• Complete removal of metals	• High use of chemicals • Generation of acidic fumes • Complex control of chemicals	Commercial	[64]

Table 2. Thin-film solar modules recycling processes.

5. Environmental aspects

Several studies have analyzed the impacts of recycling processes for PV modules on the environment. There are advantages and disadvantages of the different methods, considering all the stages, from the collection of the PV modules to the end of the recycling process.

An environmental study made for the European Full Recovery End-of-Life Photovoltaic (FRELP) project showed that environmental impacts from c-Si recycling processes come from plastic incineration and some chemical and mechanical treatments (sieving, acid leaching, electrolysis, and neutralization) for the recovery of metals [65].

Additionally, before the recycled silicon from solar cells can be used again, further chemical treatment is necessary, as well as for silver and aluminum. The chemical treatments have the potential of producing environmental impacts. Besides that, it is important to note that no process can recycle 100% of recovered materials from solar modules yet [28].

Nevertheless, for the PV Cycle [25] c-Si recycling process it was shown that there is a significant decrease in Global Warming Potential impacts (up to 20% compared to the process of making cells) [66] and for CdTe modules, there is and environmental benefit from the glass and copper recycling [67].

When comparing c-Si recycling and landfill EoL scenarios it was found that the environmental impacts from the recycling process are lower than for landfill, assuming that the recycled resources go back to the PV cells and modules manufacturing. These results considered that the recycling process involving dismantling, remelting, thermal and chemical treatments [28].

It can be seen that there are opportunities and challenges related to PV recycling processes. Although it was already show that there are environmental benefits, the recycling methods still need to improve in order to achieve better recovery rates and work on the transportation issues.

6. Economic aspects

The recovery of valuable materials during the recycling of PV modules can have great economical value. The extraction of secondary raw material from EoL PV modules, if made in an efficient way, can make them available to the market again [68].

Attention has been paid particularly to silver. PV modules that reach their EoL will build up a large stock of embodied raw materials (as mentioned previously), which can be recovered and become available for other uses or even for solar cells again. However, this will not occur before 2025, according to some forecasts [68].

The ITRPV predicts that, by 2030, the total material value recovered from PV recycling can reach USD 450 million. With this amount it is possible to produce 60 million PV modules (18 GW), which would be approximately 33% of the 2015 production [7]. Considering Si, up to 30,000 t of silicon can theoretically be recovered in 2030 [7], which is the amount of silicon needed to produce approximately 45 million new modules. Considering a polysilicon current prices at USD 20/kg and a recovery rate from commercial recycling processes of 70% this is equivalent to USD 380 million [7].

7. Conclusions

The current study presented an overview of possible PV recycling process for solar modules, including c-Si and thin-film technologies. The motivation, legislation and current processes were discussed and possible issues were addressed.

So far, recycling processes of c-Si modules results in a net cost activity when compared to landfill (due to the avoidance of the true environmental costs and externalities for the latter) but these processes can ensure the sustainability of the supply chain in the long-term, increase the recovery of energy and embedded materials, while reducing CO_2 emissions and energy payback time (EPBT) for the whole PV industry. The unprofitability of the current methods does not mean that the recycling of PV modules should be discarded. The PV waste management has the potential to develop new pathways for industry development and offers employment prospects to investors, for both public and private sector [7].

It is well known that the recycling of EoL PV modules has positive influences on the environmental impacts. Recycling of PV modules can remove and retain potentially harmful substances (e.g. lead, cadmium, and selenium), recover rare materials (e.g. silver, tellurium and indium) and make them available for future use [8]. To achieve the best possible results at acceptable costs, it is essential that future recycling processes stay up to date on the continuous innovations in solar cells and modules technologies.

However, the current waste volumes are still low, which entails economical obstacles for the development of the existing processes. If we compare the economics of recycling electronics and telecommunications, where the profits are generated through the recovery of precious metals and parts, it is unlikely for PV solar modules to have sufficient amounts of these materials to pay for the associated costs of the steps of recycling processes [69].

It is important that specific legislation is established for PV waste management and recycling and that this step is given before the amount of waste from EoL PV modules becomes alarming, as forecast for the year 2030 [7]. Regulation will help, but it might not be the only way. The economic viability should be achieved as well. If a recycling process for PV waste that is revenue positive (i.e. a good business) can be created, then it will happen regardless of regulations.

It was shown that recycling technologies for PV wastes are extensively explored not just on labs and pilot plants, but some are also commercially available. It is also clear that a few challenges (e.g. economic feasibility, recovery of more materials, and recovery of unbroken cells), still remain in process efficiency, complexity, energy requirements and use of non-environmentally friendly materials for the treatment of some elements.

Acknowledgements

MML and RC acknowledge the support of the Australian Government through the Australian Renewable Energy Agency (ARENA). Responsibility for the views, information or advice

expressed herein is not accepted by the Australian Government. Additionally, the first author would like to acknowledge *Coordenação de Aperfeiçoamento de Pessoal de Nível Superior* (CAPES) for her scholarship.

Author details

Marina Monteiro Lunardi[1], Juan Pablo Alvarez-Gaitan[2], José I. Bilbao[1] and Richard Corkish[1]*

*Address all correspondence to: r.corkish@unsw.edu.au

1 The Australian Centre for Advanced Photovoltaics (ACAP), School of Photovoltaic and Renewable Energy Engineering, University of New South Wales, Sydney, Australia

2 School of Civil and Environmental Engineering, University of New South Wales, Sydney, Australia

References

[1] Fthenakis VM. End-of-life management and recycling of PV modules. Energ Policy. 2000; **28**(14):1051-1058

[2] IEA, PVPS. Snapshot of Global Photovoltaic Markets; 2016

[3] ITRPV. International Technology Roadmap for Photovoltaic Results 2016, 8th ed; 2017

[4] REN21. Renewables 2017 Global Status Report; 2017

[5] Green MA. Commercial progress and challenges for photovoltaics. Nature Energy. 2016; **1**:15015

[6] ITRPV Working Group. International Technology Roadmap for Photovoltaic (ITRPV); 2016

[7] Weckend S, Wade A, Heath G. End-of-Life Management Solar Photovoltaic Panels. IRENA and IEA-PVPS; 2016

[8] European Union. Directive 2012/19/EU of the European Parliament and of the Council of 4 July 2012 on Waste Electrical and Electronic Equipment (WEEE). Official Journal of the European Union. 2012:L 197/38-71

[9] State Council of the People's Republic of China. Waste Electrical and Electronic Products Recycling Regulations; 2011

[10] Ministry of Economy Trade and Industry (METI); Ministry of Environment (MOE), Guidelines on End-of-Life Management of PV Modules. Japan; 2015

[11] Ministry of Environment, Forest and Climate Change. Solid Waste Management Rules and Hazardous and Other Wastes (Management and Transboundary Movement) Rules, India, 2016

[12] The Australian Government. Product Stewardship Act 2011; 2017

[13] The United States Congress. Resource Conservation and Recovery Act of 1976; 1976

[14] Muhammad-Sukki F, Abu-Bakar SH, Munir AB, Yasin SHM, Ramirez-Iniguez R, McMeekin SG, et al. Feed-in tariff for solar photovoltaic: The rise of Japan. Renewable Energy. 2014;**68**:636-643

[15] JPEA. Guidelines for Proving Information for Proper Treatment of Used Solar Cell Modules; 2017

[16] State of California. USA. Senate Bill No. 489 - Hazardous Waste: Photovoltaic Modules; 2015

[17] Perinotto T. 12 Agenda Items from State and Territory Enviro Pollies and why they Matter. The Fifth Estate; 2017

[18] Granata G, Pagnanelli F, Moscardini E, Havlik T, Toro L. Recycling of photovoltaic panels by physical operations. Solar Energy Materials and Solar Cells. 2014;**123**:239-248

[19] Monier V, Hestin M. Study on photovoltaic panels supplementing the impact assessment for a recast of the WEEE directive. Final Report, ENV G. 2011;**4**:6

[20] Weckend S, Wade A, Heath G. End-of-Life Management Solar Photovoltaic Panels. IRENA and IEA-PVPS; 2016

[21] FirstSolar. 2017. Available from: http://www.firstsolar.com/. [Accessed: 03-01-2018]

[22] Bakhiyi B, Labreche F, Zayed J. The photovoltaic industry on the path to a sustainable future–Environmental and occupational health issues. Environment International. 2014; **73**:224-234

[23] Sener C, Fthenakis V. Energy policy and financing options to achieve solar energy grid penetration targets: Accounting for external costs. Renewable and Sustainable Energy Reviews. 2014;**32**:854-868

[24] Bustamante ML, Gaustad G. Challenges in assessment of clean energy supply-chains based on byproduct minerals: A case study of tellurium use in thin film photovoltaics. Applied Energy. 2014;**123**:397-414

[25] Cycle P. Breakthrough in PV Module Recycling Brussels2016 [updated February 18th, 2016. Available from: http://www.pvcycle.org/press/breakthrough-in-pv-module-recycling/. [Accessed: 30-01-2018]

[26] Office AB. Start of Examinations for Recycling Solar Panels 2017 [Available from: https://www.asiabiomass.jp/english/topics/1510_01.html. [Accessed: 30-01-2018]

[27] Kadro JM, Pellet N, Giordano F, Ulianov A, Müntener O, Maier J, et al. Proof-of-concept for facile perovskite solar cell recycling. Energy & Environmental Science. 2016;**9**(10): 3172-3179

[28] Huang B, Zhao J, Chai J, Xue B, Zhao F, Wang X. Environmental influence assessment of China's multi-crystalline silicon (multi-Si) photovoltaic modules considering recycling process. Solar Energy. 2017;**143**:132-141

[29] Sander K, Politik I. Study on the Development of a Take Back and Recovery System for Photovoltaic Products; 2007

[30] Narasinha S, Rohatgi A. Optimized aluminum back surface field techniques for silicon solar cells. Photovoltaic Specialists Conference, 1997, Conference Record of the Twenty-sixth IEEE: IEEE; 1997. pp. 63-6

[31] Green MA. The passivated emitter and rear cell (PERC): From conception to mass production. Solar Energy Materials and Solar Cells. 2015;**143**:190-197

[32] Ranjan S, Balaji S, Panella RA, Ydstie BE. Silicon solar cell production. Computers and Chemical Engineering. 2011;**35**(8):1439-1453

[33] Carol Olson BG, Goris M, Bennett I, Clyncke J. Current and future priorities for mass and material in silicon PV module recycling. EUPVSEC 2013, Paris; 2013

[34] Wambach K, Müller A, Alsema E, editors. Life cycle analysis of a solar module rec ycling process. 20th European Photovoltaic Solar Energy Conference, Barcelona, Spain; 2005

[35] Fraunhofer Institute for Solar Energy Systems I. Photovoltaics Report Available from: www.ise.fraunhofer.de2017 [Accessed: 12-06-2017]

[36] Green MA. Thin-film solar cells: Review of materials, technologies and commercial status. Journal of Materials Science: Materials in Electronics. 2007;**18**(1):15-19

[37] Raugei M, Isasa M, Palmer PF. Potential Cd emissions from end-of-life CdTe PV. International Journal of Life Cycle Assessment. 2012;**17**(2):192-198

[38] Fthenakis V, Moskowitz P. Thin-film photovoltaic cells: Health and environmental issues in their manufacture use and disposal. Progress in Photovoltaics: Research and Applications. 1995;**3**(5):295-306

[39] Polman A, Knight M, Garnett EC, Ehrler B, Sinke WC. Photovoltaic materials: Present efficiencies and future challenges. Science. 2016;**352**(6283):aad4424

[40] Green MA, Emery K, Hishikawa Y, Warta W, Dunlop ED. Solar cell efficiency tables (version 48). Progress in Photovoltaics: Research and Applications. 2016;**24**(7):905-913

[41] Wronski CRC, David E. Amorphous silicon solar cells. In: Archer M, Hill R, editors. Clean Electricity from Photovoltaics. 2001

[42] PV CYCLE - The World of PV Cycle. 2016. Available from: http://www.pvcycle.org/. [Accessed: 20-06-2017]

[43] Campo MD, Bonnet D, Gegenwart R, Beier J. Process for recycling CdTe/Cds thin film solar cell modules. US Patent # 6,572,782; 2003

[44] SolarWorld. 2017. Available from: https://www.solarworld.de/en/home/. [Accessed: 20-06-2017]

[45] Komoto K, editor. Developments on PV Recycling in Japan. 24th European Photovoltaic Solar Energy Conference. Hamburg; 2014

[46] Tomioka O. Japanese companies work on ways to recycle a mountain of solar panels. Nikkei Asian Review. 17 Nov. 2016. Available from: https://asia.nikkei.com/magazine/20161117-INCOMING/Tech-Science/Japanese-companies-work-on-ways-to-recycle-a-mountain-of-solar-panels. [Accessed: 14-02-2018]

[47] Palitzsch W, Loser U. Integrierte Wiederverwendung von Hightech-und Greentech-Abfällen. In: Strategische Rohstoffe—Risikovorsorge. Springer; 2014. pp. 173-181

[48] Reclaim PV. 2014. Available from: http://reclaimpv.com/. [Accessed: 20-06-2017]

[49] Maurer A, Schlummer M. Good as new-recycling plastics from WEEE and packaging wastes. Waste Management World. 2004:33-44

[50] Kim Y, Lee J. Dissolution of ethylene vinyl acetate in crystalline silicon PV modules using ultrasonic irradiation and organic solvent. Solar Energy Materials and Solar Cells. 2012; **98**:317-322

[51] Doni A, Dughiero F, editors. Electrothermal Heating Process Applied to c-Si PV Recycling. Photovoltaic Specialists Conference (PVSC), 2012 38th IEEE; 2012

[52] Yu SR. Improvement on recycling process and life cycle assessment of photovoltaic panel. Proceedings of the EcoDesign 2013 International Symposium; 2013 4–6 December 2013. Jeju, Korea

[53] Frisson L, Lieten K, Bruton T, Declercq K, Szlufcik J, De Moor H, et al. editors. Recent improvements in industrial PV module recycling. 16th European Photovoltaic Solar Energy Conference; 2000

[54] Bruton T, Scott R, Nagle J, Man M, Fackeral A, editors. Recycling of high value, high energy content components of silicon PV-modules. 12th European Photovoltaics Conference, Amsterdam; 1994

[55] Berger W, Simon F-G, Weimann K, Alsema EA. A novel approach for the recycling of thin film photovoltaic modules. Resources, Conservation and Recycling. 2010;**54**(10):711-718

[56] Krueger L, editor Overview of first solar's module collection and recycling program. 1st International Conference on PV Module Recycling; 2010

[57] Wang TY, Hsiao JC. Recycling of materials from silicon base solar cell module. Photovoltaic Specialists Conference (PVSC), 2012 38th IEEE; 2012

[58] Klugmann-Radziemska E, Ostrowski P, Drabczyk K, Panek P, Szkodo M. Experimental validation of crystalline silicon solar cells recycling by thermal and chemical methods. Solar Energy Materials and Solar Cells. 2010;**94**(12):2275-2282

[59] Kang S, Yoo S, Lee J, Boo B, Ryu H. Experimental investigations for recycling of silicon and glass from waste photovoltaic modules. Renewable Energy. 2012;**47**:152-159

[60] Palitzsch W, Loser U, editors. A new and intelligent de-Metalization step of broken silicon cells and silicon cell production waste in the recycling procedure of crystalline Si modules. Photovoltaic Specialists Conference (PVSC), 37th IEEE; 2011

[61] Latunussa C, Mancini L, Blengini G, Ardente F, Pennington D. Analysis of Material Recovery from Silicon Photovoltaic Panels. Luxembourg: Publications Office of the European Union; 2016

[62] Doi T, Tsuda I, Unagida H, Murata A, Sakuta K, Kurokawa K. Experimental study on PV module recycling with organic solvent method. Solar Energy Materials and Solar Cells. 2001;**67**(1):397-403

[63] Huot J-Y, Suys M, editors. Recycling of solar Thin Film PV modules and scraps, and closed-loop use of metals. Innovation Forum for Life-Cycle Strategies and Recycling of Scarce Metals of Strategic Importance; 2011

[64] Marwede M, Berger W, Schlummer M, Mäurer A, Reller A. Recycling paths for thin-film chalcogenide photovoltaic waste–Current feasible processes. Renewable Energy. 2013;**55**: 220-229

[65] Latunussa CE, Ardente F, Blengini GA, Mancini L. Life cycle assessment of an innovative recycling process for crystalline silicon photovoltaic panels. Solar Energy Materials and Solar Cells. 2016;**156**:101-111

[66] Cucchiella F, Rosa P. End-of-life of used photovoltaic modules: A financial analysis. Renewable and Sustainable Energy Reviews. 2015;**47**:552-561

[67] Perez-Gallardo J, Azzaro-Pantel C, Astier S. A multi-objective framework for assessment of recycling strategies for photovoltaic modules based on life cycle assessment. Waste and Biomass Valorization. 2017:1-13

[68] Perez-Santalla M. Silver Use: Changes & Outlook, 2013 Available from: www.bullionvault.com/gold-news/silver-use-103020132. [Accessed: 30-01-2018]

[69] D'Adamo I, Miliacca M, Rosa P. Economic feasibility for recycling of waste crystalline silicon photovoltaic modules. International Journal of Photoenergy. 2017;**2017**. Article 4184676; https://doi.org/10.1155/2017/4184676

Chapter 3

Quantum Two-Level Model for Excitonic Solar Cells

Tahereh Nemati Aram and Didier Mayou

Additional information is available at the end of the chapter

http://dx.doi.org/10.5772/intechopen.74996

Abstract

While improving the performance of excitonic solar cells (XSCs) has been a central effort of the scientific community for many years, theoretical approaches facilitating the understanding of electron-hole interaction, recombination and electron-phonon coupling effects on the cell performance are still needed. We present a novel simple model which is based on the quantum scattering theory, in particular on the Lippmann-Schwinger equation; this minimizes the complexity of the problem while providing useful and non-trivial insight into the mechanism governing photocell operation. In this formalism, both exciton pair creation and dissociation are treated in the energy domain, and therefore there is access to detailed spectral information, which can be used as a framework to interpret the charge separation yield. Our analysis helps to optimize the charge separation process and the energy transfer in excitonic solar cells.

Keywords: quantum model, two-level system, electron-hole interaction, electron-phonon coupling, charge separation yield

1. Introduction

Excitonic solar cells have attracted a broad interest in recent years due to their potential to provide an excellent alternative to conventional Si-based photovoltaic cells. The aim of this chapter is to discuss more details of this technology, their various types, basic operation principles and important challenges. Excitonic solar cells are structures that employ organic materials (carbon-based compounds) such as small molecules, polymers or the hybrids of these material sets to absorb light and produce photovoltaic current. Carbon-based semiconductors exhibit desirable light absorption and charge creation properties with the capability of manufacturing by low-temperature processes [1–3]. According to the type of materials used in their structure, excitonic solar cells are classified into two main categories: dye-sensitized solar

cells (DSC) [4] and organic solar cells (OSC) [5] developed in single layers [6] and bi-layers [7] including planar [8] and bulk heterojunction configurations [9]. A schematic view of different excitonic solar cells is shown in **Figure 1**.

Historically, in the end of nineteenth century, by the emerging modern organic chemistry, the scientific and industrial interests in the research on organic materials enhanced. The photoconductivity phenomenon by an organic compound "Anthracene" for the first time was observed by Pochettino in 1906 [12]. Since then, it was realized that many conventional dyes such as methylene blue can show the semiconducting characteristics [13], and enormous number of organic semiconducting molecules do exist such that their electrical and optical properties can be fine-tuned to address the special applications [14]. In the 1970s, (semi)conducting polymers were discovered [15].

The first major breakthrough in the deployment of organic solar cells has been made in 1986 by Tang who developed the donor-acceptor solar cell and reported an efficiency of 1% [16]. The energy conversion efficiency of this cell was very low, but it showed a promising potential of organic photovoltaics when electron donor and acceptor molecules are used together. In 1992, Sariciftci et al. [17] displayed the photo-induced charge transfer within organic molecules that led to particular interests in OSC field. A report of 2.9%-efficient cells based on conducting organic polymers mixed with derivatives of C60 published by Yu et al. in 1995 [18] increased

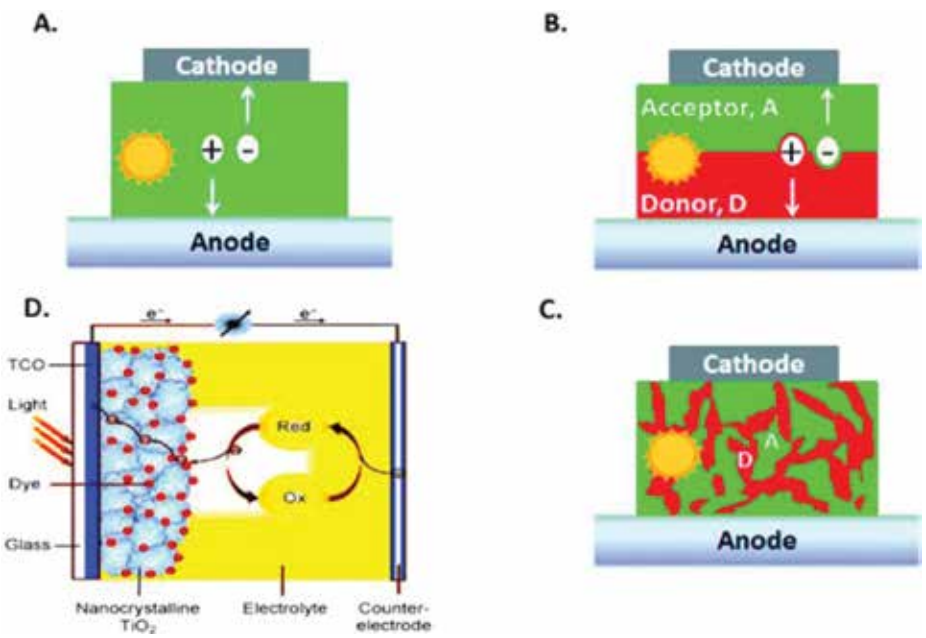

Figure 1. Different types of excitonic solar cells. (A) Single-layer OSC; (B) planar OSC; (C) bulk heterojunction OSC; (D) dye-sensitized solar cell. Figures adapted from [10, 11].

the excitement in this research area. After these achievements, the number of publications rose dramatically. Based on the aforementioned explanations, common organic solar cells use a donor and an acceptor organic material to build up a heterojunction favoring the separation of the exciton into free charge carriers. The same organic materials are also responsible for charge transport to their respective contacts. That a material for organic photovoltaic devices should have both good light absorption and carriers' transporting properties is a hard task to achieve. On the other hand, the dye-sensitized solar cell technology separates the two requirements as the charge generation is done at the interface of semiconductor dye and on the other hand, the semiconductor and electrolyte are the responsible for charge transport. Therefore, modifying the dye alone can optimize the spectral properties, while carriers' transporting properties can be improved by optimizing the semiconductor and the electrolyte phases. The first significant study of dye sensitization of semiconductors also goes back to the nineteenth century, when Vogel utilized silver halide emulsions sensitized by dyes for providing a black and white photographic film [19]. The mechanism of electron injection from photoexcited dye molecules into the conduction band of the semiconductor dates only from the 1960s [20]. The concept of dye adsorption on the surface of the semiconductor was started in 1976 by Tsubomura et al. [21] and developed in 1981 by Dare-Edwards et al. [22]. However, exploiting the dye-sensitization mechanism in photovoltaic technology was an unsuccessful process until the early 1990s when a breakthrough happened by Grätzel et al. at the EPFL. The Grätzel cell (DSC) revealed an energy conversion efficiency exceeding 7% in 1991 [23] and 10% in 1993 [24]. DSCs offer large flexibility in color, shape, and transparency [25] and perform relatively better compared with other solar cell technologies at higher temperatures [26]. Furthermore, due to the utilization of cheap and Earth-abundant materials and also simple preparation and easy fabrication processes, they are highly cost effective when compared with the conventional inorganic counterparts [27].

All the cons and pros pointed earlier make the excitonic solar cells a prospective and interesting research and innovation field. Although power conversion efficiencies (PCEs) of XSCs have represented a significant increase over the past 10 years, there are still problems in enhancing PCEs and stability to make them commercially available [28].

In 2005, the US Department of Energy published a report discussing the point that there exists insufficient microscopic intuition or theory to conduct material and device for better design of new-generation photovoltaic devices [29]. According to the mentioned report, developing theories that can provide unified, quantitative and comprehensive understanding of principle processes taking place in solar energy conversion such as photon absorption, exciton formation and dissociation, charge separation, and collection are essentially needed. Following this interesting report, here, we develop a new quantum formalism to describe the performance of excitonic solar cells in the presence of electron-hole interaction, recombination and electron-phonon coupling. This model is based on quantum scattering theory and in particular on the Lippmann-Schwinger Equation [30]. Of specific interests of the model is its development on the energy domain such that it provides detailed spectral information to interpret the exciton creation and dissociation phenomena and their effects on device properties as well.

2. Formalism and numerical methods

2.1. Two-level photovoltaic system

The basic idea of our methodology is described through the example of the two-level molecular photocell where the energy conversion process takes place in a single molecular donor-acceptor complex attached to electrodes. The two-level system is characterized by the highest occupied molecular orbital (HOMO) and the lowest unoccupied molecular orbital (LUMO). Initially, the whole system is in the ground state with filled valence bands and empty conduction bands. Following the photon absorption by the molecule, one electron and one hole are created in LUMO and HOMO, respectively. Both charge carriers interact via the Coulomb potential and can be recombined in the molecule or can be transferred to their respective channels where they produce photovoltaic current (see **Figure 2**).

Here, the first coupling energies to the charge evacuation channels are denoted by C. The hopping matrix element inside each evacuation channel is considered uniform (i.e., independent of the electron-hole positions) and denoted by J. The on-site energies of the electron at site (x) and the hole at site (y) are assumed to be $\varepsilon_e(x)$ and $\varepsilon_h(y)$, respectively. Additionally, their Coulomb-type interaction $I(x, y)$ is modeled by

$$I(x,y) = \begin{cases} U & if\, x = 0 \;\; and \;\; y = 0 \\ \frac{V}{(x+y)} & if\, x \neq 0 \;\; or \;\; y \neq 0 \end{cases} \tag{1}$$

Since $I(x, y)$ is an attractive Coulomb potential, U and V have negative values. In the above equation, U represents the strength of short-range electron-hole interaction, that is, the situation

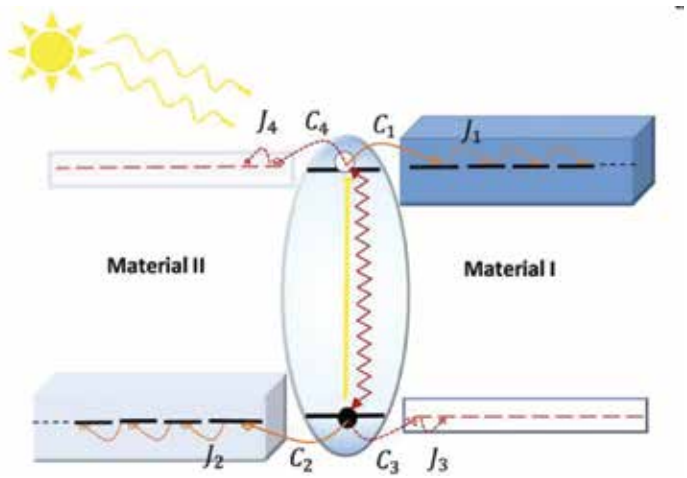

Figure 2. A molecular photocell with one HOMO and one LUMO orbital attached to the electrodes in materials I (right) and II (left). The red wiggly line represents the electron-hole interaction and recombination and the hopping integrals of electron and hole are denoted by *C* and *J*.

where both charge carriers are in the same place, that is, the absorber molecule. Furthermore, V is the strength of long-range electron-hole interaction, that is, the situation where at least one of the charge carriers is in its respective lead. It has to be noted here that this form of interaction is suitable for the mono-channel configuration where photo-generated electron and hole are directed toward different evacuation channels.

2.2. The electron-hole pair Hamiltonian

The effective Hamiltonian of the system is of the tight-binding type

$$H = \sum_i \varepsilon_i |i\rangle\langle i| + \sum_{i,j} J_{i,j} |i\rangle\langle j| \tag{2}$$

Here, the first term indicates the total on-site energy of each electron-hole basis state which is defined as a summation over the electron on-site energy, the hole's on-site energy, and the Coulomb interaction energy between them:

$$\varepsilon(x, y) = \varepsilon_e(x) + \varepsilon_h(y) + I(x, y) \tag{3}$$

The second term in Eq. (2) represents the coupling energy between two adjacent basis states. In the other words, coupling represents either the hoping of a hole or of an electron from a given initial site of the electron-hole pair to a neighboring site. As pointed earlier, the coupling energies between molecular states and their first neighbors are taken to be different from the other coupling energies.

2.3. Fluxes & quantum yield

In this formalism, we consider a photovoltaic cell as a system submitted to an incident flux of photons and assume that the whole system (PV cell plus electromagnetic field) is in a stationary state that obeys the fundamental Lippmann-Schwinger Equation [31–34]. By applying quantum scattering theory, in particular the Lippmann-Schwinger equation, the photovoltaic system is described by a wave function. The incoming state of the theory $|\Phi_{inc}\rangle$ represents the photon field with the PV cell in its ground state. By the dipolar interaction between the photovoltaic system and the electromagnetic field, this incident state $|\Phi_{inc}\rangle$ is coupled to a state where one photon is absorbed and one electron-hole pair is created. Based on the Lippmann-Schwinger equation, the total wave function of the system with incident photons of energy E is:

$$|\psi(E)\rangle = |\Phi_{inc}\rangle + G_0 V |\psi(E)\rangle \tag{4}$$

The second term in the right-hand side of the above equation is called the scattered wave function, $|\psi_p(E)\rangle = G_0 V |\psi(E)\rangle$, which represents the charge carriers photo-generated by absorption of a photon with energy E and plays an important role in this formalism. Knowing $|\Psi_p(E)\rangle$ enables one to compute all the essential fluxes to describe the photocell operation. The main three fluxes are the following: (1) the flux of absorbed photons $\Phi_{Ph}(E)$, which is

the number of absorbed photons per unit time, (2) the fluxes of electron-hole pairs that recombine in the molecule $\Phi_R(E)$, and (3) the flux of pairs whose escape from the molecule results in the photovoltaic current $\Phi_C(E)$. The determination of these quantities gives access to a detailed analysis of the photovoltaic cell performance. The yield $Y(E)$ of the photocell at a given photon energy E is proportional to the ratio of photo-generated electrons or holes that arrive at the electrodes and the total number of absorbed photons at this given energy.

$$Y(E) = \frac{\Phi_C(E)}{\Phi_{Ph}(E)} \tag{5}$$

The average yield or in other words the charge separation yield, Y, which is the proportion of all electron-hole pairs, generated by different photons and giving rise to the photovoltaic current, can be defined as:

$$Y = \frac{\Phi_C}{\Phi_{Ph}} = \int n(E)Y(E)dE \tag{6}$$

where $n(E)$ is the local density of states which is related to the flux of absorbed photons through Fermi's golden rule [31].

3. Results and discussions

3.1. Two-level systems with local interaction

Relying on the new formalism described in the previous section, here we are going to investigate the effects of short-range electron-hole interaction on the performance of a molecular photocell. The short-range interaction term implies that interaction between the electron and the hole occurs only when they both are inside the absorber molecule. To simplify the discussion, only mono-channel configuration, where there is just one possible evacuation channel for each charge carrier (i.e., $C_1 \,\&\, C_2 \neq 0$), is considered. The discussion later could be generalized to cover the multi-channel configuration; interested readers are referred to [32].

3.1.1. Local density of states

For the numerical simulations, we use $J_1 = J_2 = J = 0.2eV$ and $\Delta = 0.2eV$; therefore, the energy continuum lies between 1.2 and 2.8 ev. The energy continuum is the possible energy states of the independent electron-hole pairs far from the two-level system.

The total energy continuum is simply the sum of the electron and hole energies. In **Figure 3**, the LDOS is plotted as a function of the absorbed photon energy. In these plots, the dependence of LDOS on short-range interaction energy (U), strength of coupling parameters (C), and recombination rate (Γ_R) is examined. As can be seen from panels (a) and (b), for a given set of coupling parameters and in the absence of recombination, the number of LDOS peaks is dependent on the interaction strength. For small values of $|U|$, there is a single peak which tends to become

http://dx.doi.org/10.5772/intechopen.74996

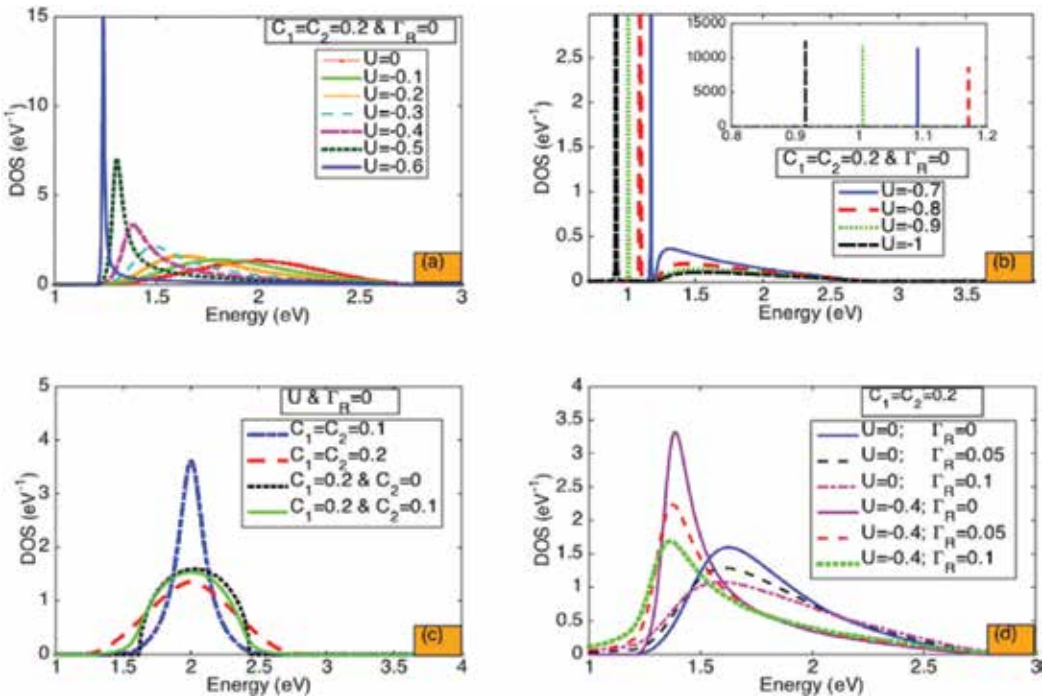

Figure 3. Local density of states as a function of incident photon energy in a mono-channel system under different conditions. ((a) and (b)) for different values of interaction energy (U); (c) for different coupling parameters (C_1 & C_2); and (d) for different interaction energies and recombination rates (U & Γ_R).

narrower for larger $|u|$. This peak appears at an energy $E_{res} \simeq \varepsilon_e(0) + \varepsilon_h(0) - U$. Indeed, E_{res} is the energy at which photons are most easily absorbed. The peak eventually splits into two for growing values of $|u|$ and the resulting two peaks separate further with increasing $|u|$ as depicted in panel (b). The narrow peak outside the continuum is called excitonic state, which blocks the charge carrier injection to the energy continuum. Next, we study the effects of the coupling parameters. The corresponding LDOS is shown in panel (c). As discussed, increasing C enhances charge carrier transfer from HOMO and LOMO to the respective evacuation channels; it can be detected through the extended width of the LDOS line shape. In both cases, the effect of Γ_R is to slightly shift the LDOS peak to the left and slightly broaden the line shape width.

3.1.2. Charge separation yield

The other important quantity that can be investigated is the charge separation yield, Y, which is computed as an average over all the absorbed photon energies.

The dependence of the charge separation yield of the interacting electron-hole pair is examined as a function of short-range interaction strength U and recombination rate Γ_R, for different coupling parameters C. As shown in **Figure 4**, in all cases, for small values of interaction energy, the yield remains 1 for $\Gamma_R = 0$. The effect of Γ_R and U is to reduce the yield. The behavior can be understood based on the spectral information provided in **Figure 3**. For larger values

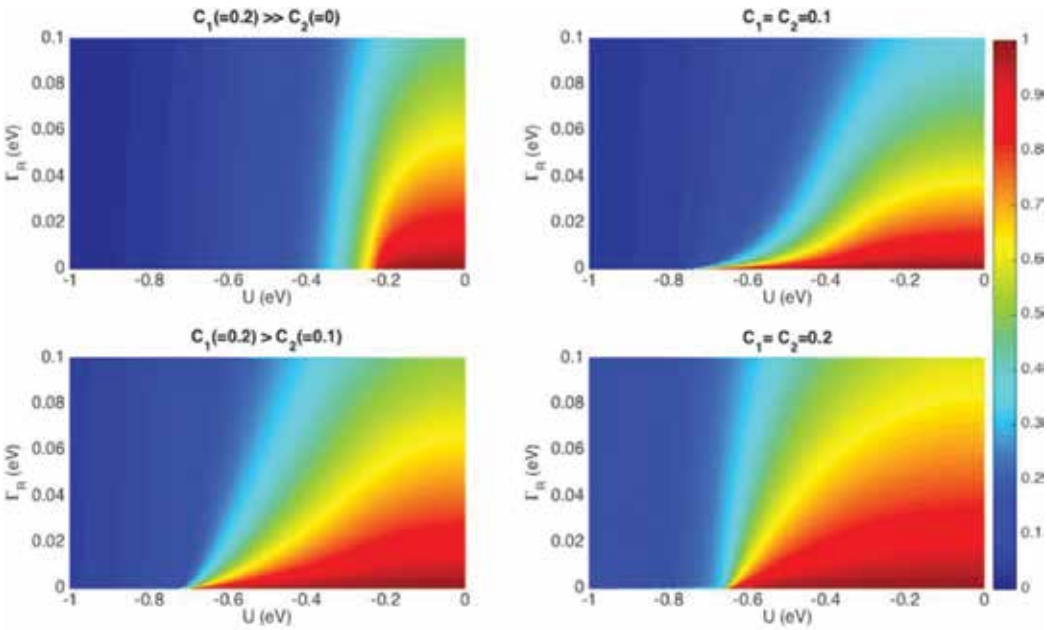

Figure 4. Photovoltaic yield as a function of interaction energy (U) and recombination rate (Γ_R) in a mono-channel system for different values of coupling parameters (C_1 and C_2).

of $|U|$, the charge carriers will stay on the molecule to form a localized state because their energy does not lie in the energy continuum of the contacts. Besides, for large values of the coupling parameters (C_1 and C_2), more charge carriers will transfer to the evacuation channels and hence the cell remains efficient over a wider range of the recombination parameter.

3.2. Two-level systems with non-local interaction

This section is intended to investigate the effects of non-local interaction on the performance of photovoltaic cells. This means that in contrast to the results presented in the previous section there are interactions even if the charge carriers are outside the molecule. An important case of non-local interaction is the long-range Coulomb interaction between the photo-generated electron and hole. This means that the electron and the hole do interact even if they are not both inside the molecule. Here of course the Coulomb interaction is not the bare interaction but is screened by all the charges of the materials around the electron-hole pair. This screening effect is well represented by considering an effective dielectric constant of the medium. The other case of non-local interaction is the coupling between the electron (or the hole) with the lattice distortion around it when the electron (or the hole) moves out of the initial two-level system. The first part of this section is devoted to the long-range Coulomb interaction case and the second part deals with the coupling to the optical phonon modes.

3.2.1. Long-range electron: hole Coulomb interaction

Similar to the previous section, we consider the mono-channel case where there is only one evacuation channel for each charge carrier. We analyze photon absorption, energy conversion

and quantum yield of the molecular photocell by considering the effects of long-range electron-hole interaction and non-radiative recombination.

3.2.1.1. Local density of states

For the numerical simulation, the same parameters as in the previous section are used. In all the calculations, C stands for the first coupling parameters and we treat the symmetric condition, that is, $C = C_1 = C_2$.

In **Figure 5**, the LDOS is plotted as a function of the absorbed photon energy. In these plots, the dependence of LDOS on short- and long-range interaction energy (U and V) and strength of coupling parameters (C) is examined. Here, the coupling parameter related to the panels of top and bottom rows is $C = 0.1\,eV$ and $C = 0.2\,eV$, respectively. As shown, under the influence of the long-range interaction, a series of excitonic peaks appears outside the energy continuum, below the lower band edge. This was expected, as it is known that the long-range Coulomb interaction creates localized states. It should be noted that upon increasing the interaction strength, the total weight of excitonic states increases. Furthermore, in all cases, as the coupling parameter increases, the width of the LDOS peak inside the energy continuum increases as well.

3.2.1.2. Charge separation yield

The dependence of the charge separation yield of the interacting electron-hole pair is examined as a function of U and Γ_R for different coupling parameters C and long-range electron-hole

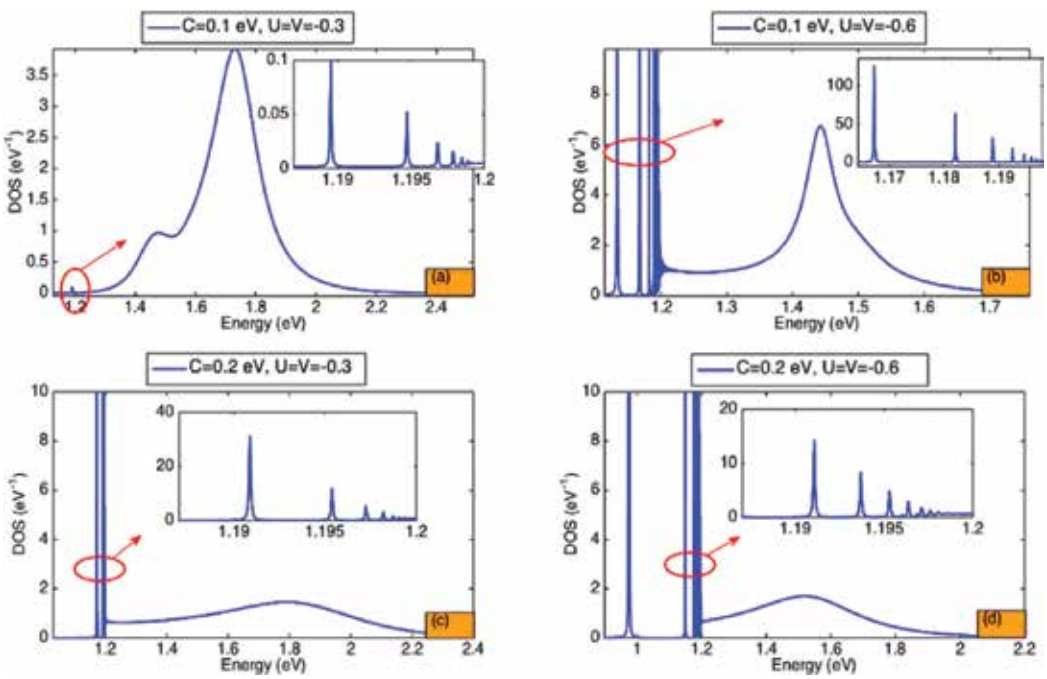

Figure 5. LDOS as a function of the energy of the absorbed photon. The impact of the coupling parameter C and the strength of the electron-hole interaction U & V are illustrated in the various panels.

interaction strength V (see **Figure 6**). The coupling parameters in the panels of left and right columns are $C = 0.1\,eV$ and $C = 0.2\,eV$, respectively. As shown, upon increasing interaction strength inside the molecule (U), less charge carriers exit through the contacts because of localized state formation and hence the yield decreases. The interesting point is that in the case of $U = V$, the effect of the Coulomb interaction is to diminish the global potential nearly uniformly, which has a small effect on the localization of the electron-hole pair. Therefore, the maximum of the charge separation yield is at $U \simeq V$. In panels (a) and (b) where the effect of the long-range interaction has been neglected, the maximum in the charge separation yield is at $U = 0\,eV$; in the other panels, as a consequence of the electron-hole long-range interaction ($V \neq 0\,eV$), the maximum of the yield is at lower values of the interaction energy.

Additionally, for a given coupling parameter, the yield is higher for weakly interacting electron-hole pairs. This behavior can be understood based on the spectral information provided in **Figure 5**; explicitly under the influence of the strong interaction, the weight of localized

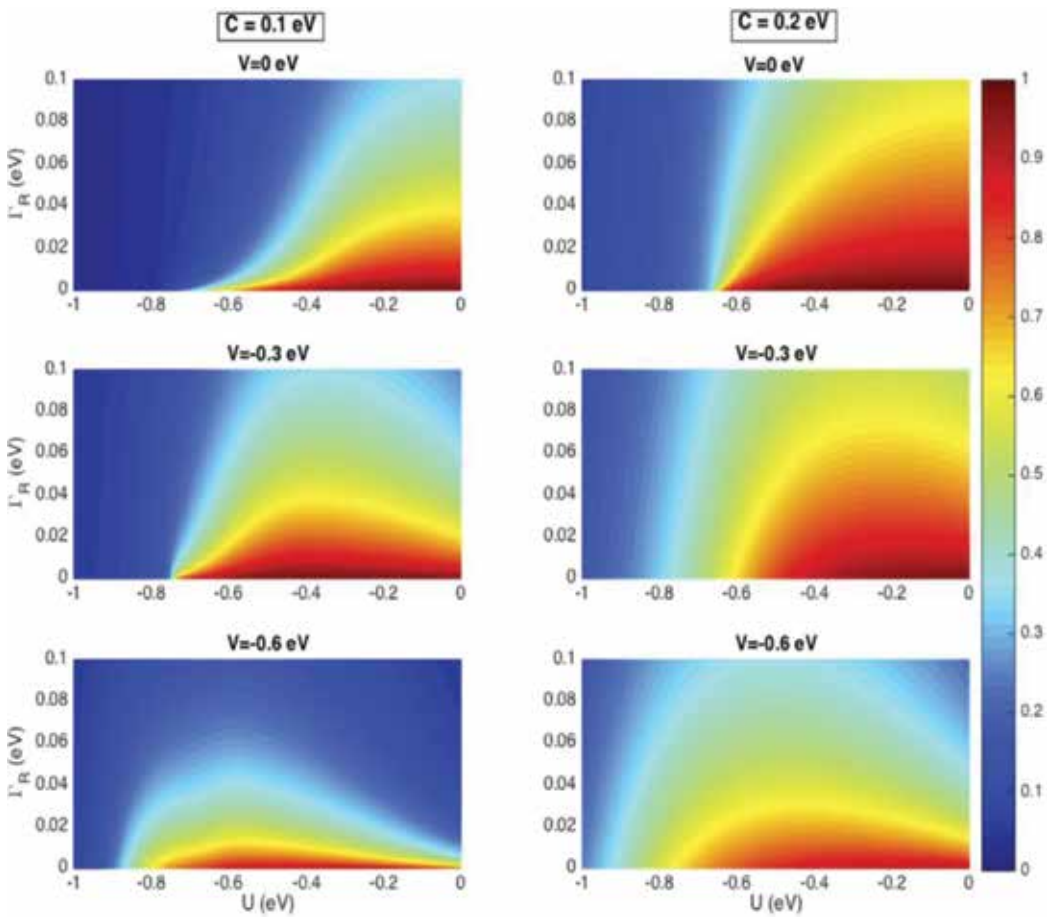

Figure 6. Charge separation yield as a function of the interaction energy (U) and recombination rate (Γ_R). The various plots are obtained upon the variation of the electron-hole interaction and for different strengths of the coupling parameters.

states increases and consequently the possibility of recombination and annihilating the charge carriers enhances. For a given electron-hole interaction strength, the yield improves with increasing values of the coupling parameter. Since the strong coupling extends the width of the DOS line shape and consequently improves the escaping rate, this behavior is understandable. Furthermore, the effect of non-radiative recombination is to diminish the yield, and its impact is more important under the influence of the strong long-range interaction condition.

3.2.2. Charge injection in polaronic bands and quantum yield of excitonic solar cells

In the performance of excitonic solar cells, coupling to the phonon modes can play a major role as it may lead to the occurrence of polarons, where a polaron is a moving charge surrounded by a cloud of virtual phonons. To address how the electron-phonon coupling (in addition to the electron-hole interaction) can affect the charge separation process, here we propose a simple tight-binding-based model. We analyze the spectrum of polaronic bands and focus on their effects on the charge separation yield, which is defined as a proportion of emitted electrons that arrive at the cathode electrode. We start the discussion by the model description.

3.2.2.1. Coupling to the phonon modes: theoretical model in the small polaron limit

We present a mathematical model to investigate the influence polaron formation has on the charge separation process of excitonic solar cells. This model can be applied to any type of excitonic solar cells. We suppose that an electron emitted at first site ($l = 0$) of a chain that represents the acceptor material and hole is fixed at the interface. We construct a simple vibration chain model which is schematically illustrated in **Figure 7**.

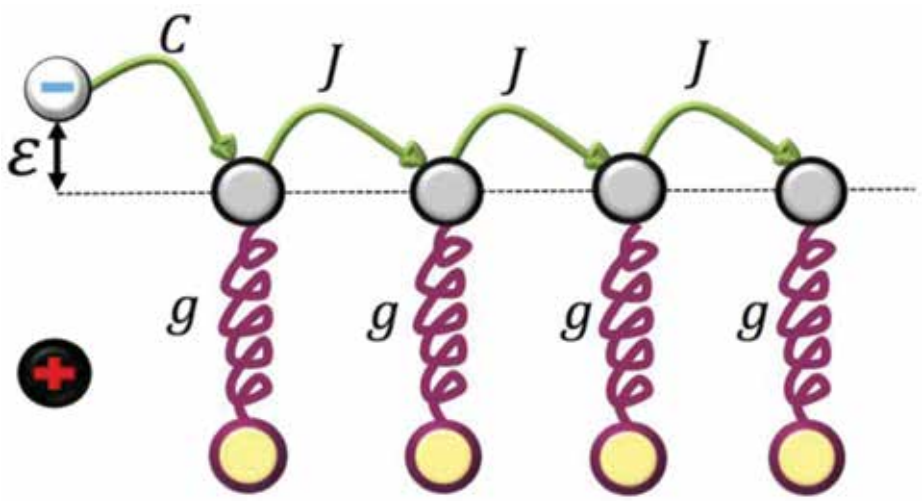

Figure 7. Schematic depiction of the chain model to describe the electron-vibration coupling which can occur on every single acceptor site when the electron arrives at that site. *C* represents the coupling parameter between interface state and initial acceptor site. The coupling between adjacent sites on the acceptor chain is shown by *J*. *g* is the strength of coupling to the phonon chains.

In this model, the charge separation process follows an interesting scenario: after the exciton dissociation at the interface, the electron either recombines with the hole which is fixed at the interface or moves through a set of acceptor sites where it can be coupled to one single phonon mode. The physical interpretation of the model is that the charge-transfer process is viewed as a hopping process when the electron interacts sufficiently strongly with intramolecular vibrations. The Hamiltonian of the considered system can be written based on the Holstein model [35]:

$$H = \varepsilon_0 c_0^+ c_0 + \sum_{l=1}^{N} \frac{V}{l} c_l^+ c_l + C\left(c_0^+ c_1 + c_1^+ c_0\right) + J\sum_{l=1}^{N-1}\left(c_l^+ c_{l+1} + c_{l+1}^+ c_l\right) + \hbar\omega_0 \sum_{l=1}^{N} a_l^+ a_l + g\sum_{l=1}^{N} c_l^+ c_l\left(a_l^+ + a_l\right) \quad (7)$$

where $a_l^+(a_l)$ and $c_l^+(c_l)$ are, respectively, the phonon and electron creation (destruction) operators on-site l, $\hbar\omega_0$ is the energy of the relevant molecular vibration, g is the electron-phonon coupling constant, C is the coupling parameter between the initial site ($l = 0$) and acceptor chain, ε_0 is the energy of the LUMO orbital of the electron at the interface, V sets the typical Coulomb potential binding the electron-hole pair, and J is the hopping amplitude within the chain. In the following section, we use the dimensionless Huang-Rhys parameter $\alpha^2 = (g/\hbar\omega_0)^2$ to characterize the strength of the electron-phonon interaction [36]. In the calculations, we consider only the nearest neighbor's tight-binding interaction and study the model at zero temperature. This assumption is justified as the electronic and vibrational energies are much larger than $k_B T$. Furthermore, we examine the model in the small polaron limit, which means that there are excited phonons only on the site where the electron arrives. The small polaron effect is present in a variety of materials, including many polymers (trans-polyacetylene, etc.) and most transition metals (MnO, NiO, etc.) [37]. Now we intend to examine the charge separation yield in the presence of electron-hole and electron-phonon interactions.

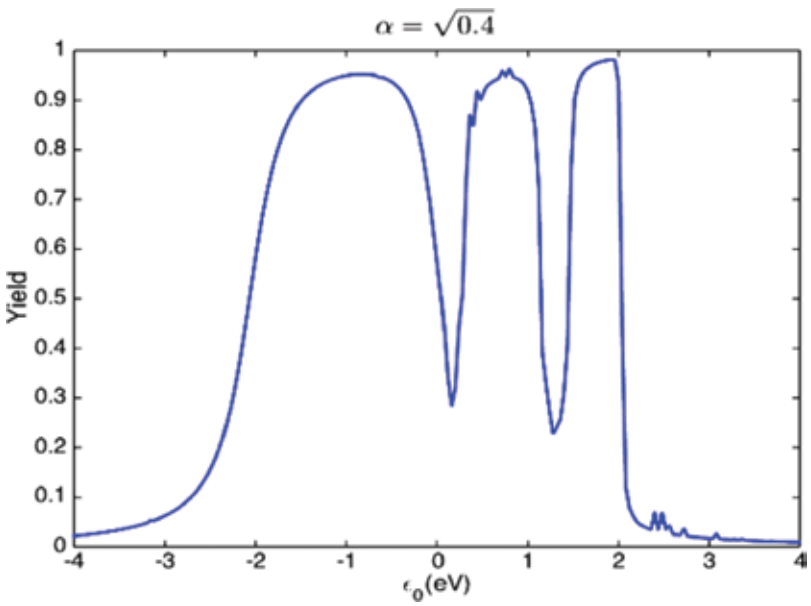

Figure 8. Yield as a function of incoming electron energy, ε_0, for various values of the electron-phonon coupling constant α in the presence of long-range electron-hole binding $V = -1\,eV$.

Let us recall that the yield is the proportion of the electrons that arrive at the cathode electrode, the other electrons recombining at the interface with the hole. We assume that the hole is localized at the two-level system (called site $l = 0$). The effects of hole propagation can be described by extending Hamiltonian Eq. (7) and normally it is expected that the hole propagation decreases the effective Coulomb potential. To study the effects of lattice distortion, we consider a coupling between electron and single intramolecular vibration mode. Besides, a Coulomb interaction between the photo-generated electron-hole pair is considered but in principle other types of interaction potentials should not significantly affect the results [38]. Since both electronic and vibrational energy scales are much larger than $k_B T$, the investigation is done at zero temperature [39]. In the following we examine the charge separation yield in the presence of electron-phonon and long-range electron-hole interaction. The charge separation yield under the influence of long-range Coulomb interaction and a given strength of electron-phonon coupling is represented in **Figure 8**.

As can be seen, first, the yield keeps the periodic resonance structure as a consequence of polaronic band formation. Second, the combined effect of Coulomb interaction and polaronic dressing

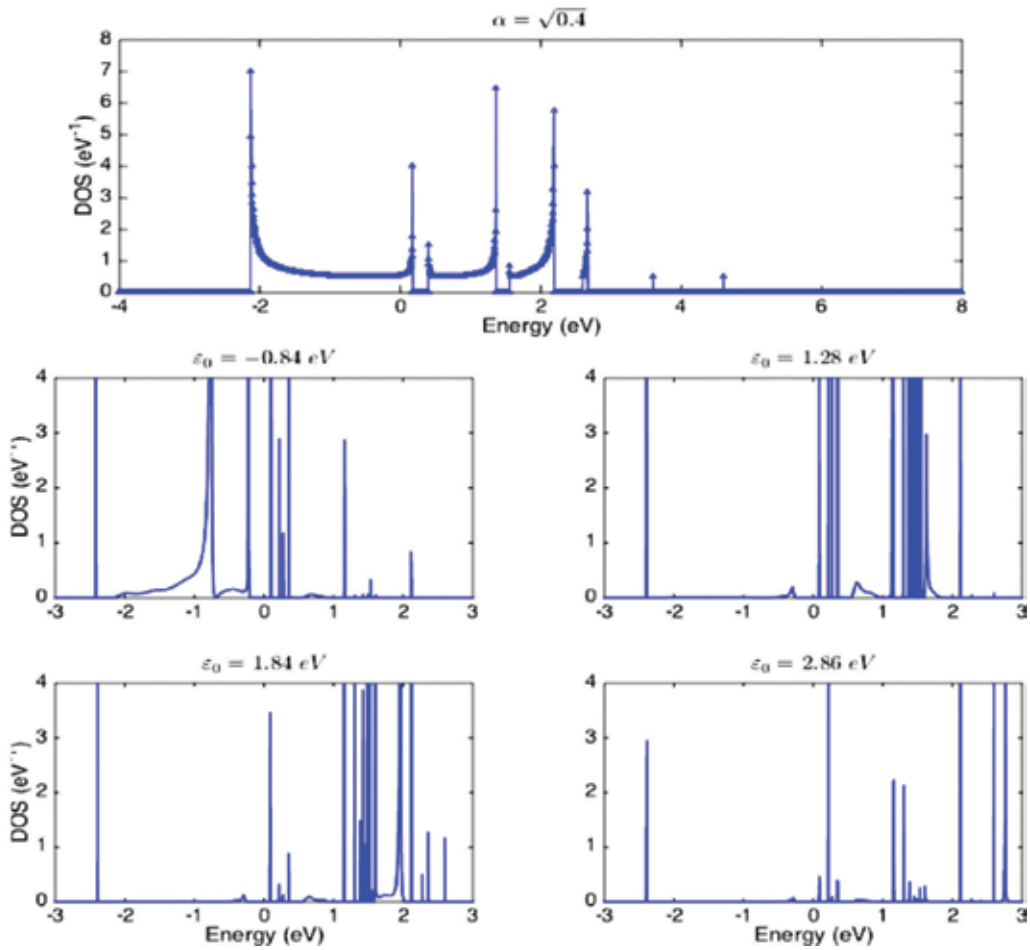

Figure 9. Local density of states in the bulk part and close to the interface for different injection energies. The electron-phonon coupling constant is $\alpha = 0.4$ and the coulomb interaction energy is $V = -1\,eV$.

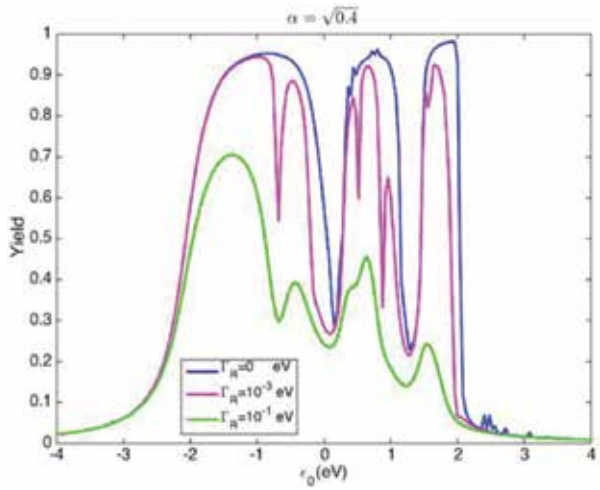

Figure 10. Yield as a function of incoming electron energy ε_0 in the presence of long-range electron-hole interaction $V = -1eV$ for the given electron-phonon coupling constant α and different electron-hole recombination rate Γ_R. The legend presented in the first panel is valid for all the other panels.

of the carriers leads to a strong overall suppression of the yield such that it never reaches one. To have clear understanding, again we refer to the spectral information. **Figure 9** represents the yield and corresponding LDOS. The LDOS is represented in the bulk part (far from the interface) and also at the interface for different injection energies. The electronic structure in the bulk part gives a view of all possible polaronic bands and the energy gap regimes. For a given injection energy ε_0, the electronic structure may contain the energy states on the allowed polaronic bands and also localized states in the energy gap (compared to the bulk DOS).

The charge carriers lying in a polaronic band can evacuate and arrive at the electrodes. On the other hand, the charge carriers localized in the bound state in the gap recombine quickly and cannot lead to photovoltaic current which diminishes the yield. Through this physical interpretation, yield values around the red marked points are in good agreement with the corresponding electronic structure. As shown, the long-range Coulomb interaction leads to an intricate spectrum with many localized and nearly localized states. This tendency to localizing the spectrum induces a lowering of the efficiency of the cell. **Figure 10** represents the effect of recombination (Γ_R) on the yield. The effects of recombination can be detected through the global reduction of yield.

4. Conclusions

The aim of this chapter was to acquire a deep understanding of the working mechanism of excitonic solar cells and to improve the device performance. Therefore, we developed a new quantum formalism based on the wave function of excitonic solar cells. The basic idea of this new methodology was shown through the example of two-level excitonic solar cells. We

demonstrated that this new methodology provides a quantitative picture of the fundamental processes underlying solar energy conversion, including photon absorption, exciton dissociation and charge separation as well as an understanding of their consequences on the cell performance. Interestingly, this theory could successfully analyze excitonic solar cell in the presence of strong Coulomb interaction between the electron and the hole. Here we highlight some of the important achievements of this study.

I. We showed that there is a competition between injection of charge carriers in the leads and recombination in the two-level system. This competition depends sensitively on the parameters of the model such as the local electron-hole interaction, the recombination rate, the coupling to the leads, and the band structure of the leads.

II. We found that the electron-hole Coulomb interaction and non-radiative recombination reduce the photocell yield, especially under the weak coupling condition where the charge carriers cannot readily escape into the contacts.

III. Finally, we provided microscopic evidence that the efficiency of charge transfer is subtly controlled by interplay of electrostatic confinement and coherent coupling of charge carrier(s) to high-energy quantized vibrational modes.

Author details

Tahereh Nemati Aram[1,2]* and Didier Mayou[1]

*Address all correspondence to: th.nemati@gmail.com

1 Néel Institute, CNRS and University of Grenoble Alpes, Grenoble, France

2 Research Institute for Applied Physics and Astronomy, University of Tabriz, Tabriz, Iran

References

[1] Lee KM, Hu CW, Chen HW, Ho KC. Incorporating carbon nanotube in a low-temperature fabrication process for dye-sensitized TiO_2 solar cells. Solar Energy Materials and Solar Cells. 2008;**92**:1628-1633. DOI: 10.1016/j.solmat.2008.07.012

[2] Yu C, Choi K, Yin L, Grunlan JC. Light-weight flexible carbon nanotube based organic composites with large thermoelectric power factors. ACS Nano. 2011;**5**:7885-7892. DOI: 10.1021/nn202868a

[3] Wu J, Wang ZM. Quantum dot solar cells. Spring. 2014. 387p. DOI: 10.1007/978-1-4614-8148-5

[4] Kalyanasundaram K. Dye-Sensitized Solar Cells. Lausanne: EPFL press; 2010. 609p

[5] Choy WCH, Ho WAA. Organic Solar Cells: Materials and Device Physics. In: London: Springer. 2012. DOI: 10.1007/978-1-4471-4823-4

[6] Jain V, Rajbongshi BK, Mallajosyula AT, Bhattacharjya G, Iyer SSK, Ramanathan G. Photovoltaic effect in single-layer organic solar cell devices fabricated with two new imidazolin-5-one molecules. Solar Energy Materials and Solar Cells. 2008;**92**:1043-1046. DOI: 10.1016/j.solmat.2008.02.039

[7] Gommans HHP, Cheyns D, Aernouts T, Girotto C, Poortmans J, Heremans P. Electro-optical study of subphthalocyanine in a bilayer organic solar cell. Advanced Functional Materials. 2007;**17**:2653-2658. DOI: 10.1002/adfm.200700398

[8] Liu M, Johnston MB, Snaith HJ. Efficient planar heterojunction perovskite solar cells by vapour deposition. Nature. 2013;**501**:395-398. DOI: 10.1038/nature12509

[9] Park SH, Roy A, Beaupré S, Cho S, Coates N, Moon JS, et al. Bulk heterojunction solar cells with internal quantum efficiency approaching 100%. Nature Photonics. 2009;**3**:297-302. DOI: 10.1038/nphoton.2009.69

[10] Ala'a FE, Sun JP, Hill IG, Welch GC. Recent advances of non-fullerene, small molecular acceptors for solution processed bulk heterojunction solar cells. Journal of Materials Chemistry A. 2014;**2**:1201-1213. DOI: 10.1039/C3TA14236A

[11] Mishra A, Fischer MK, Bäuerle P. Metal-free organic dyes for dye-sensitized solar cells: From structure: Property relationships to design rules. Angewandte Chemie International Edition. 2009;**48**:2474-2499. DOI: 10.1002/anie.200804709

[12] Spanggaard H, Krebs FC. A brief history of the development of organic and polymeric photovoltaics. Solar Energy Materials and Solar Cells. 2004;**83**:125-146. DOI: 10.1016/j.solmat.2004.02.021

[13] Bredas JL, Silbey R, Boudreaux DS, Chance RR. Chain-length dependence of electronic and electrochemical properties of conjugated systems: Polyacetylene, polyphenylene, polythiophene, and polypyrrole. Journal of the American Chemical Society. 1983;**105**:6555-6559. DOI: 10.1021/ja00360a004

[14] Fratini S, Mayou D, Ciuchi S. The transient localization scenario for charge transport in crystalline organic materials. Advanced Functional Materials. 2016;**26**:2292-2315. DOI: 10.1002/adfm.201502386

[15] Chiang CK, Fincher CR Jr, Park YW, Heeger AJ, Shirakawa H, Louis EJ, et al. Electrical conductivity in doped polyacetylene. Physical Review Letters. 1978;**40**:1472. DOI: 10.1103/PhysRevLett.39.1098

[16] Tang CW. Two-layer organic photovoltaic cell. Applied Physics Letters. 1986;**48**:183-185. DOI: 10.1063/1.96937

[17] Sariciftci NS, Smilowitz L, Heeger AJ, Wudl F. Photoinduced electron transfer from a conducting polymer to buckminsterfullerene. Science. 1992;**258**:1474-1476

[18] Yu G, Gao J, Hummelen JC, Wudl F, Heeger AJ. Polymer photovoltiac cells: Enhanced efficiencies via a network of internal donor-acceptor heterojunctions. Science. 1995;**270**:1789

[19] McEvoy AJ, Grätzel M. Sensitisation in photochemistry and photovoltaics. Solar Energy Materials and Solar Cells. 1994;**32**:221-227. DOI: 10.1016/0927-0248(94)90260-7

[20] Hodes G. Electrochemistry of Nanomaterials. Weinheim: Wiley-VCH, John Wiley & Sons; 2008. 309p

[21] Tsubomura H, Matsumura M, Nomura Y, Amamiya T. Dye sensitised zinc oxide: Aqueous electrolyte: Platinum photocell. Nature. 1976;**261**:402-403

[22] Dare-Edwards MP, Goodenough JB, Hamnett A, Seddon KR, Wright RD. Sensitisation of semiconducting electrodes with ruthenium-based dyes. Faraday Discussions of the Chemical Society. 1980;**70**:285-298. DOI: 10.1039/DC9807000285

[23] O'regan B, Grätzel M. A low-cost, high-efficiency solar cell based on dye-sensitized colloidal TiO_2 films. Nature. 1991;**353**:737. DOI: 10.1038/353737a0

[24] Nazeeruddin MK, Kay A, Rodicio I, Humphry-Baker R, Müller E, Liska P, et al. Conversion of light to electricity by cis-X2bis (2, 2′-bipyridyl-4, 4′-dicarboxylate) ruthenium (II) charge-transfer sensitizers (X= Cl-, Br-, I-, CN-, and SCN-) on nanocrystalline titanium dioxide electrodes. Journal of the American Chemical Society. 1993;**115**:6382-6390. DOI: 10.1021/ja00067a063

[25] Wöhrle D, Meissner D. Organic solar cells. Advanced Materials. 1991;**3**:129-138. DOI: 10.1002/adma.19910030303

[26] Hagfeldt A. Brief overview of dye-sensitized solar cells. Ambio. 2012;**41**:151-155. DOI: 10.1007/s13280-012-0272-7

[27] Lewis NS. Toward cost-effective solar energy use. Science. 2007;**315**:798-801. DOI: 10.1126/science.1137014

[28] Chidichimo G, Filippelli L. Organic solar cells: Problems and perspectives. International Journal of Photoenergy. 2010;**2010**. DOI: 10.1155/2010/123534

[29] Lewis NS, Crabtree G. Basic Research Needs for Solar Energy Utilization: Report of the Basic Energy Sciences Workshop on Solar Energy Utilization. US Department of Energy, Office of Basic Energy Science; 2005 April; 18-21

[30] Taylor JR. Scattering Theory: The Quantum Theory of Nonrelativistic Collisions. Mineola, New York: Courier Corporation; 2006. 478p

[31] Nemati Aram T, Anghel-Vasilescu P, Asgari A, Ernzerhof M, Mayou D. Modeling of molecular photocells: Application to two-level photovoltaic system with electron-hole interaction. The Journal of Chemical Physics. 2016;**145**:124116. DOI: 10.1063/1.4963335

[32] Nemati Aram T, Asgari A, Mayou D. Charge separation in organic solar cells: Effects of coulomb interaction, recombination and hole propagation. EPL (Europhysics Letters). 2016;**115**:18003. DOI: 10.1209/0295-5075/115/18003

[33] Nemati Aram T, Asgari A, Ernzerhof M, Quémerais P, Mayou D. Quantum modeling of two-level photovoltaic systems. EPJ Photovoltaics. 2017;**8**:85503. DOI: 10.1051/epjpv/2017004

[34] Nemati Aram T, Ernzerhof M, Asgari A, Mayou D. The impact of long-range electron-hole interaction on the charge separation yield of molecular photocells. The Journal of Chemical Physics. 2017;**146**:034103. DOI: 10.1063/1.4973984

[35] Wellein G, Fehske H. Polaron band formation in the Holstein model. Physical Review B. 1997;**56**:4513. DOI: 10.1103/PhysRevB.56.4513

[36] Feinberg D, Ciuchi S, and de Pasquale F. Squeezing phenomena in interacting electron-phonon systems. International Journal of Modern Physics B. 1990;**4**:1317-1367. DOI: 10.1142/S0217979290000656

[37] Salaneck WR, Friend RH, Brédas JL. Electronic structure of conjugated polymers: Consequences of electron–lattice coupling. Physics Reports. 1999;**319**:231-251. DOI: 10.1016/S0370-1573(99)00052-6

[38] Tamura H, Burghardt I. Potential barrier and excess energy for electron–hole separation from the charge-transfer exciton at donor–acceptor heterojunctions of organic solar cells. The Journal of Physical Chemistry C. 2013;**117**:15020-15025. DOI: 10.1021/jp406224a

[39] Fratini S, Ciuchi S. Dynamical mean-field theory of transport of small polarons. Physical Review Letters. 2003;**91**:256403. DOI: 10.1103/PhysRevLett.91.256403

Chapter 4

Effects of the Novel Micro-Structure on the Reflectance of Photovoltaic Silicon Solar Cell

Lei Zhang

Additional information is available at the end of the chapter

http://dx.doi.org/10.5772/intechopen.74972

Abstract

Reducing the cost of solar cells and improving the photoelectric conversion efficiency have attracted great attention in recent years. Forming a textured surface using suitable texturing methods was demonstrated as an effective means of increasing the ray trapping efficiency. The effects of different ray trapping structure, as formed on the surface of silicon solar cells to increase the light trapping efficiency, are different on the optical reflectance and absorptance. The aim of this chapter is to study the effects of the novel textured surface formed mechanically on the light trapping efficiency. The base angle size can be controlled mechanically to break through the limitation of crystal structure. In order to calculate the weighted reflectance of different structure, a numerical algorithm was developed in this work. The weighted reflectance was calculated numerically. The light transmission process was tracked. The ray trapping efficiency of novel texture with different parameters was calculated. The weighted reflectance in different conditions was obtained respectively.

Keywords: photovoltaic silicon solar cells, light trapping microstructure, ray tracing, weighted reflectance

1. Introduction

As solar energy is a kind of infinite and clean energy, it has been the focus of research on solar energy by reducing the reflectance to improve the photoelectric conversion efficiency. Silicon solar cell is a kind of widely used solar cell [1], and the surface texturization of silicon cells is one of major way to improve photoelectric conversion efficiency. Dominant preparation methods of light trapping structure in silicon solar cells are acid etching techniques [2], alkaline corrosion [3], mechanical grooving [4], laser grooving [5–7], reactive ion etching RIE [8–10],

mask etching [11], mask growing [12], electro-chemical corrosion [13], electrical discharge machining [14]. These methods have positive influence on improving photoelectric conversion efficiency.

At present, wet etching is the most mature method to fabricate the light trapping structure on the surface of silicon solar cells. Because of the isotropy of polycrystalline silicon, the morphology of porous silicon can be etched on the surface of polycrystalline silicon solar cells by acid etching. Compared with pyramidal textured surface, the light trapping efficiency of porous silicon is lower, and the optical reflectance is higher. As for monocrystalline silicon solar cells, pyramidal textured surface can be formed due to the anisotropy of material by alkaline etching. However, the limitation of crystal structure makes the largest base angle of the pyramid is 54.74°, some experimental studies believe that the angle is closer to 50–52°. The reflectance shown dependence on the base angle, with larger base angle size resulting in reduced reflectance. The lowest reflectance of the pyramidal textured surface formed by alkaline etching is about 10.5%.

Etching with alkaline solution such as NaOH, KOH, the texture obtained is a generally well-distributed pyramidal texture with solid top angle of 70° due to the different corrosion rate in different crystal orientation [13]. Reflectance of light when propagating from one media to another media with different refractive indices is determined by incidence, wavelength and polarization of light. Some researchers studied the effects of pyramidal structure with different top angles fabricated by mechanical way on weighted reflectance. The reflectance can reach 6% when the top angle is 60° and the reflectance is less than 10% when the incident angle of light is less than 30°. When the incident angle of light is larger than top angle, the structure tends to be a primary reflection area [15], in the light of Fresnel equations, the results could be considerably not precise. Hua et al. [16] proposed four different structures including triangular pyramid, rectangular pyramid, hexangular pyramid and cone structure. Ray-Tracing technology was employed to investigate the influence of many factors like geometrical shape, density and the top angle of the unit structure on sunlight absorption. In addition, mechanical tools develop in a trend of miniaturization and facilitation presently, Dehong et al. [17], Choong et al. [18], Rusnaldy et al. [19] have investigated and proved that single-crystalline silicon can be removed by micro machining in the ductile mode under the condition of appropriate parameters of mechanical grooving. Because of isotropy of polycrystalline silicon surface, pyramidal structure with large ratio of depth to diameter cannot be fabricated by alkaline corrosion, which appear to be a limit of this dominant fabrication method. Recently, the metal assisted chemical etching method [20–22] has been utilized to prepare SiNW(Silicon Nanowire) or nanopore structure in silicon crystalline surface called "black silicon", which has a relatively low reflectance at all angles, but the trade-off between low reflectance and low PCE (Power Conversion Efficiency) resulting from surface recombination efficiency caused by high surface-to-volume ratio of SiNW arrays is a problem [23]. Besides, preparing a homogeneous and dense light trapping structure is difficult for chemical etching way, and the acid etching and alkaline corrosion produce contaminative water and cause pollution on the surface of the finished products, the quality could be influenced. The aim of this paper is to investigate the reflectance of arc-shaped and rectangular-shaped groove structure prepared by common cutting tools, while mentioned by few papers(for our knowledge). The reflectance of light trapping structure on rectangular groove can reach 3% and even lower without ARC (Antireflection Coatings).

In this chapter, numerical analysis method is developed to simulate the reflection path of rays in the different groove light trapping microstructures, and reflectance of ray at each reflection point is determined according to Fresnel equations. Then the weighted reflectance of each structure with different incident angle of light and structural parameters was calculated and precise results were obtained. The reflection law of rectangular groove structure is strictly deduced by formula, and the best angle and optimized parameters of rectangular groove structure were proposed.

2. Textured surface models and calculated methods

2.1. Textured surface models

The normal pyramidal textured surface morphology depicted in **Figure 1**.

The size-independent behavior of the reflectance was clearly explained by a simple mathematical model in the perspective of geometric-optical. A profile was shown schematically in **Figure 2**. The orange (second reflection) and green (third reflection) areas play the role of light trapping efficiency. When the model size changes, if the ratio of the orange area to the green area does not change, the reflectance will not change. This principle also applied to the three-dimensional pyramid structure. Therefore, the height of the structure was defined as a unit length. The reflectance of the whole wafer was not affected by the change of the parameters in the subsequent stage.

The schematics of cross-sectional views for ideal model with no fillet on the included angle and the model with a fillet on the included angle were depicted in **Figure 3(a)** and **(b)**, respectively. If there exists a fillet on the included angle between neighboring pyramidal structures fabricated by mechanical way, the second model was proposed. The height of structure was set to a unit length in the algorithm. The size and angle of the structure was shown in **Figure 3**.

For convenience of calculation, a simplified two-dimensional model of arc-shaped groove structure formed under ideal mechanical condition (without uncut part, and will be mentioned below) is depicted in **Figure 4**. As **Figure 5** shows, θ_p is the primary incidence angle of light projects on arc-shaped groove trap of cell, θ_{i1}, θ_{i2}, and θ_{i3} are the incidence angle of rays at

Figure 1. Normal pyramidal textured surface morphology.

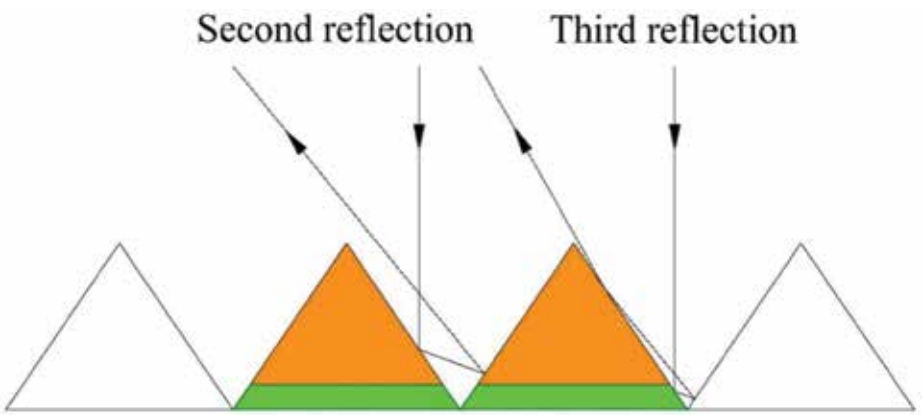

Figure 2. A simplified two-dimensional model of multiple reflections.

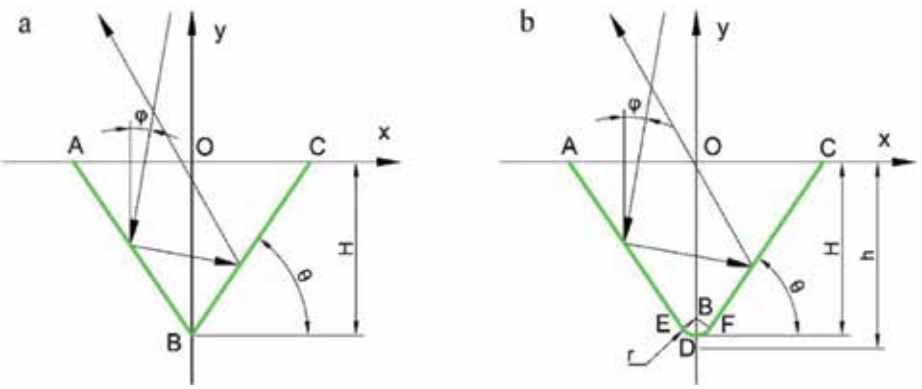

Figure 3. Schematic of (a) ideal model with no fillet on the included angle and (b) the model with a fillet on the included angle.

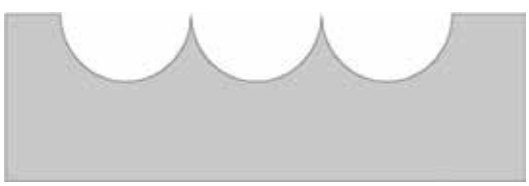

Figure 4. Simplified two-dimensional arc-shaped groove model.

each point of reflection, *r* is radius of arc-shaped light trap. The height of groove *H* is defined as the dimensionless unit length in this model.

2.2. Calculated model and numerical algorithm

To analyze light trapping efficiency of ideal arc-shaped grooved microstructure, curve equation of microstructure should be obtained first, which is determined by radius *r* and height *H*

http://dx.doi.org/10.5772/intechopen.74972

of the groove. After one reflection in microstructure, the ratio of reflected light intensity to incident light intensity is defined as primary reflectance R, and after t reflections, the ratio of reflected light intensity to incident light intensity is defined as exitance β:

$$\beta = R^t \tag{1}$$

As depicted in **Figure 6**, a beam of parallel light projects into the light trapping microstructure. This beam of parallel light can be evenly divided into n rays in the direction of horizontal width (AB). It is assumed n is large enough, and the number of reflections of the i^{th} ray is noted as t_j, then the exitance $\beta = R^{t_j}$, and the ratio of total escaped light intensity to incident light intensity is defined as weighted reflectance γ:

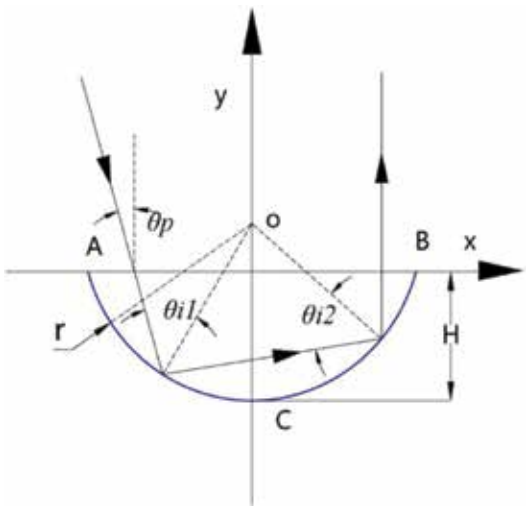

Figure 5. Schematic of arc-shaped groove structure model.

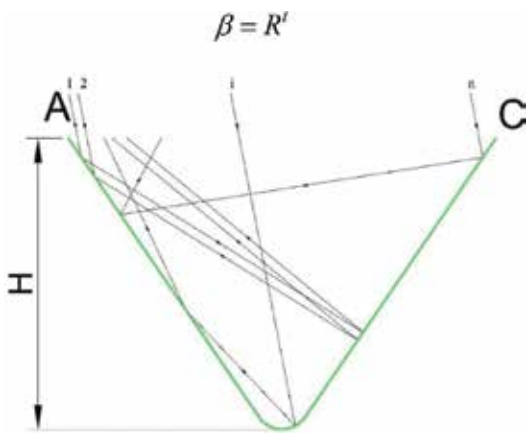

Figure 6. Multi-reflection schematic of parallel light in trap.

$$\gamma = \frac{1}{n}\sum_{j=1}^{n}\beta_j = \frac{1}{n}\sum_{j=1}^{n}R^{t_j} \tag{2}$$

the number of rays after t_j reflections is noted as n_i ($1 \le n_i \le n$, $i = t_j$), hence the Eq. (2) can be shown as following:

$$\gamma = \frac{1}{n}\sum_{j=1}^{n}R^{t_j} = \sum_{i=1}^{\infty}\zeta_i R^i \tag{3}$$

where ζ_i is the proportion of rays after i reflections relative to total rays, which can be depicted as following:

$$\sum_{i=1}^{\infty}\zeta_i = 1, \zeta_i = \frac{n_i}{n}, i = 1, 2, \cdots \tag{4}$$

The reflectance R of ordinary silicon wafer is about 0.33 [24], which can be considerably not precise for the weighted reflectance calculation. On the basis of Fresnel equations, the reflectance for s-polarized light (the component of the electric field of photons perpendicular to the plane of incidence) is explained by [25]:

$$R_s = \left|\frac{Z_2\cos\theta_i - Z_1\cos\theta_t}{Z_2\cos\theta_i + Z_1\cos\theta_t}\right|^2 = \left|\frac{\sqrt{\frac{\mu_2}{\varepsilon_2}}\cos\theta_i - \sqrt{\frac{\mu 1}{\varepsilon_1}}\cos\theta_t}{\sqrt{\frac{\mu_2}{\varepsilon_2}}\cos\theta_i + \sqrt{\frac{\mu 1}{\varepsilon_1}}\cos\theta_t}\right|^2 \tag{5}$$

the reflectance for p-polarized light (the component of the electric field of photons parallel to the plane of incidence):

$$R_p = \left|\frac{Z_2\cos\theta_t - Z_1\cos\theta_i}{Z_2\cos\theta_t + Z_1\cos\theta_i}\right|^2 = \left|\frac{\sqrt{\frac{\mu_2}{\varepsilon_2}}\cos\theta_t - \sqrt{\frac{\mu 1}{\varepsilon_1}}\cos\theta_i}{\sqrt{\frac{\mu_2}{\varepsilon_2}}\cos\theta_t + \sqrt{\frac{\mu 1}{\varepsilon_1}}\cos\theta_i}\right|^2 \tag{6}$$

where Z_1 and Z_2 are the wave impedances of media 1 and media 2, respectively, μ_1 and μ_2 are the magnetic permeability of two materials, ε_1 and ε_2 are the electric permeability of two materials. θ_i and θ_t are the incident and refracted angle of rays respectively, they are showed in **Figure 7**.

For non-magnetic materials such as silicon (i.e. materials for which $\mu_1 \approx \mu_2 \approx \mu_0$, where μ_0 is the permeability of free space), we have

$$Z_1 = \frac{Z_0}{n_1}, Z_2 = \frac{Z_0}{n_2} \tag{7}$$

The parameters n_1 and n_2 are the refractive index of media 1 and media 2 respectively. Using Snell's law and trigonometric identities, by eliminating θ_t in Fresnel equations, the reflectance for s-polarized light becomes

http://dx.doi.org/10.5772/intechopen.74972

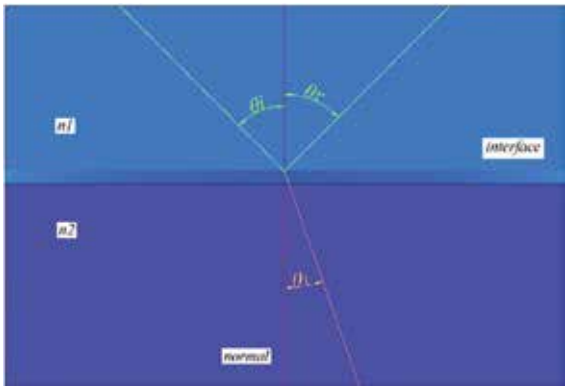

Figure 7. Variables used in the Fresnel equations.

$$R_s = \left|\frac{n_1\cos\theta_i - n_2\cos\theta_t}{n_1\cos\theta_i + n_2\cos\theta_t}\right|^2 = \left|\frac{n_1\cos\theta_i - n_2\sqrt{1-\left(\frac{n_1}{n_2}\sin\theta_i\right)^2}}{n_1\cos\theta_i + n_2\sqrt{1-\left(\frac{n_1}{n_2}\sin\theta_i\right)^2}}\right|^2 \tag{8}$$

the reflectance for p-polarized light becomes

$$R_p = \left|\frac{n_1\cos\theta_t - n_2\cos\theta_i}{n_1\cos\theta_t + n_2\cos\theta_i}\right|^2 = \left|\frac{n_1\sqrt{1-\left(\frac{n_1}{n_2}\sin\theta_i\right)^2} - n_2\cos\theta_i}{n_1\sqrt{1-\left(\frac{n_1}{n_2}\sin\theta_i\right)^2} + n_2\cos\theta_i}\right|^2 \tag{9}$$

Sun light consists of short wave trains with equal mixture of polarizations, which can be seen as unpolarized light, the reflectance for unpolarized light

$$R = \frac{1}{2}\left(R_s + R_p\right) \tag{10}$$

To derive the reflectance at each reflected point in light trap on silicon cell, we need to know refractive index of air and silicon and incidence angle at each reflected point on the interface, the refractive index of light for air is seen as 1 here, refractive index for silicon differing with wavelength of ray is shown in **Figure 9**. We used numerical software to pick out points from original refractive index curve [26], and the curve in **Figure 8** can fit original curve well by 4th order polynomial function and exponential function.

Figure 9 shows the reflectance for different wavelength rays of various incidence angles, the curve follows a trend similar to **Figure 8** when wavelength increases, the curve of incidence equal to 75° shows a lower descending gradient comparing with other smaller incidence angles, and wavelength seem to have more significant influence than incidence on reflectance of light.

By analyzing the calculated results of reflectance, the maximal value of reflectance for silicon is approximately obtained at wavelength 380 nm, R_{max} = 0.535, After 20 reflections, the exitance

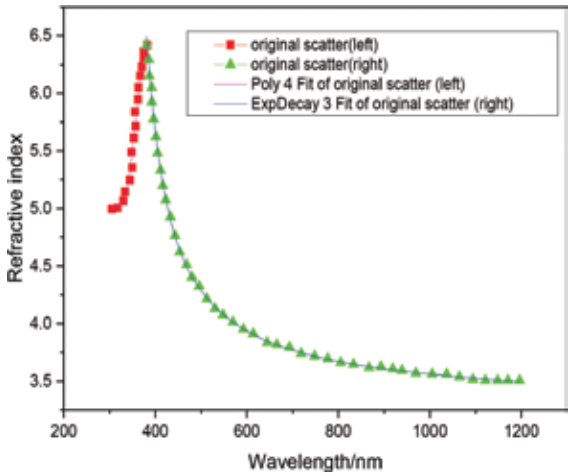

Figure 8. Refractive index for silicon to different wavelength rays.

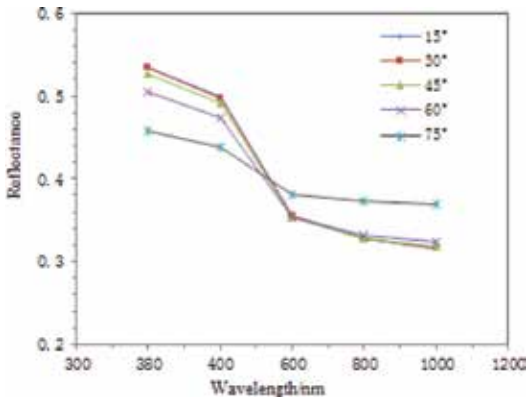

Figure 9. Reflectance for different wavelength rays.

$\beta_{20} = R_{\max}{}^{20} = 3.69 \times 10^{-6}$, and $\zeta_i < 1$ (in Eq. (4)), hence the calculations can be ignored when i>20, and the weighted reflectance γ can be shown as:

$$\gamma = \sum_{i=1}^{20} \zeta_i R^i \tag{11}$$

where R^i in formula (11) becomes

$$R^i = \prod_{j=1}^{i} R_j \tag{12}$$

where R_j is the reflectance of monochromatic ray at j^{th} reflection.

3. Results and discussions

3.1. Beam number determination

As shown in **Figure 4**, the incident light starting point was selected at point A, and then each light beam increased a distance of $\frac{2H}{n\tan\alpha}$ at x-axis direction, and ended at point C. Different weighted reflectance γ according to the flow chart were carried out when n was set to different values. γ can achieve exact value when n is larger than a certain value. The calculation results under the model with no fillet ($\theta = 55^\circ, r = 0$) on the included angle and the model with a fillet ($\theta = 55^\circ, r = H/10$) on the included angle were shown in **Table 1** and **Table 2** respectively.

A satisfactory result was obtained at $n = 200$, following works were carried out at the condition of $n = 200$. At $n = 200$, the relative errors between the adjacent dates were 0.148% and −0.491% respectively which can meet the needs of engineering completely.

3.2. Effects of base angle size on optical reflectance

As depicted in **Figure 4** (a), the calculation results were shown as curve (a) in **Figure 10** with different base angle size θ (from 30˚ to 75˚). It is notable that the structure lost light trapping efficiency when $\theta \leq 30^\circ$, according to the geometric relationship between the incident and reflected light.

The irregular curve can be discussed as follows:

The variation of reflection times changed with the base angle size was obtained after a rigorous geometric calculation: the n^{th} reflection area started occurrence when the base angle θ reached $\frac{180n-270}{2n-1}^\circ$, i.e., $\alpha = \frac{360}{2n-1}^\circ$; the whole light trapping area became n^{th} reflection area when the base angle θ reached $90\frac{n-1}{n}^\circ$, i.e., $\alpha = \frac{180}{n}^\circ$. Specifically speaking, all the incident lights reflected only one time when $\theta \leq 30^\circ$, and the reflectance was stable at 33.333%; the 2nd, 3rd, 4th, 5th, 6th reflection area starting occurrence when θ reached 30˚, 54˚, 64.286˚, 70˚, 73.636˚ respectively, and the whole light trapping area became 2nd, 3rd, 4th, 5th, 6th reflection area when θ reached 45˚, 60˚, 67.5˚, 72˚, and 75˚, respectively. And the weighted reflection γ maintained constants

n	**10**	**20**	**100**	**200**	**500**	**2000**	**5000**	**10,000**
γ/%	9.630	10.370	9.926	10.000	9.985	9.985	9.984	9.986
relative error/%	−7.143	4.478	−0.741	0.148	0	0.010	−0.014	0

Table 1. Calculated result and analysis by different n ($\theta = 55^\circ, r = 0$).

n	**10**	**20**	**100**	**200**	**500**	**2000**	**5000**	**10,000**
γ/%	9.630	11.111	11.852	12.000	12.059	12.052	12.050	12.050
relative error/%	−13.333	−6.250	−1.235	−0.491	0.061	0.012	0	0

Table 2. Calculated result and analysis by different n ($\theta = 55^\circ, r = H/10$).

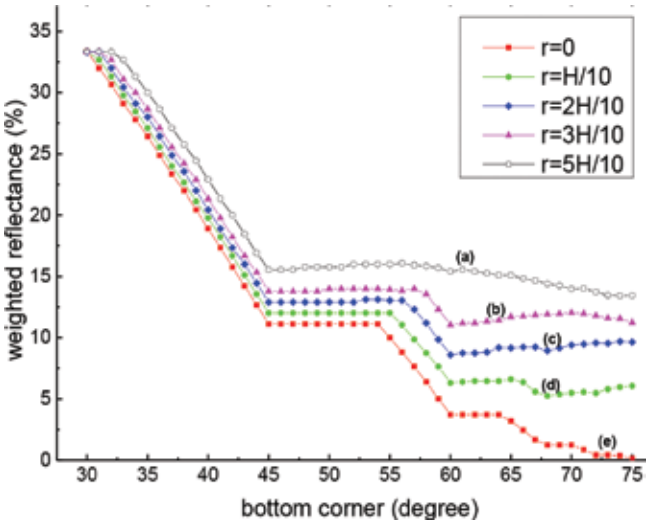

Figure 10. Relationship of weighted reflectance and the base angle size.

is 11.111, 3.703, 1.235, 0.411 and 0.137%. In other areas when there existed a variety of reflection areas, the weighted formula of reflectance was shown as in the following:

$$\gamma = aR^t + (1-a)R^{t+1} = \left(R^t - R^{t+1}\right)a + R^{t+1} \tag{13}$$

Where a is the proportion of lights projected onto the t^{th} reflection area. With increasing base angle size, a decreased linearly from 0 to 1, t and $t+1$ were the reflection times of the two kinds of reflection area which existed in the light trapping area, and R is the reflectance. Obviously it was a linear function, therefore, in each area which existed a variety of reflection areas, γ decreased linearly with the base angle size.

In a word, 60˚ was chosen as the final structure base angle of the pyramidal structure considering that the reflectance had reached a relatively stable value. In addition, 60˚ was a suitable value for the tool design.

3.3. Effects of r/H and incidence on the reflectance of arc-shaped grooved light trapping microstructure

Figure 11a, **b**, **c**, and **d** show the variation curve of weighted reflectance for wavelength 400 nm,600 nm,800 nm,1000 nm respectively when primary incidence and value of r/H change. Four graphs show similar variation tendency to each other, the weighted reflectance tends to be the least for all incidence angles when $r = H$. As the value of r/H increases, for incidence $\theta_p \leq 30^\circ$, the weighted reflectance increases monotonously and then tends to be stable, and for $\theta_p > 30^\circ$, the result decreases first and then increases, and then tends to be stable. When r/H reaches a specific value, rays tend to reflect once in the trap, the weighted reflectance become stable at the value of one reflection reflectance under the condition of their

http://dx.doi.org/10.5772/intechopen.74972

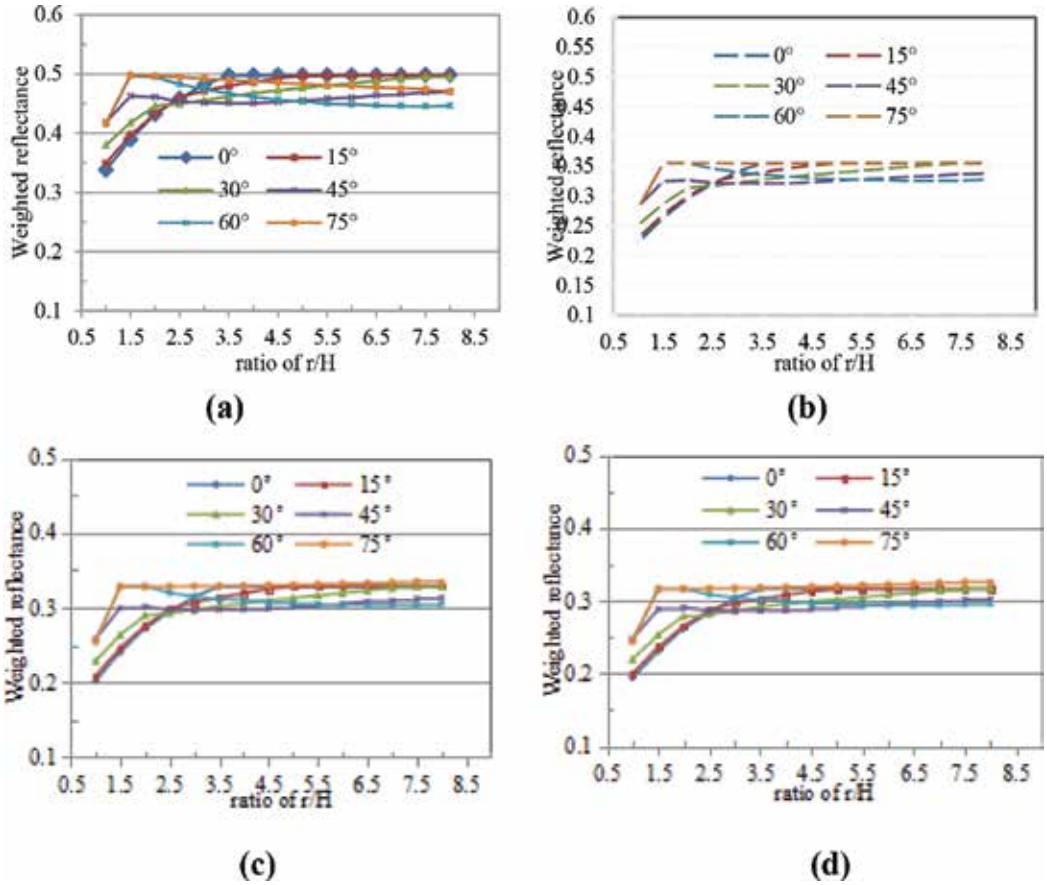

Figure 11. Effects of different ratio of r/H and primary incidence on the reflectance of arc-shaped grooves of rays of different wavelengths. Wavelengths of (a) 400 nm, (b) 600 nm, (c) 800 nm, and (d) 1000 nm.

incidence respectively. Every arc-length blocked by rays reflection in the arc equals each other, therefore, the number of reflections of ray in arc-shaped groove is positively correlated with the ratio of total arc-length to single arc-length blocked by each reflection. The rays of short wavelength show higher weighted reflectance when incidence and structure parameters are the same, which is similar to the variation trend of refractive index, it means when the other conditions remain the same, silicon shows lower absorption efficiency for shorter wavelength rays. In practical preparation process of arc-shaped micro-structure, reflectance will be higher as the existence of one reflection area of uncut part.

4. Conclusions

An algorithm was designed to calculate the weighted reflectance of the light trapping structure. The light trapping mechanism was studied by numerical algorithm with the morphology

of the light trapping structure. The weighted reflectance of pyramidal textured surface was calculated in different conditions, respectively. The optimized parameters of the pyramid texture were proposed and the best incident angle was obtained by analyzing the values. A basis method is provided for future fabrication of pyramidal textured surface by mechanical way. The following conclusions were carried out.

1. The reflectance is more suitable for commercial production when the structure is smaller and denser.
2. When the base angle size increased in the ideal pyramid model, the weighted reflectance decreased monotonically. A satisfactory light trapping efficiency was calculated at $\theta = 60^{\circ}$ in the actual pyramid model with fillet.
3. After the whole structure determined completely, the light trapping efficiency of the structure can reach a best level to accept the vertical incident light; a satisfactory light trapping efficiency also can be obtained.

Acknowledgements

This work was supported by National Natural Science Foundation of China (Grant No.51475276).

Author details

Lei Zhang

Address all correspondence to: sirzhanglei@sdu.edu.cn

Key Laboratory of High Efficiency and Clean Mechanical Manufacture of Ministry of Education, School of Mechanical Engineering, Shandong University, Jinan, China

References

[1] Yerokhov VY, Hezel R, Lipinski M, Ciach R, Nagel H, Mylyanych A, Panek P. Cost-effective methods of texturing for silicon solar cells. Solar Energy Materials and Solar Cells. 2002;**72**(1-4):291-298

[2] Sun XF, Wang HY, Lu JX, Li WQ. Preparation of large area textured polycrystalline silicon. Semiconductor Optoelectronics. 2004;**25**(3):197-200

[3] Nishimoto Y, Namba K. Investigations of texturization for crystalline silicon solar cells with sodium carbon solutions. Solar Energy Materials and Solar Cells. 2000;**61**(4):393-402

[4] Yang SY, Zhang L, Ge PG. Experimental study of the pyramidal texturization on the surface of photovoltaic silicon with cemented carbide micro-milling tool. International journal of advanced manufacture. Technology. 2017;**8**:1-10

[5] Yu JJ, Zhang JY, Boyd IW. Laser-assisted mechanical texturing of magnetic media. Applied Physics A: Materials Science and Processing. 2001;**72**(6):687-690

[6] Li P, Wang Y, Feng GJ, Zheng CD, Zhao L, Zhu JT. Study of silicon micro-structuring using ultra-short laser pulses. Chinese Journal of Lasers. 2006;**33**(12):1688-1691

[7] Wu DJ, Ma GY, Cao XS, Wang XY, Zhao FL, Guo DM. Analysis of silicon surface profile of pulsed laser bending processing. Chinese Journal of Lasers. 2007;**34**(11):1589-1593

[8] Winderbaum S, Reinhold O, Yun F. Reactive ion etching (RIE) as a method for texturing polycrystalline silicon solar cells. Solar Energy Materials and Solar Cells. 1997;**46**(97):239-248

[9] Ruby DS, Zaidi SH, Narayanan S, Damiani BM, Rohatgi A. Rie-texturing of multicrystalline silicon solar cells. Solar Energy Materials and Solar Cells. 2002;**74**(s1–4):133-137

[10] Chen WH, Lin HH, Hong FCN. Improvement of conversion efficiency of multi-crystalline silicon solar cells using reactive ion etching with surface pre-etching. Thin Solid Films. 2005;**597**:50-56

[11] Zhao JH, Wang AH, Campbell P, Green MA. A 19.8% efficient honeycomb multicrystalline silicon solar cell with improved light trapping. IEEE Transactions on Electron Devices. 1999; **46**(10):1978-1983

[12] Webber KJ, Blakers AW, Catchpole KR. The epilift technique for Si solar cells. Applied Physics A: Materials Science & Processing. 1999;**69**(2):195-199

[13] Chen YS, Wang HY, Yang SE. Application of light trapping in the crystal silicon cell. Lasers & Optoelectronic Progress. 2004;**41**(5):56-58

[14] Qiu MB, Huang YH, Liu ZD, Tian ZJ, Wang W. Numerical study on effect of silicon texture structure on reflectance of light. Acta Optica Sinica. 2008;**28**(12):2394-2399

[15] Yang SY, Ge PQ, Zhang L. The effects of different pyramidal textured silicon surface parameters on the optical reflectance. Solar Energy. 2016;**134**:392-398

[16] Hua X, Zhang Y, Wang H. The effect of texture unit shape on silicon surface on the absorption properties. Solar Energy Materials and Solar Cells. 2010;**94**(2):258-262

[17] Huo DH, Lin C, Choong ZJ, Pancholi K, Degenaar P. Surface and subsurface characterisation in micro-milling of monocrystalline silicon. The International Journal of Advanced Manufacturing Technology. 2015;**81**(5):1319-1331

[18] Choong ZJ, Huo DH, Degenaar P, O'Neill A. Effect of crystallographic orientation and employment of different cutting tools on micro-end-milling of monocrystalline silicon. Proceedings of the Institution of Mechanical Engineers Part B-Journal of Engineering Manufacture. 2016;**230**(9):1756-1764

[19] Rusnaldy, Ko TJ, Kim HS. Micro-end-milling of single-crystal silicon. International Journal of Machine Tools and Manufacture. 2007;**47**(14):2111-2119

[20] Mews M, Leendertz C, Algasinger M, Koynov S, Korte L. Amorphous/crystalline silicon heterojunction solar cells with black silicon texture. Physica Status Solidi RRL: Rapid Research Letters. 2014;**8**(10):831-835

[21] Lee I, Paik U, Park J. Solar cell implemented with silicon nanowires on pyramid-texture silicon surface. Solar Energy. 2013;**91**:256-262

[22] Jung JY, Um HD, Jee SW, Park KT, Bang JH, Lee JH. Optimal design for antireflective Si nanowire solar cells. Solar Energy Materials and Solar Cells. 2013;**112**:84-90

[23] Toor F, Branz HM, Page MR, Jones KM, Yuan HC. Multi-scale surface texture to improve blue response of nanoporous black silicon solar cells. Applied Physics Letters. 2011;**99**: 103501

[24] Lu JX, Sun XF, Wang HY, Li WQ, Gu JH. The texturisation of multicrystalline silicon by chemical etching. Acta Energiae Solaris Sinica. 2004;**25**(2):138-141

[25] Hecht E. Optics. 4th ed. Addison Wesley; 2002 ISBN 0-321-18878-0

[26] Qian CF, Wang QK, Li HH. Design of Black Silicon with ultra-light-trapping structure. Acta Optica Sinica. 2011;**31**(10):61-65

Chapter 5

From 11% Thin Film to 23% Heterojunction Technology (HJT) PV Cell: Research, Development and Implementation Related 1600 × 1000 mm² PV Modules in Industrial Production

Eugenii Terukov, Andrey Kosarev,
Alexey Abramov and Eugenia Malchukova

Additional information is available at the end of the chapter

http://dx.doi.org/10.5772/intechopen.75013

Abstract

Plasma-enhanced chemical vapor deposition (PECVD) developed for thin film (TF) Si:H-based materials resulted in large area thin film PV cells on glass and flexible substrates. However, these TF cells demonstrate low power conversion efficiency PCE = 11% for double and PCE = 13% for triple junction cells below predicted PCE ≈ 24%. PV cells on crystalline silicon (c-Si) provide PCE ≈ 17–19%. Cost of c-Si PV cells lowered continuously due to reducing price of silicon wafers and enlarging their size. Two factors stimulated a combination of PECVD films and c-Si devices: (a) compatibility of the technologies and (b) possibility for variation of electronic properties in PECVD materials. The latter results in additional build-in electric fields improving charge collection and harvesting solar spectrum. We describe a transformation of PECVD TF solar cell technology for 11% efficiency modules to heterojunction technology (HJT) c-Si modules with 23% efficiency. HJT PV structure comprises c-Si wafer with additional junctions created by PECVD deposited layers allowing development of single wafer PV cells with PCE ≈ 24% and the size limited by wafer (15.6 x 15.6 cm²). The chapter starts with background in PECVD and c-Si PV cells. Then, in Section 2, we describe electronic properties of PECVD materials in HJT PV structures. Section 3 deals with structure and fabrication process for HJT devices. In Section 4, we present and discuss performance characteristics of the devices. Section 5 describes implementation of the developed HJT module (1600 x 1000 mm²) based on HJT single wafer cells in industry with presentation and discussion of characteristics related to industrial production. Finally, Section 6 presents the outlook and summary of the chapter.

Keywords: photovoltaic solar cells, HJT silicon solar cells, solar cell modules, plasma deposition

1. Introduction

Market of PV devices shows continuous increase, for example, for only 1 year, that is, 2016–2017, it has grown from 76 GW to about 100 GW (by more than 30%) [1]. PV devices based on silicon dominate in the market (>90%). Interdigitated back contact (IBC) cells on monocrystalline n-type silicon demonstrate mass production efficiency, PCE = 23% (2016) with prognosis to rise to PCE = 27% by 2027 [1]. Fabrication of these devices is complicated because of multiple deposition and etching steps required to form both p- and n-doped contact areas on rear surface of the cells. Moreover this fabrication is based on conventional crystalline silicon technology including high temperature processes. Alternative and relatively simple approach to get high efficiency defined as heterojunction technology (HJT) includes deposition of thin layers by plasma-enhanced chemical vapor deposition (PECVD) conducted at low temperature. PECVD technique provides a wide range of possibilities for material engineering with variation of structure, electronic properties and doping of the films. These films can be used for surface passivation and for creation of additional built in electric field at interfaces with silicon. HJT solar cells exhibit PCE = 22% (2016) with prognosis for rise to PCE = 24% in 2027 [1]. Furthermore, a combination of HJT and back contact technology will allow to overcome PCE values predicted for conventional IBC cells made with diffusion approach as it is confirmed by a world record PCE values above 26% reported for such cells [2].

PECVD is a rather mature industrial technology exploited to fabricate both PV modules on both glass substrate with dimensions up to 2200 × 2600 mm^2 and flexible plastic or metal foil substrates. The best developed PECVD PV structures provide efficiency, that is, PCE = 11% for "micromorph" two junction tandem [3] and PCE = 13% for triple tandem on stainless steel foil [4]. These values are less than those theoretically predicted PCE = 24%. Therefore, PECVD PV solar cell modules on glass are not able to compete with those based on crystalline silicon technology for terrestrial applications, though they occupy a segment of flexible solar cells in PV market. Advantages of PECVD technology for material engineering together with compatibility of this technique with c-Si technology made promising implementation of PECVD materials in c-Si PV technology resulting in development of HJT solar cells. The latter is attractive because of PECVD is a low-temperature process and also because of its performance demonstrated.

This chapter describes our experience in research and development of HJT solar cells and modules based on our previous background in fabrication of "micromorph" modules; implementation of HJT modules consisted of 60 cells in industrial production is also discussed.

2. Configurations and fabrication of HJT devices

In this section, we describe basic configurations of solar cells based on crystalline materials. **Figure 1** shows cross-section diagrams for crystalline silicon solar cell (a) fabricated by standard

diffusion processes with typical efficiency of 17–19%, PECVD thin silicon film "tandem" structure (c) comprising two p-i-n junctions with efficiency of 9–11% and HJT silicon-based solar cell incorporating some PECVD films.

n-Type c-Si is a conventional material for HJT cells nowadays, although HJT solar cells based on p-type silicon with efficiency above 20% have been also reported, for example, see Ref. [5].

Despite using floating zone (FZ), c-Si for record cells and reasonable parameters obtained on high-quality multicrystalline wafers manufactured with direct solidification technique [6], crystalline silicon made by Czochralski (CZ) technique is conventionally used for HJT cells' mass production. In this study, 6" CZ Si pseudo square n-doped <100> wafers with typical resistivity in the range from 1 to 5 Ohm·cm were used. The wafers were sliced with diamond wire technology from ingots with low impurity level providing bulk lifetime of minority carriers $\tau > 1$ ms measured by transient photoconductance technique on ingots.

It is worthy of some comments in terms of different HJT configurations. Frontal side of solar cell is determined as that for penetration of incident light, and opposite side is determined as rare (or back) side. There is also not well-justified term "emitter" which nevertheless is widely used in the literature, it is referred to the position of p(or p^+) layer. Two configurations of HJT cells are possible: with frontal emitter meaning p-layer position on frontal side and rare (back) emitter meaning p-layer on rear side. For industrial production, to our mind rear emitter is preferable because of higher contribution of the wafer in lateral conductivity resulting in lower requirements for contact grid (lines may be narrower and separated by longer distance) and consequently, reducing shadow losses. In addition, employing n-layer made of nanocrystalline silicon (PECVD nc-Si) on frontal side results in reducing absorption losses from frontal side. However, lower holes diffusion length and nonuniform absorption of the incident light inside of c-Si wafer resulting in much higher carrier generation rate at

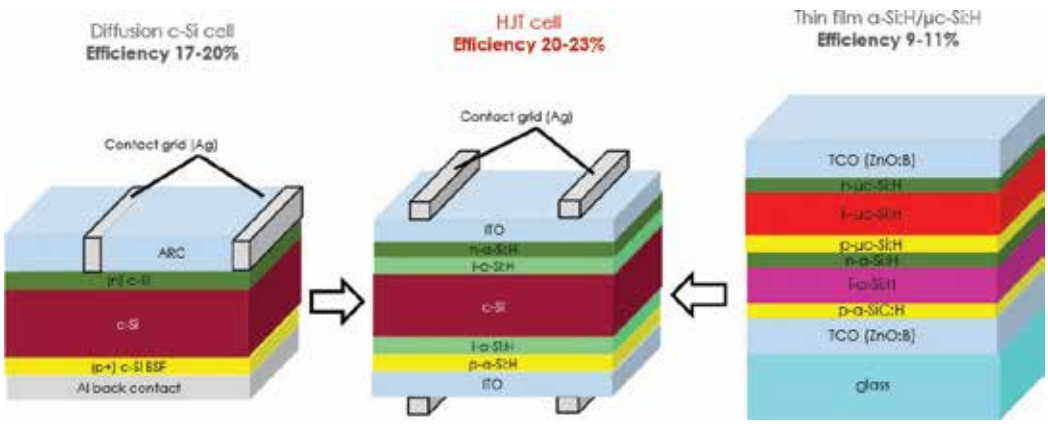

Figure 1. Configurations of different solar cells: (a) crystalline silicon c-Si device fabricated with diffusion processes, (b) HJT cell comprising c-Si and PECVD materials and (c) thin film a-Si:H/mk-Si:H solar cell (two junction tandem).

front interface lead to record efficiencies on laboratory cells with frontal emitter configuration [7]. As seen in **Figure 1(b)** and **(c)**, the structures comprise different PECVD films such as undoped (e.g., amorphous silicon a-Si:H, microcrystalline mk-Si:H), p-doped (e.g. p-a-SiC:H, p-mk-Si:H) and n-doped (e.g. n-a-Si:H, n-mk-Si:H). Electronic properties of these films are discussed in Section 3 and film deposition in Section 5.

Here, we would like to provide some comments on functions of these films in device structures. Historically, first c-Si solar cells contained p- and/or n-doped layers prepared with diffusion, and they contacted to metals. They are characterized by significant losses at interfaces due to several processes, for example, free carrier absorption, surface recombination, and so on, and efficiency achieved is 17–19%. Further progress is related to the development of significantly more complex structures such as passivated emitter rear locally diffused (PERL) [8] and passivated emitter and rear cell (PERC) solar cells [9]. Then PV structures prepared by heterojunction technology called HJT solar cells_ have been developed [9]. In these HJT structures crystalline silicon surfaces is passivated by PECVD films which also create heterojunctions providing additional built-in electric fields, reduce surface recombination and back diffusion of photocarriers and serve as anti-epitaxial buffer.

3. Electronic properties of PECVD materials used in HJT solar cells

Let us consider some principal electronic properties of PECVD films used in HJT solar cells. They are listed in **Table 1** that contains some electrical and optical characteristics of the films. It is seen that properties of PECVD films differ significantly from those in crystalline materials comprising the same atoms. For example, optical gap for c-Si Eg = 1.1 eV and for amorphous silicon a-Si:H Eg = 1.62–1.65 eV, there is also a difference in activation energy of conductivity. These films can be also doped in n- and p-type though with less efficiency of doping compared to crystalline one. Difference of these characteristics provides possibility creation of heterojunctions with crystalline silicon resulting in local built-in electric fields. Conventionally, PECVD films are deposited from hydride gases such as silane (SiH_4), methane (CH_4), and

Layer type	E_g (eV)	n@500 nm	k@500 nm	E_a (eV)
i-layer(a-Si:H)*	1.65	4.79	0.61	0.75–0.82
p-layer(a-Si:H)	1.62	4.2	0.47	0.3–0.4
n-layer(a-Si:H)	1.63	4.72	0.6	0.25–0.35
p-layer (nc-Si:H)	1.87*	4.22	0.18	0.08–0.12
n-layer (nc-Si:H)	1.83*	4.16	0.20	0.02–0.04
p-layer (a-SiC:H)	2.02	3.49	0,24	0.45–0.50

*E_{04} values are presented.

Table 1. Electronic properties of PECVD films incorporated in HJT solar cells.

germane (GeH_4), which are often supplied as a mixture with hydrogen. Thus, glow discharge during film growth contains significant amount of hydrogen in the form of molecules, atoms and ions. The latter two are very active chemically promoting passivation of substrate surface, which is of principle importance during fabrication of HJT solar cells.

There are various techniques to grow thin device quality films, for example, atomic layer deposition (ALD), hot wire (HW) deposition, inductively coupled plasma (ICP), direct current (DC), low frequency (LF), radio frequency (RF), very high frequency (VHF), microwave plasma in capacitance type reactors, and so on. Comparison of these techniques is out of the scope of the chapter; therefore, we only notice that the industry is mostly employed with RF and VHF PECVD systems. The latter type is used for fabrication of HJT solar cells in this chapter.

Nanometer-scale thicknesses of the PECVD films in HJT structures are really a challenge in material engineering and electronic characterization of such films. Conventionally, at initial stage, material of each film and its electronic properties are optimized by preparing the samples on appropriate substrate such as glass or silicon. Thickness of the film at this stage is more than 100 nm, while in HJT structures, we need 5–20 nm thickness. Therefore, questions arise: is it possible to characterize such thin films? Is it possible to apply electronic characteristics measured in thicker films in device design? Up to now, there are contradictory data reported. Some researchers have observed changes in electronic properties with thickness [10], while others have revealed such behavior. Here, we present some data obtained in thin films by attenuated total reflection infrared spectroscopy (ATR IR) spectroscopy technique allowing characterization of rather thin films. To our mind, both spectral ellipsometry and ATR IR are widely used technique for thin film characterization. ATR IR spectroscopy allows measurements of the films with thickness less than 20 nm, that is, in the range of thickness of the films in HJT device structures. **Figure 2** shows IR spectra (measured by transmission on silicon substrate and ATR IR technique) of the films deposited on different substrate (glass and silicon) in the same run. The peaks for both curves are located at the value of k = 2000 cm^{-1}suggesting practically the same hydrogen bonding structure in the samples.

Figure 3 presents ATR IR spectra around k = 2000 cm^{-1} (Si-H stretching mode) for the intrinsic and doped samples with different thicknesses. One can see in the figure that using ATR IR absorption spectra of a-Si:H film, it is possible to observe Si-H stretching mode in the films with thickness less than 20 nm; therefore, this technique can be effectively used for optimization of the films with thickness required for HJT cells. It is clearly seen that all the curves are well centered at k = 2000 cm^{1}. No detectable changes have been observed with thickness.

This is revealed even more clearly in **Figure 4**, where the spectra are normalized at maximum value for both intrinsic and p-doped layer. Thus, we have demonstrated some evidence for negligible effect of thickness on microstructure and consequently on electronic properties.

In other words, some basic material optimization can be performed by optical measurements with ellipsometry or ATR IR spectroscopy in the films deposited on some acceptable substrates (e.g., on glass), which is of principal importance for optimization of uniformity and electronic properties in ultrathin films deposited in mass production PECVD systems.

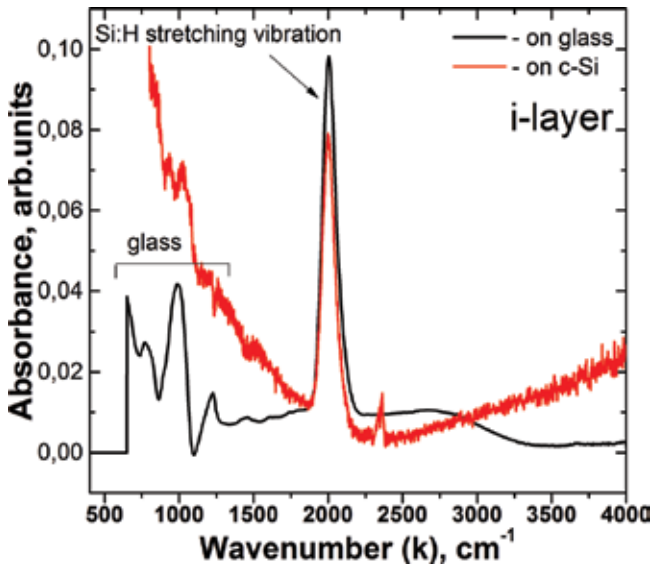

Figure 2. IR absorption spectra measured by transmission and ATR IR spectroscopy.

After the basic optimization, the characteristics obtained can be extrapolated to the thicknesses of the films in device structures. However, such optimization is only initial stage because always growth conditions for the films even in the same run (with fixed operator deposition parameters) are different for the film deposited on glass from those when the film is deposited on stack of previously deposited films. Therefore, it should be noted that final optimization of the films is performed in concrete device structures for concrete film inserted between other materials. Figures of merit for such optimization are performance characteristics of the device.

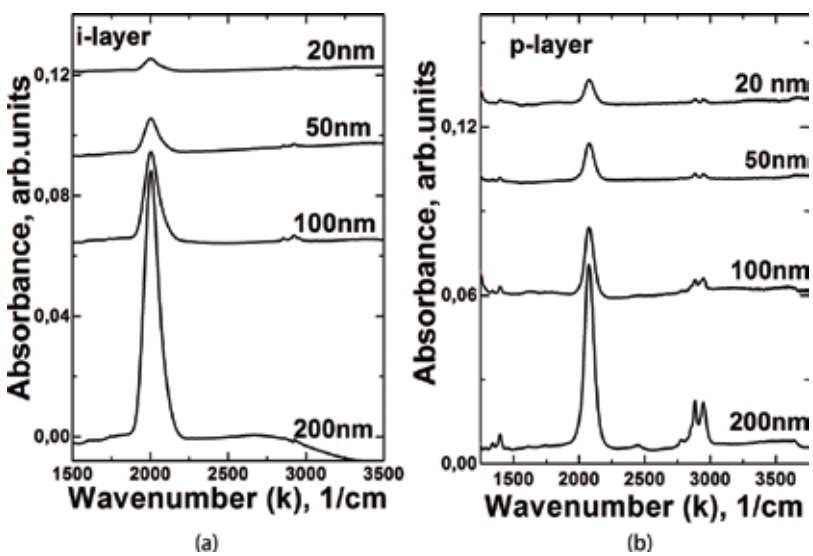

Figure 3. ATR IR spectra of intrinsic (a) and doped (b) a-Si:H layers of different thickness.

http://dx.doi.org/10.5772/intechopen.75013

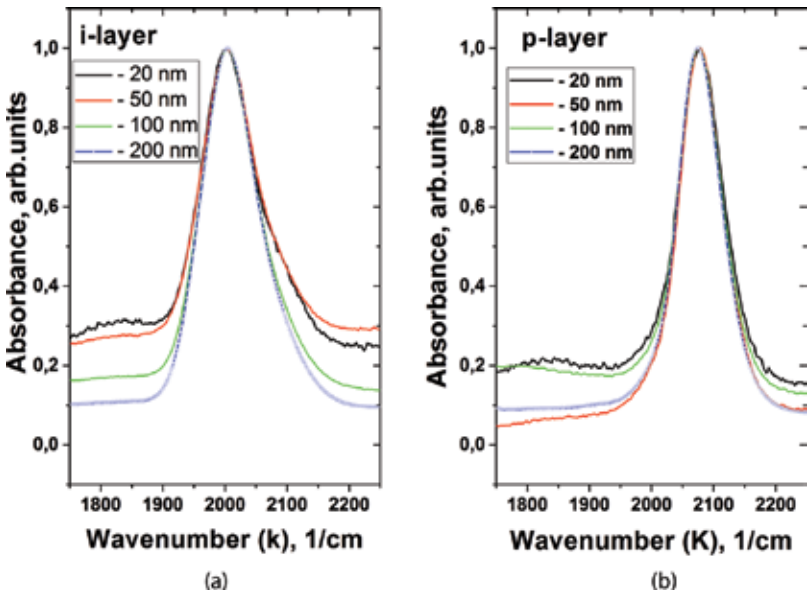

Figure 4. Normalized IR absorbance spectra for intrinsic i-a-Si:H (a) and p-doped p-Si:H layers (b).

4. Performance characteristics of HJT solar cells (single wafer devices)

Performance characteristics of both solar cells and modules allow obtaining finally power conversion efficiency (PCE) of solar energy into electric energy, to see harvesting photons of different energy of the Sun spectrum and to get insight into technological issues. In this section, we describe and discuss these characteristics for single wafer HJT solar cells.

PCE values are conventionally determined from current–voltage J(U) characteristics measured with illumination of solar simulator providing incident light intensity I_{inc} = 1000 W/m^2 and AM 1.5 conditions. An example of J(U) characteristic is shown in **Figure 7**, and the characteristics calculated from this J(U) curve are given in the insert. PCE is defined by the following equation:

$$PCE = \eta = (J_{sc}\, U_{oc})\, FF/I_{inc} \quad (1)$$

where J_{sc} is the short circuit current density determined at U = 0, U_{oc} is the open circuit voltage determined at J = 0, I_{inc} is the incident light intensity and FF is the fill factor.

Progress in efficiency for single wafer HJT solar cells and some images of the samples as a function of R&D time in RDC TF TE are presented in **Figure 5**.

Starting in 2014, with small area prototypes RDC TF TE in 2017 achieved PCE = 22.8% for solar cell with 156 × 156 mm^2 dimensions (corresponding area S = 244 cm^2) in 2017. This cell is the base for large area modules with dimensions 1600 × 1000 mm^2. Fabrication and characteristics of this module are presented and discussed in Section 5.

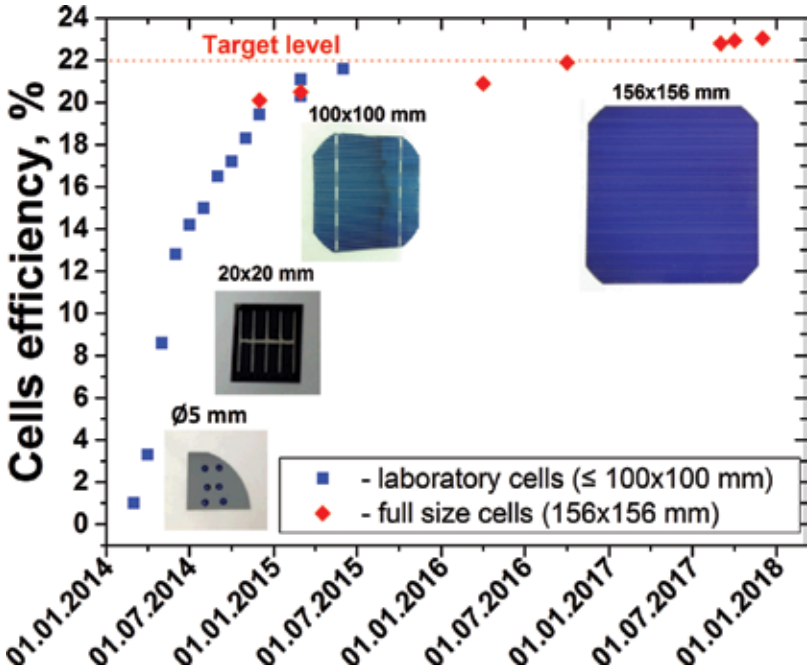

Figure 5. PCE increase of HJT single wafer solar cell during the development in RDC TF TE.

In order to improve light trapping in the device structures, Si wafers were textured using isopropanol alcohol (IPA) free alkaline process. Despite diamond wire, sliced wafer can be successfully textured from as cut state without surface damage etch (SDE) step, we used SDE because it facilitated uniform texturing, improved process stability and reduced production costs by lower consumption of surfactants providing anisotropic Si etching along <111> direction.

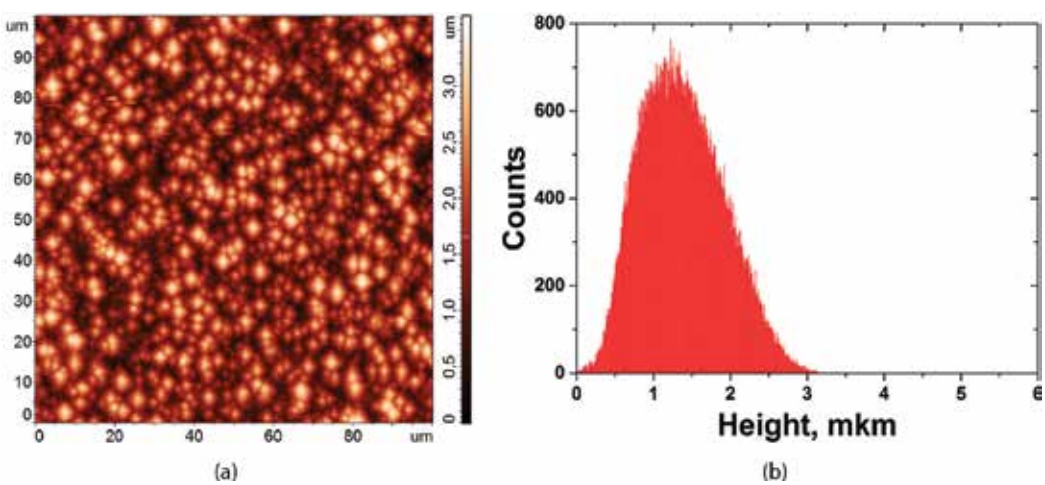

Figure 6. AFM image of textured Si wafer surface (a) and distribution function of heights (b).

As a consequence, textured wafers have pyramidal surface topology with size and distribution of pyramids controlled by parameters of etching process. An example of AFM image of textured wafer is shown in **Figure 6**. One can see in the figure that surface of textured wafer is uniformly covered by pyramids with average height about 1.5 mkm.

Special attention has been paid to final cleaning of wafers surface from organic and metal impurities. We used several cleaning steps followed by final HF-dip and hot nitrogen drying procedure.

Current-voltage characteristic of our best cell measured under standard test conditions (STC) is shown in **Figure 7** for single wafer HJT solar cell (156 × 156 mm^2). This cell exhibits such parameters as efficiency PCE = 23.04%, Uoc = 735 mV, Isc = 9.45 A and FF = 81.0%.

Spectral characteristics for different c-Si solar cells, including single wafer HJT solar cell, are presented in **Figure 8**. Comparing spectral curves in **Figure 8**, we can see that PERC solar cell has higher response in short wavelength range (λ < 500 nm) and lower response in long wavelength region (λ > 900 nm) than HJT device resulting in a small difference about 2% in integral current. Multicrystalline solar cell made by the BSF technology currently dominating in PV market has a little bit better response for λ < 350 nm and worse response for λ > 900 nm when compared to that for HJT device resulting in lower value of integral current. Both PERC and HJT silicon solar cells provide high and close values of integral short circuit currents.

Average values of characteristics are presented in **Table 2**.

Dispersion values for the measured characteristics indicate rather good reproducibility of electronic properties observed in the device structures. For comparison, record data on HJT single wafer solar cell reported by "Kaneka Corp," Japan in 2017 [2]. This company increased its previous record in 2015 from PCE =25.1% to PCE = 26.6% in 2017 and the predicted efficiency exceeded 27% soon. It is worth to note that cells with record characteristics require

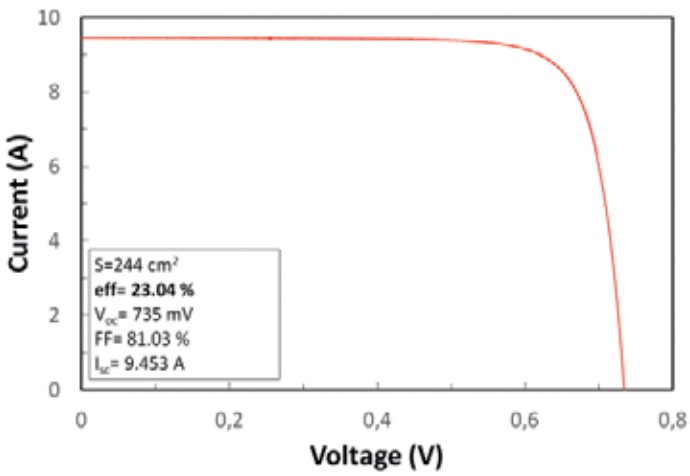

Figure 7. Current-voltage I(U) graph and characteristics for single wafer HJT cell (156 × 156 mm^2).

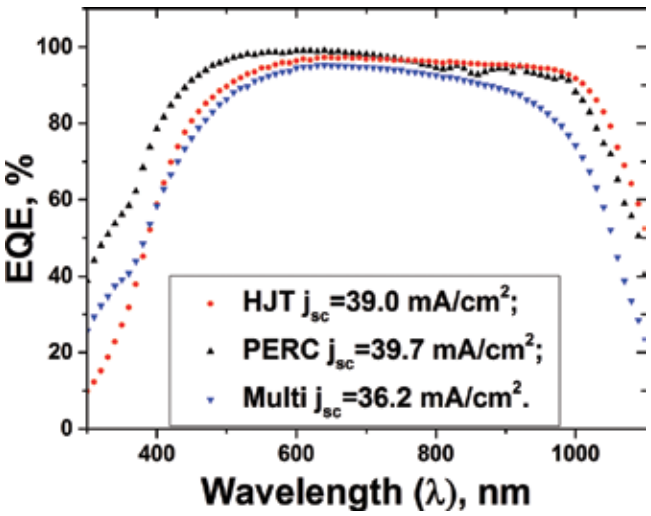

Figure 8. Spectral response of PV cells fabricated with crystalline silicon, PECVD silicon films and combination in HJT structures.

	Isc (A)	Voc (V)	Pmax (W)	Vpmax (V)	Ipmax (A)	FF (%)	Eff (%)
Avg. value	9.45 ± 0.01	0.73 ± 0.01	5.52 ± 0.01	0.63 ± 0.01	8.80 ± 0.01	79.9 ± 0.1	22.6 ± 0.1
"Kaneka" 2017 [2]	10.37*	0.740	Not reported	Not reported	Not reported	84.7	26.6

*Calculation based on data in [2]: area S = 180 cm^2, density of short circuit current Jsc = 42.5 mA/cm^2.

Table 2. Performance characteristics of HJT single wafer (156 × 156 mm^2) HJT solar cells.

usually special design and materials which may not be compatible with mass production conditions and/or facilities; however, such high efficiency level of laboratory cells demonstrates definitely potential for further improvement of HJT technology.

5. Implementation of the developed single wafer HJT structures in 1600 × 1000 mm^2 modules in industrial production

PECVD films for previous optimization were deposited in RDC TF TE laboratory system from "Oerlikon Solar," Switzerland, model Gen 5 KAI, photo is presented in **Figure 9(a)**. Reactor of this system is similar to the industrial system "KAI MT R1.0 Modular PECVD System" installed for industrial fabrication of the large modules S = 1600 × 1000 mm^2. Photo of this system is shown in **Figure 9(b)**. In both PECVD systems, capacitive glow discharge at frequency f = 40.68 MHz, is used, deposition temperature is about T_d = 200 C, technological gases of semiconductor purity.

Figure 9. Laboratory installation (a) and industrial PECVD system (b).

We shall skip description of technological process details and discuss only some specific issues related to HJT with crystalline silicon wafers large area module fabrication. Initially, these systems were employed for fabrication of thin film double junction tandem module on glass substrate (see diagram in **Figure 1(c)**). For HJT solar cell module, silicon wafers are placed on a special wafer carrier developed by RDC TF TE and then loaded into reactor. More details (process sequence, equipment, project milestones, etc.) on process of conversion silicon thin film solar module to high efficiency HJT module production can be found in ref. [11].

An important issue for large area modules is uniformity of electronic properties of the films deposited on large area substrate (or the carrier with 60 wafers).

Map of thicknesses for a-Si:H films deposited on large area glass substrate is shown in **Figure 10** with mean thickness value $<d> = 48.5$ nm and deviation of thickness $<\Delta d> = 7.1\%$. In other words, thickness of the films over entire reactor active area (1300 × 1000 mm^2) is better than 10%.

Figure 11 shows five-point average thicknesses and five-point bandgap values for the array of 5 × 5 silicon wafers, with mean values of thickness $< d > = 94.7$ and deviation 3.4% and with mean value of optical gap $<E_g> = 1.72$ eV and deviation $<\Delta E_g> =$HJT 1.1%. These characteristics meet uniformity requirement for fabrication of HJT cells on wafer distributed over entire reactor area with thin films incorporated in the device structure.

Performance characteristic of "Hevel" HJT solar cell module is shown in **Figure 12**. Comparison of this characteristic with that for HJT module reported by "Meyer-Burger" is presented in **Table 3**.

One can see in **Table 3** that the values reported by "Hevel Solar" are still less than those of "Meyer Burger." However, this difference partially comes from using full square wafers in MB modules, which results in reduced dead space area and corresponding gain in current value. It should be noted that it is difficult to perform correct comparison because of the difference in the form of silicon wafers (not always reported), in normalization over area taking

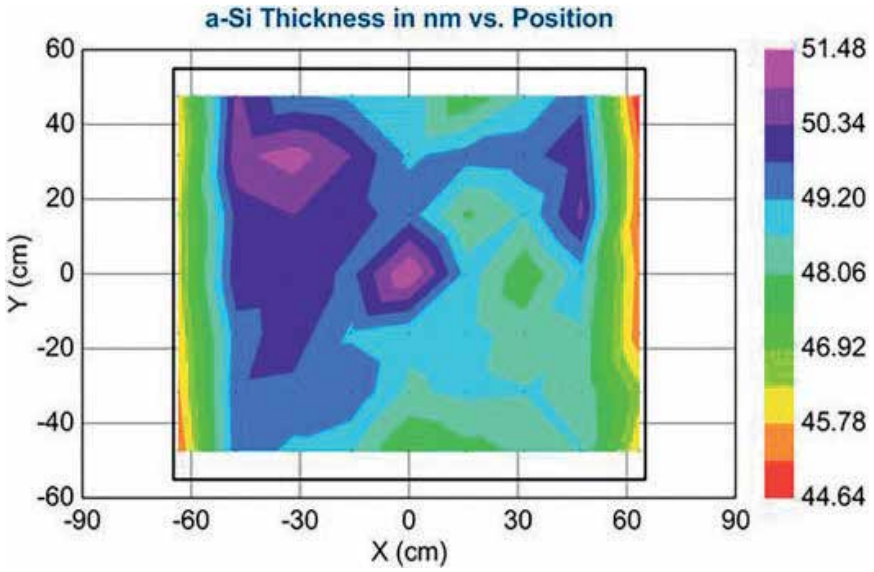

Figure 10. Thickness mapping for a-Si:H films deposited on glass substrate. Data are obtained by spectral ellipsometry.

into account substrate area occupied by contact grid or not, and so on resulting in some uncertainties when comparing the devices.

Interesting data on outdoor 1-year testing of "Hevel Solar" HJT modules can be found in Ref. [13] (**Figure 12**).

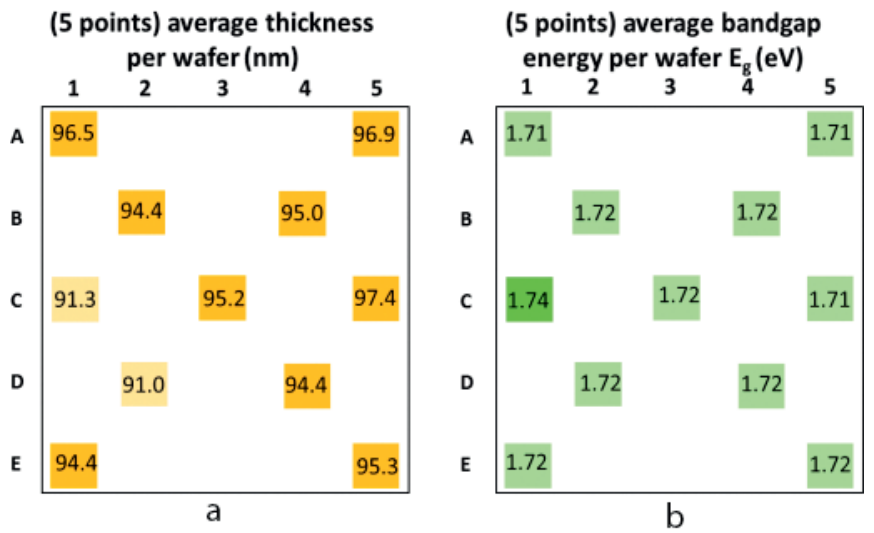

Figure 11. Thickness and optical gap mapping for the films deposited on silicon substrate (wafer dimensions 156 × 156 mm^2). Data are obtained by spectral ellipsometry.

Module	Pmax	Vmp (V)	Imp (A)	Voc (V)	Jsc (A)	FF (%)	PCE (%)
"Hevel Solar"	317	35.78	8.85	43.88	9.44	76.4	19.1
"Meyer Burger"	329	37.04	8.89	44.28	9.66	77.0	19.8

Note: PCE indicated in table are effective values calculated with integral module area without subtraction area occupied by electrode stripes and elements of hermetization and assembling.

Table 3. Comparison of performance characteristics of 1600 × 1000 mm² HJT modules consisted of 60 single wafer cells made by "Hevel Solar" and "Meyer Burger" [12].

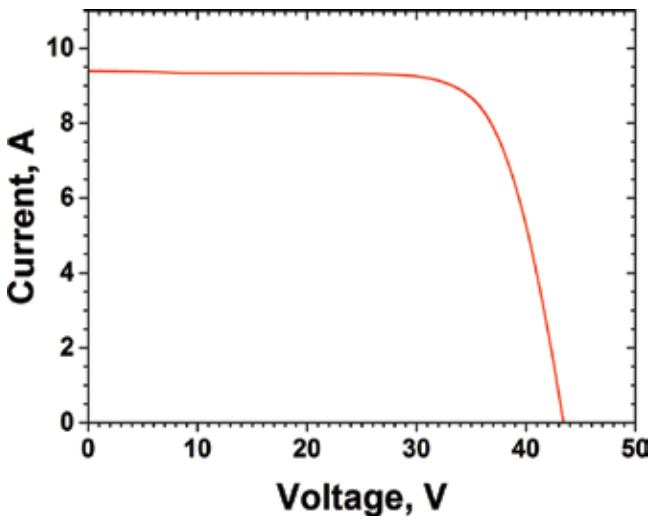

Figure 12. Current-voltage I(U) characteristics of HJT module 1600 × 1000 mm² (60 cells 156 × 156 mm²), developed by RDC TF TE and fabricated by "Hevel solar".

6. Summary and outlook

We have briefly described a successful transformation of technology for thin film solar cell modules (1000 × 1300 mm²) with efficiency 11% to heterojunction technology (HJT) for c-Si solar cell modules (1000 × 1600 mm²) with efficiency around 20% with employing the same essential equipment for PECVD materials. Now, the developed HJT modules are commercially produced by "Hevel Solar" (Russia) [14].

PECVD technique being principal in HJT module fabrication for both passivation and growth of semiconductor films is very versatile technology with high potential for further material engineering.

Well-known theoretical estimation of efficiency for one bandgap material c-Si gives value around PCE ≈ 30–34%, while record value achieved in 2017 by "Kaneka Corp." (Japan) is about PCE ≈ 27%. Thus some potential still exists for PCE increase for one gap c-Si HJT solar

cells, which can be realized by improving passivation, electrodes, improving short wavelength collection by frontal interface, and so on.

General road to increase conversion efficiency is related to multijunction (MJ) design and fabrication of PV structures comprising materials with different bandgaps adjusted for harvesting maximum of solar energy spectrum. This has been demonstrated by MJ solar cells with A_3B_5 semiconductors provided the highest reported values of PCE = 46% [15].

Therefore, MJ approach should be taken into account considering further development of HJT c-Si solar cells with efficiency above 34%.

Conflict of interest

Hereby the authors declare a lack of any known for them conflicts of interests.

Nomenclature

PECVD	plasma-enhanced chemical vapor deposition
ATR IR	attenuated total reflection infrared spectroscopy
FTIR	Fourier transform spectroscopy
HJT	heterojunction technology (devices, solar cells)
IBC	interdigitated back contact (solar cells)
PCE, η,	power conversion efficiency
E_g	optical gap, eV
PV	photovoltaic (structures, solar cells)
TCO	transparent conductive oxide
ITO	indium tin oxide
i-a-SiH	un-doped amorphous silicon
p-a-Si:H	p-doped amorphous silicon
n-a-Si:H	n-doped amorphous silicon
c-Si, (p)c-Si, (n)	c-Si un-doped crystalline silicon, p- and n-doped crystalline silicon
i-μc-SiH	un-doped microcrystalline silicon
n-μc-SiH	n-doped microcrystalline silicon
p-μc-SiH	p-doped microcrystalline silicon
p-SiC:H	p-doped microcrystalline silicon carbide

BSF	back surface field (solar cell)
CZ silicon	silicon fabricated by Czochralski technique
PERC	passivated emitter (usually p-Si) and rear cell (silicon solar cell).
PERL	passivated emitter rear locally diffused (silicon solar cell).
PERT	passivated emitter rear totally diffused (solar cells).
J_{sc}	short circuit current density, mA/cm^2.
I_{sc}	short circuit current, A
U_{oc}	open circuit voltage, V, mV
R_{sh}	effective shunt resistance, Ohm
R_s	effective series resistance, Ohm
STC	standard test conditions, output performance conditions used by most manufactures AM 1.5, I = 1000 W/m^2, T = 25°C
TMB	trimethyl boron

Author details

Eugenii Terukov[1], Andrey Kosarev[2]*, Alexey Abramov[1] and Eugenia Malchukova[3],

*Address all correspondence to: akosarev@inaoep.mx

1 R and D Center TFTE, Polytechnicheskaya, St-Petersburg, Russia

2 National Institute for Astrophysics, Optics and Electronics, Puebla, Mexico

3 Ioffe Institute, Polytechnicheskaya, St-Petersburg, Russia

References

[1] Int. Technology Roadmap for Photovoltaics, 2016 Results, 8th ed. September 8, 2017

[2] Yamamoto K, Yoshikawa K, Yoshida W, Irie T, Kawasaki H, Konishi K, Asatani T, Kanematsu M, Mishima R, Nakano K, Uzu H, Adachi D. High efficiency a-Si/c-Si heterojunction solar cells. In: Program Book, 27th International Conferece on Amorphous and Nanocrystalline Semiconductors, August 21-25, 2017, Seoul, Korea. p. 92

[3] Shah AV, Schade H, Vanecek M, Meier J, Vallat-Sauvain E, Wyrsch N, Kroll U, Droz C, Bailat J. Thin-film silicon solar cell technology. Progress in Photovoltaics: Research and Applications. 2004;**12**:113-142. DOI: 10.1002/pip.533

[4] Yang J, Banerjee A, Guha S. Triple junction amorphous silicon alloy solar cell with 14.6 initial and 13.0% stable conversion efficiencies. Applied Physics Letters. 1997;**70**:2975-2977

[5] Batzner DL, Habermann D, Andreeta L, Frammelsberger W, Kramer R, Lachenal D, Legradic B, Meixenberger J, Papet P, Strahm B, Wahli G. Heterojunction solar cells on p-type mono-Si wafers and the flexibility of HJT processing. In: Proceedings of 31rd European PV Solar Energy Conference and Exhibition. September 14-18, Hamburg, Germany. 2015. pp. 788-790. DOI: 10.4229/EUPVSEC20152015-2AV.3.33

[6] Release: Multicrystalline Silicon Solar Cell with 21.9 Repcent Efficiency: Fraunhofer ISE Again Holds World Record. February 20, 2017. pp. 1-3. Available from: https://www.ise.fraunhofer.de/content/dam/ise/en/documents/press-releases/2017/0617_ISE_e_PR_Weltrekord%20multi%20Si%20Solarzelle_final.pdf [Accessed: January 30, 2018]

[7] Masuko K, Shigematsu M, Hasiguchi T, Fujishima D, Kai M, Yoshimira N, Yamaguchi T, Ichihashi Y, Mishima T, Matsubara N, Yamanishi T, Takahama T, Taguchi M, Maruyama E, Okamoto S. Achievemnt of more than 25% conversion efficiency with crystalline silicon heterojunction solar cell. IEEE Journal of Photovoltaics. 2014;**2014**(11):1433-1435. DOI: 10.1109/JPHOTOV.2014.2352151

[8] Zhao J, Wang A, Altermatt A, Wenham PP, Green MA. 24% efficient PERL silicon solar cell: Recent improvements in high efficiency silicon cell research. Solar Energy Materials and Solar Cells. 1996;**41/42**:87-99

[9] Green MA, Blakers AW, Zhao J, Milne AM, Wang A, Dai X. Characterizzation of 23 percent efficient silicon solar cells. IEEE Transactions on Electron Devices. 1990;**37**(2):331-336

[10] Kherodia A, Panchal AK. Analysis of thickness-dependent optical parameters of a-Si:H/nc-Si:H multilayer thin films. Materials for Renewable and Sustainable Energy. 2017;**6**:23. DOI: 10.1007/s40243-017-0107-3

[11] Andronikov D, Abramov A, Abolmasov S, Emtsev K, Ivanov G, Nyapshaev I, Orekhov D, Semenov A, Shelopin G, Terukova E, Terukov E, Belkova N, Dubrovskiy A, Ishmuratov P, Ivanov A, Saykin D, Shakhray I, Smirnov A, Tarasov V, Timakov V, Tomchinskiy A, Kekelidze G. A successful conversion of silicon thin film solar cell module production to high efficiency heterojunction technology. In: Proceedings of 33rd European PV Solar Energy Conference and Exhibition, September 25-29, Amsterdam, Netherlands. 2017. pp. 732-735

[12] De Wolf S. High Efficiency Silicon Heterojunction Solar Cells: Properties, Processing, and Perspectives. Available from: http://www.icans26.org/icans26/EN/_SharedDocs/Downloads/EN/abstract%20de%20wolf.pdf?__blob=publicationFile [Accessed: Jan 29, 2018]

[13] Emtsev K, Malevsky D, Andronikov D, Abramov A, Yakovlev S, Titov A, Terukov E, Orekhov D, Bulygin B, Dubrovskiy A. Proceedings of 33-rd European PV Solar Energy Conference and Exhibition, September 25-29, 2017. Amsterdam, Netherlands. 2017. pp. 1628-1631

[14] Hevel achieves heterojunction cells with 22.8% efficiency as plant ramps. https://www.pv-tech.org/news/hevel-achieves-heterojunction-cells-with-22.8-efficiency-as-plant-ramps. [Accessed 2018- 01-29]

[15] Green MA, Hishikawa Y, Warta W, Dunlop ED, Levi DH, Hohl-Ebinger J, Ho-Baillie AWY. Progress in Photovoltatics: Research and Applications. 2017;**25**:668-676. DOI: 10.1002/pip.2909

Chapter 6

Perovskite-Structured Photovoltaic Materials

Ming-Chung Wu and Yin-Hsuan Chang

Additional information is available at the end of the chapter

http://dx.doi.org/10.5772/intechopen.74997

Abstract

In this chapter, we provide the historical background and overview of perovskite-structured photovoltaic materials. The organolead halide perovskite-structured solar cell is considered as one of the most promising photovoltaic technologies due to its rapid progress in power conversion efficiency. However, the existence of lead in perovskite-structured photovoltaic materials raises toxicological and environmental issues. Therefore, many scientists focused on discovering new materials that can replace the lead and improve photovoltaic performance. There are still some issues to be overcome before commercialization of perovskite-structured photovoltaic materials. The fast degradation phenomenon under humidity or constant irradiation is one such issue. The hysteresis phenomena could cause inaccurate estimation of power conversion efficiency. The choice of selective contact also plays an important role in obtaining high performance device. Therefore, the interaction between each layer should be considered. Overall, we reported on state-of-the-art perovskite-structured photovoltaic materials and discussed the essential factor for fabricating high-performance perovskite-structured solar cells.

Keywords: perovskite, photovoltaic, active layer, lead-reduced, solar cells

1. Introduction

For several decades, there has been substantial development in solar cells. Solar cells can be roughly divided into three generations, including (1) single-crystalline and polycrystalline silicon solar cells, (2) thin film solar cells (CIGS, CdTe, and amorphous silicon), and (3) new generations of solar cells (organic solar cells, dye-sensitized solar cells, and perovskite solar cells). Among these solar cells, the third generation of solar cells, which adopt organic materials and nanotechnology, shows relatively low cost; the fabrication process is relatively uncomplicated. Therefore, the booming of research interest in third generation solar cells has taken placed. Particularly,

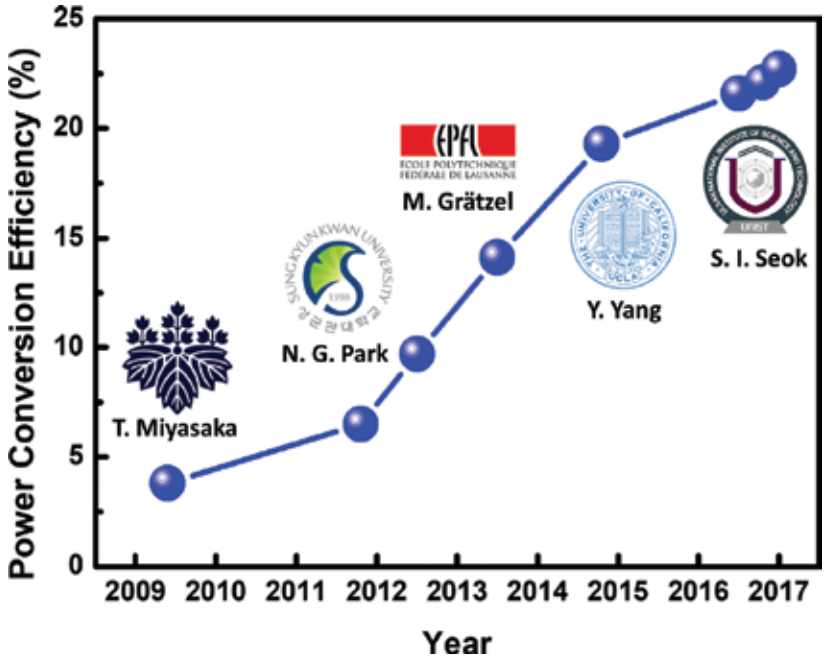

Figure 1. Efficiency chart of perovskite-structured solar cells.

Figure 2. The number of articles related to the "perovskite solar cell" in the science citation index (SCI;Thomson Reuters) from 2012 to 2017.

the perovskite solar cells (PSCs), bearing the advantages including feasible solution process, low material cost, and rapid progress of efficiency, has drawn much attention. As one of the third generation photovoltaic material, the development of the perovskite solar cells (PSCs) efficiency chart, which was recorded by the National Renewable Energy Laboratory (NREL), is illustrated in **Figure 1** [1]. In 2009, Japanese scientist T. Miyasaka's group first reported methylammonium lead halide ($CH_3NH_3PbI_3$) as a light absorber in dye-sensitized solar cells with a power conversion efficiency (PCE) of 3.8% [2]. After that, many research groups dedicated to constructing various perovskite solar cells in the past eight years. By the apparent increase in the number of publications per year (**Figure 2**), PSCs have attracted the scientific community's attention for several years. Owing to the scientists' contribution, the PCE of PSCs has rapidly improved, and the latest record is up to 22.7% by the S. I. Seok group. However, the presence of lead ions in perovskite-structured materials is so toxic to both environment and human community that it will be an obstacle for possible commercialization. During the fabricating process of PSCs, the commonly used solvents, such as dimethylformamide (DMF, C_3H_7NO), acetonitrile (ACN, C_2H_3N), and chlorobenzene (CB, C_6H_5Cl), are also highly toxic, which may even result in cancer. Therefore, future development will focus on the reduction of lead content and the use of low-hazardous solvents.

2. What is perovskite?

In 1839, Gustav Rose, a German mineralogist, first discovered a kind of calcium titanium oxide mineral, composed of calcium titanate ($CaTiO_3$), in the Ural Mountains of Russia [3]. This mineral was then named after Russian mineralogist Lev Perovski. However, the material currently used in perovskite solar cells is not $CaTiO_3$ but a material that has a similar crystal structure to perovskite. The chemical formula of this material is commonly denoted as $\mathbf{ABX_3}$, where **A** is a monovalent cation, **B** is a bivalent metal cation, and **X** is a halogen anion. Furthermore, the **A** cation with larger ionic radii occupying a cuboctahedral site is shared with 12 **X** anions. The 6 **X** anions surround the **B** cation with the smaller ionic radii occupying octahedral coordination and form a stable structure. The octahedron will connect with each other by corning sharing arrangement, and the center of each octahedron is the location of **A** cation [4]. The crystal structure of ABX_3 is shown in **Figure 3**.

The proposed perovskite structure and its stability can be determined by Goldschmidt's tolerance factor (TF) and octahedral factor (μ) [5]. For an ideal cubic perovskite, the unit cell axis, *a*, is geometrically related to the ionic radii and can be described with Eq. (1):

$$a = \sqrt{2}(R_A + R_X) = 2(R_B + R_X) \tag{1}$$

where R_A, R_B, and R_X are the ionic radii of **A** cation, **B** cation, and **X** anion, respectively. Goldschmidt's tolerance factor is the ratio of the two expressions of the unit cell axis. The equation of TF is as follows.

$$TF = \frac{(R_A + R_X)}{\sqrt{2}(R_B + R_X)} \tag{2}$$

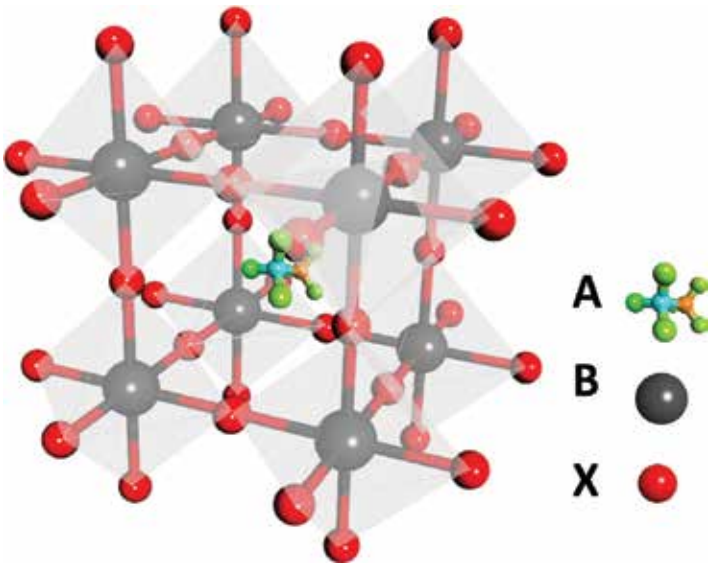

Figure 3. Crystal structure of an organic–inorganic metal halide perovskite.

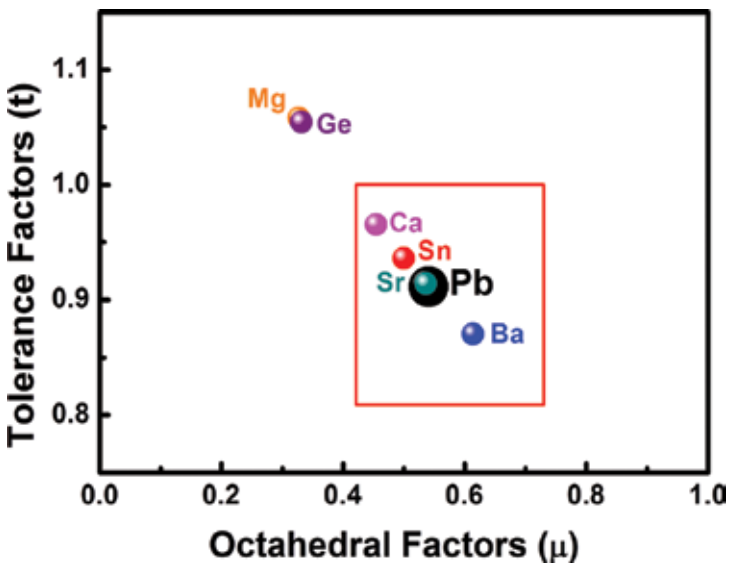

Figure 4. Comparison of calculated octahedral and tolerance factors for metal cations as a candidate for replacing toxic lead.

The perovskite structure is stable when the TF is in the range of $0.82 < TF < 1.00$. The octahedral factor calculated by Pauling's rule can determine the coordination numbers of the metal cation and the halogen anion. The equation of the octahedral factor is described in Eq. (3).

$$\mu = \frac{R_B}{R_X} \tag{3}$$

For the stable perovskite structure, the coordination number is 6, and the corresponding μ will be in the range of $0.414 < \mu < 0.732$. Calculating the tolerance factor and the octahedral factor could be an effective way to construct a new structural map leading to new principles of the formability of perovskite compounds.

To further complement the suitable metal cation candidates to replace toxic lead in perovskite while not to destroy its structure, **Figure 4** summarizes the comparison of tolerance and octahedral factors based on Goldschmidt's rule for non-toxic alkaline-earth metal cations. The homovalent substitution of Pb to alkaline-earth metal cations shows that it can meet the requirement of not only the charge balance but also the tolerance factor of Goldschmidt's rule in perovskite. As a result, alkaline-earth metal cations are widely considered as suitable candidates for replacing toxic lead.

3. Development of perovskite-structured photovoltaic materials

Perovskite-structured photovoltaic materials can be divided into four groups according to the demand of the research objectives. The first group, organolead halide perovskite, is used to improve the power conversion efficiency up to its theoretical limit ~31%. The second group is lead-free perovskite. The purpose of the lead-free perovskite-structured material is to find an alternative to replace the toxic lead. The third group is lead-reduced perovskite-structured material. Owing to the unstable performance of lead-free perovskite, partial substitution of lead can not only reduce the lead content but also retain the power conversion efficiency. The last group, two-dimensional (2D) perovskite-structured material, with the presence of hydrophobic alkyl ammonium, exhibits good moisture resistance. In this section, we provide a report of the four types of perovskite-structured photovoltaic materials and their relevant applications.

3.1. Organolead halide perovskite-structured materials

Up to now, the organolead halide perovskite is still the highest performance material for PSCs. The high performance perovskite-structured solar cells are commonly based on $MAPbI_3$, where MA is CH_3NH_3. To obtain high efficiency, one of the effective approach is to improve the grain boundaries of $MAPbI_3$ thin film. The grain boundary is a critical factor of charge carrier kinetics and recombination, and thus influences the photovoltaic performance. It is believed that less non-radiative pathways in grain boundaries can lead to higher photovoltaic performance. However, formation of grain boundaries is unavoidable while the $MAPbI_3$ is forming on the substrate during the solution process. Therefore, the N. G. Park group reported a grain boundary healing process and achieved a PCE of 20.4% [6]. The grain boundary healing process involves adding a slight excess of MAI to the precursor coating solution of $MAPbI_3$. After spin coating the non-stoichiometric precursor solution with slightly excess MAI, the excess MAI will not influence the crystal structure but form MAI on the surface of the $MAPbI_3$ grain. This MAI film prevents carrier recombination at the grain boundaries and also maximizes the extraction ability of the electron and hole.

Another notable organolead halide perovskite solar cell is based on $FA_{1-x}MA_xPbI_{3-\gamma}Br_\gamma$. The architecture of PSCs, deposition process, and compositional manipulation have been seen as

important factors for high-efficiency PSCs. The S. I. Seok group devoted themselves to overcoming these obstacles. They proposed a sandwich-type architecture consisting of $CH_3NH_3PbI_3$ perovskite as a light harvester on mesoporous TiO_2 and achieved a PCE of 12% [7]. Then, they demonstrated a solution-based process to deposit a uniform and dense perovskite layer. The adoption of γ-butyrolactone and dimethyl sulfoxide (DMSO) mixed solvent followed by toluene drop-casting will form an intermediate phase, CH_3NH_3I–PbI_2–DMSO, which leads to the formation of a uniform layer and significantly enhances the PCE to 16.2% with no hysteresis [8]. They also developed a two-step process based on an intramolecular exchange between organic cations and DMSO molecules to fabricate $FAPbI_3$-based PSCs with 20.2% of PCE [9]. To date, the S. I. Seok group have combined the contributions mentioned earlier and modified the content of iodide in $FAPbI_3$ for efficient PSCs as shown in **Figure 5**. The addition of iodide ion by a two-step process can decrease the deep-level defects that are seen at the nonradiative recombination centers and improve the PCE to 22.1% [10].

3.2. Lead-free perovskite-structured materials

The development of lead-free perovskite-structured absorbers for solar cells is an important step toward commercializing this technology. For the perovskite-structured solar cells, lead is a critical component in the archetypical $FA_{1-x}MA_xPbI_{1-\gamma}Br_\gamma$ material. However, the presence of lead has raised questions as to whether toxicology issues will become problematic in the future for widespread deployment of PSCs [11]. Among various metal, tin is seen as the most viable metal to replace lead in perovskite-structure materials. The H. J. Snaith group reported the first completely lead-free $CH_3NH_3SnI_3$ perovskite solar cell prepared on a mesoporous TiO_2 scaffold with a PCE of 6.4% [12]. Although Sn shows excellent carrier mobility, the instability state of Sn^{2+} also makes it prone to become metallic in ambient air. Furthermore, the significant difference between Sn-based perovskite and Pb-based perovskite is the crystallizing condition; Sn-based perovskite crystallizes without heating and can suppress the formation of the uniform film. All of the aforementioned factors have become obstacles for fabricating high-efficiency lead-free PSCs.

Sn-based lead-free perovskite-structured materials still have some problems that make it lag behind lead-contained PSCs. For instance, the Sn vacancies with low formation energy lead to high-doped holes, which will cause severe carrier recombination in PSCs. Zhao et al. reported

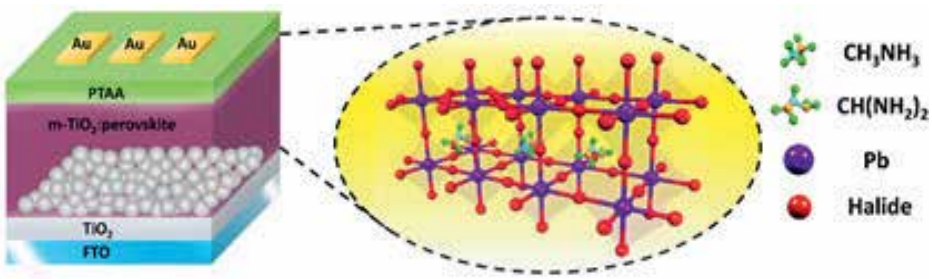

Figure 5. Schematic diagram of a perovskite device and crystal structure based on $FA_{1-x}MA_xPbX_3$ as an active layer.

$FA_xMA_{1-x}SnI_3$ served as the light harvesting layer with SnF_2 employed as an additive in DMSO [13]. Mixing cations such as MA and FA is a conventional method in the composition engineering to improve the PSCs performance. The addition of additives to perovskite precursor solution can reduce the doped-hole density and enhance the stability of Sn-base PSCs. Due to the fast crystallization of $MASnI_3$, which makes it difficult to control the film morphology, DMSO is further introduced to the perovskite precursor solution. Adding DMSO is seen as a critical step because it will react with SnI_2 and form an intermediate phase, $SnI_2{\cdot}3DMSO$, that suppresses the fast crystallization and thus obtains a homogeneous film. Up to date, the lead-free perovskite-structured material, $FA_{0.75}MA_{0.25}SnI_3$, with SnF_2 as an additive can achieve a PCE of 8.12% as shown in **Figure 6**.

3.3. Lead-reduced perovskite-structured materials

Although lead-free perovskite-structured photovoltaic materials solve the toxicity issues, efficiency is sacrificed for the replacement of lead. Partial substitution of lead in perovskite-structured materials is the alternative solution which can not only reduce the toxicity but also maintain the power conversion efficiency. Many literature indicates that owing to the facile oxidation of Sn^{2+} to Sn^{4+}, lead-free $CH_3NH_3SnI_3$ perovskite-structured material usually exhibits reduced efficiency and lack of reproducibility [14]. Therefore, many scientists attempted to prepare perovskite film with partial replacement of lead. The M. G. Kanatzidis group fabricated a perovskite material with 50% of Sn doping concentration ($CH_3NH_3Sn_{0.5}Pb_{0.5}I_3$), and found that doping Sn into the perovskite active layer can efficiently regulate the band gap of the perovskite material from 1.55 to 1.17 eV [15]. With the tunable band gap, it is also observed that light absorption extends to the near-infrared region. In addition, $CH_3NH_3Sn_{0.5}Pb_{0.5}I_3$ shows superior film coverage and better film morphology, which ensures connectivity between grains and overcomes short-circuiting and charge leaking issues.

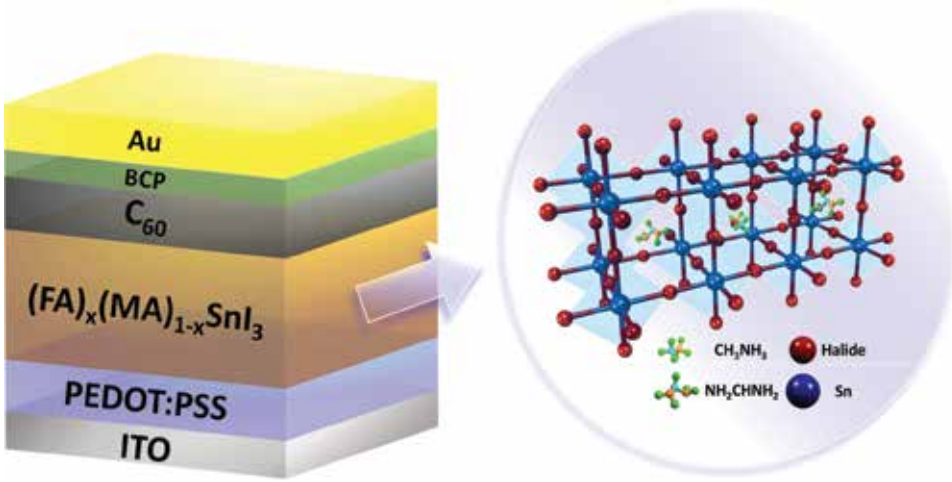

Figure 6. Schematic diagram of a perovskite device and crystal structure based on $FA_xMA_{1-x}SnX_3$ as an active layer.

The J. Navas group reported a theoretical study on partially replaced Pb^{2+} in $CH_3NH_3PbI_3$ with Sn^{2+}, Sr^{2+}, Cd^{2+}, and Ca^{2+} [16]. By doping the dopant into the perovskite-structured material, the different crystal structure and band gap will further affect the optical properties. In addition, the change in band gap mainly depends on the crystal structure of the perovskite-structured material. Undoped perovskite-structured material in company with the dopant of Sn^{2+}, Sr^{2+}, and Cd^{2+} is present in the tetragonal crystalline structure. In the case of Ca^{2+} doped perovskite, the predominant crystalline phase is a cubic phase. The values of the band gap with different dopants is in the trend of Sr^{2+} (1.50 eV) < Cd^{2+} (1.54 eV) < $CH_3NH_3PbI_3$ (1.57 eV) ≈ Sn^{2+} (1.57 eV) for the tetragonal structure and Ca^{2+} (1.52 eV) < $CH_3NH_3PbI_3$ (1.57 eV) for the cubic structure. With the greater ionic nature of the dopant–iodine interaction, a lower band gap can be obtained. By understanding the characteristic of the dopant, the growth of highly lead-substituted PSCs and high-efficiency PSCs will become a breakthrough for the commercialization in the near future.

The M.-C. Wu group adopted four kinds of alkaline–earth metal cations, including Mg^{2+}, Ca^{2+}, Sr^{2+}, and Ba^{2+}, to replace lead cations partially [17]. Among the four alkaline-earth metals, Ba^{2+} is most suitable for Pb^{2+} replacement in perovskite films; it also exhibits high power conversion efficiency. The Ba^{2+}-doped perovskite films that can be processed in the environment containing moisture (1.0% relative humidity) are stable. At the optimal 3.0 mol% Ba^{2+} replacement, the PCE of the fabricated solar cell is increased from 11.8 to 14.0%, and the PCE of champion devices is as high as 14.9% with increased storage stability (**Figure 7**).

3.4. Two-dimensional perovskite-structured materials

The three-dimensional (3D) perovskite-structured material shows outstanding power conversion efficiency owing to its tremendous advantage, including long carrier diffusion lengths for electrons and holes, small exciton binding energy, appropriate band gap, and high extinction coefficient. However, moisture instability results from the hygroscopic nature of MA and suppresses the commercialization of 3D PSCs. The two-dimensional (2D) perovskite-structured

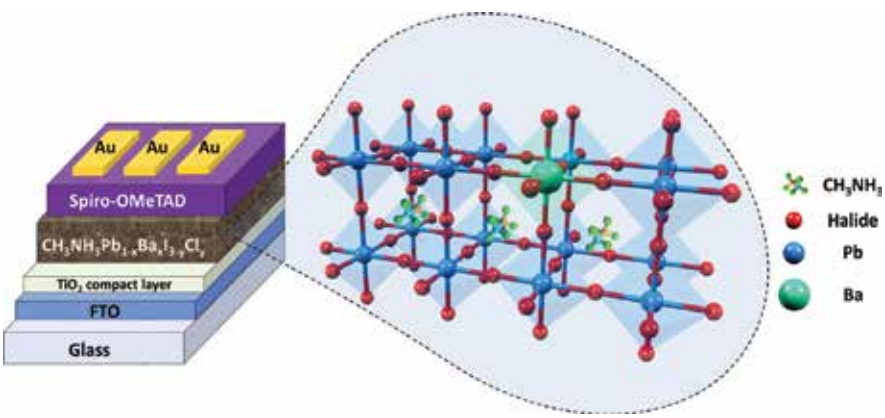

Figure 7. Schematic diagram of a perovskite device and crystal structure based on $CH_3NH_3Pb_{1-x}Ba_xX_3$ an active layer.

http://dx.doi.org/10.5772/intechopen.74997

material based on $(BA)_2(MA)_{n-1}Pb_nI_{3n+1}$, where BA is a long-chain aromatic alkylammonium cation, opens a new trend for optoelectronic devices. Its long organic side group with hydrophobic property seems to be beneficial for improving moisture stability. The inorganic layer of the 2D structure stack with each other by intercalated bulky alkylammonium cations and maintain structural integrity by weak van der Waals forces [18]. The band gap and the thickness of the 2D layer can be tuned by increasing the n values. For $n = 1$ structure, the 2D perovskite is a simple structure with the thinnest layer. At $n = \infty$, the structure becomes the typical 3D perovskite structure. An attempt to introduce 2D perovskite into the solid-state solar cell as a light-absorbing material showed poor efficiency (~4.0%) [19]. The poor device efficiency can be explained by the difficult charge transport in the out-of-plane direction. The long-chain organic cation between the conducting inorganic layers is similar to the insulating spacing layers. The H. Tsai group overcame this obstacle by fabricating near-single-crystalline thin films with the hot-casting process; they reported a PCE of 12.52% with no hysteresis [20]. It also shows outstanding light-soaking stability and moisture resistance that retains over 60% of its initial PCE after 2250 h irradiation without encapsulation. Furthermore, when the 2D PSCs is encapsulated, it shows no degradation after irradiation or under humidity. The significant breakthrough of power conversion efficiency for 2D PSCs is attributed to the enhanced charge mobility, which is facilitated by the near-perfect vertical orientation of the $\{(MA)_{n-1}Pb_nI3_{n+1}\}^{2-}$ layer. The 2D perovskite layer fabricated using the hot-casting technique can form a high-quality film, which is ideal for a photovoltaic device. Compared with conventional spin-coating film, the hot-casting technique provides a uniform and substantially large grain size film that is much more reflective. The film also presents a low density of pinhole, which is profitable for improving efficiency. Based on these results, the S. Liu group further doped Cs^+ into a 2D perovskite to replace MA^{2+} (**Figure 8**) [21]. The Cs doping enhances the optoelectronic properties attributed to the improvement of charge transfer kinetics, charge carrier mobility, and decreased of trap density. With this modification, the PCE can be successfully improved from 12.52% to 13.7%.

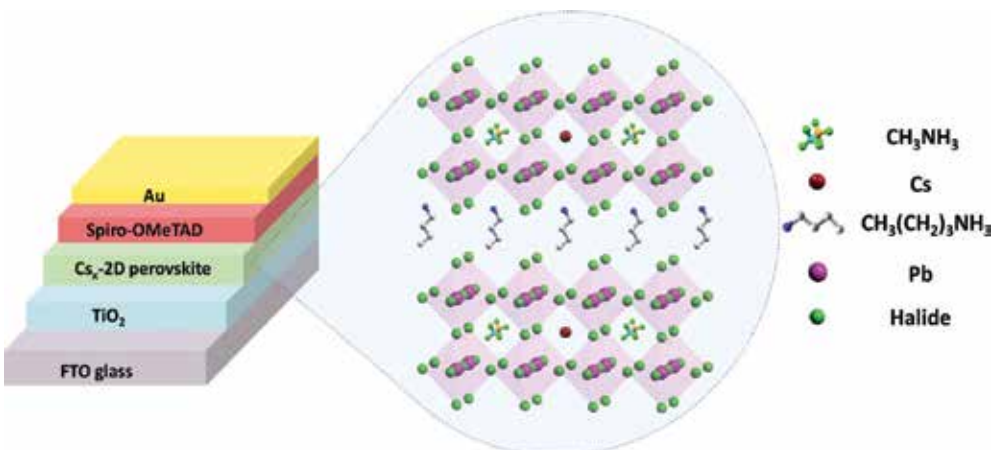

Figure 8. Schematic diagram of a perovskite device and crystal structure based on Cs^+ doped 2D perovskite as an active layer.

4. Current issues and future challenges

To date, perovskite-structured photovoltaic devices have presented considerable progress to achieve high efficiency. However, many issues have to be overcome before the commercialization. The fast degradation phenomenon under humidity or constant irradiation bears the brunt. The other crucial factor is the presence of J − V hysteresis. With the existence of the hysteresis phenomena, the accuracy of power conversion efficiency will fall under suspicion. The fundamental mechanisms of the efficient carrier transport in perovskite should also be considered. The complication of the synthesis methods and the construction of PSCs make it much more difficult to overcome these obstacles. Recently, many researchers have devoted lots of effort to address these issues and adapt the properties of corresponding materials.

4.1. Instability under humidity

The stability of PSCs is dominated by lots of factors, such as high humidity, intense illumination, and increased temperature [22]. Exposure to such a severe condition leads to the rapid degradation of efficiency and restricts PSCs from outdoor application. Many studies have revealed that when the $MAPbI_3$ is exposed to moisture, it will immediately degrade into methylammonium (MA), hydrogen iodide (HI), and lead iodide (PbI_2) owing to its solubility in water [23]. Hence, how to effectively prevent the invasion of moisture in the environment should be considered thoroughly. Prior to developing the encapsulations material, it is important to understand what happens during the degradation. $CH_3NH_3PbI_3$ taken as an example of the degradation mechanism of perovskite is shown as follows:

$$CH_3NH_3PbI_{3(s)} \leftrightarrow PbI_{2(s)} + CH_3NH_3I_{(aq)} \tag{4}$$

$$CH_3NH_3I_{(aq)} \leftrightarrow CH_3NH_{2(aq)} + HI_{(aq)} \tag{5}$$

$$4HI_{(aq)} + O_{2(g)} \leftrightarrow 2I_{2(aq)} + H_2O_{(l)} \tag{6}$$

$$HI_{(aq)} \overset{h\nu}{\leftrightarrow} H_{2(g)} + I_{2(s)} \tag{7}$$

First, the $CH_3NH_3PbI_3$ will degrade into PbI_2 and CH_3NH_3I owing to the sensitivity to water. The formation of CH_3NH_3I results in the co-existence of CH_3NH_3I, CH_3NH_2, and HI toward the progress of equilibrium reaction. After that, the HI tends to decompose in two ways, redox reaction and photochemical reaction. Based on the aforementioned equilibrium reactions, it is easy to understand that not only the moisture in the environment but also the oxygen and UV radiation affect the stability severely [24]. The design of the encapsulant should consider the permeation mechanisms of the organic and inorganic materials. For an organic polymer encapsulant, gas or vapor permeates into the PSCs by the typical solution—the diffusion model. Although an organic polymer encapsulant possesses lots of advantages including flexibility, conformability, and processability, the permeability of gas is too high, which is not

conducive to PSCs. In the case of inorganic material, it provides a barrier toward permeant penetration. Defect-free inorganic thin films as encapsulant material show the characteristic of brittleness, which will not be break resistant to moisture conditions [25]. Therefore, constructing a material consisting of both organic and inorganic materials can combine both advantages and meet the flexibility and gas barrier conditions.

4.2. J-V hysteresis phenomena

In the characterization of photovoltaic performance, a hysteretic response appears with different scanning conditions; thus the accuracy of the cell efficiency is doubted. The photocurrent density-voltage (J-V) hysteresis behavior will be affected by scanning direction, scanning rate, and applied voltage [26]. The hysteresis J-V behavior remains a challenge for the advancement of PSCs. Here are some situations that result in erroneous device efficiencies. For operating in different scanning directions, the forward scan that holds at short-circuit conditions to open circuit voltage conditions tends to have a lower efficiency than holding at the reverse scan. Hence, the forward scan is inclined to underestimate the power conversion efficiency of PSCs. In contrast, the reverse scan tends to overestimate the power conversion efficiency. If the scan rate of measuring the device is faster than its response time, hysteretic behavior will also be deteriorated. While holding at the reverse scan, the efficiency increases with the increasing scan rate. On the other hand, the efficiency measured at the forward scan decreases with the increasing scan rate. Moreover, the J-V hysteresis phenomenon becomes more intense under the faster scan rate in both scanning directions. Another important factor that can also affect the J-V hysteresis is the starting biases. The tendency is similar to the previous condition. The more positive the starting voltage holding at the reverse scan, the higher the efficiency can be measured; whereas, while holding at the forward scan, the more negative the starting voltage, the lower the efficiency of PSCs can be recorded. The existence of J - V hysteresis plays a crucial role in the accuracy of power conversion efficiency; hence, many scientists have dedicated research to searching for the solution. One of the possible methods of J - V hysteresis elimination is to measure the device with a slow scan rate. That hysteresis influenced by applied voltage can be solved by light-soaking at different biases was reported by the M. D. McGehee group [27]. Prior to the characterization, the precondition for perovskite-absorber devices with different biases presents a significant effect on the photovoltaic performance. The short-circuit current density, fill factor, and power conversion efficiency under reverse scan can be suppressed by light-soaking with a more negative bias. In contrast, the photovoltaic performance under the forward scan will be enhanced by light-soaking with a more positive bias. Hence, the declined performance under the reverse scan and the increased performance under the forward scan prevent PSCs from the J-V hysteresis phenomenon.

4.3. Carrier transport behavior

Although a perovskite-structured active layer presents high efficiency of light-harvesting behavior, finding the suitable electron transport layer (ETL) and hole transport layer (HTL) is a critical issue for improving the performance of the photovoltaic device. After solar irradiation, an electron-hole pair will be generated at the perovskite-structured active layer. How to

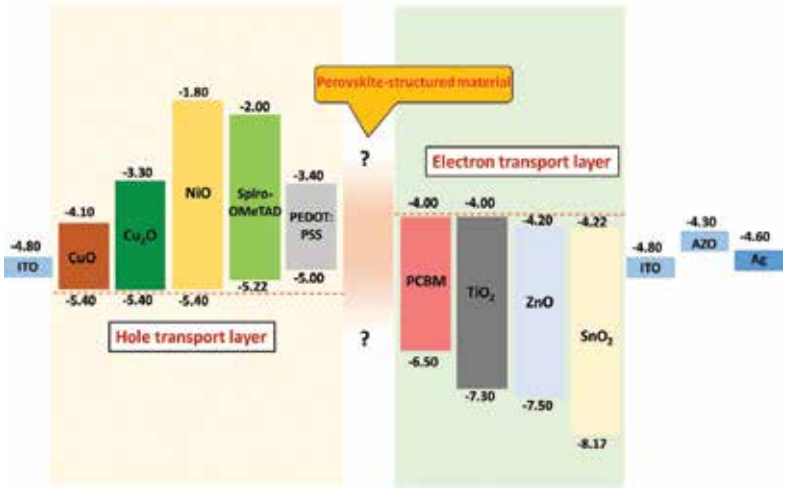

Figure 9. Energy band diagram of different electron and hole transport layers with respect to perovskite-structured photovoltaic devices.

transport the electron and hole efficiently to ETL and HTL, respectively, has been discussed thoroughly. Therefore, selecting the appropriate materials for the carrier transport layer is considered as a primary issue to prevent charge recombination and diminish energy loss at the interface between the perovskite active layer and ETL or HTL. In recent studies, the electron transport materials and the hole transport materials have been explored to construct an optimal band alignment for achieving high efficiency [28–30].

A good electron-transporting material should exhibit (1) good electron mobility to facilitate electron collection, (2) wide band gap for not hindering the absorption behavior of the perovskite active layer, and (3) both the valence band/conduction band should be lower than that of perovskite-structured material to promote electron migrate to ETL and block the hole to transport. Metal oxides, such as TiO_2, ZnO, and SnO_2, are widely applied as ETLs, especially TiO_2, owing to their electrical and optical properties [31]. A good hole-transporting material should exhibit (1) efficient hole mobility to promote hole collection, (2) the valence band/conduction band both should be higher than the perovskite-structured active layer to promote hole migration to HTL and further transport to the electrode, and (3) there should be photochemical stability. The most widely-explored materials for HTL has been divided into 3 groups: (1) small molecules (e.g., spiro-OMeTAD), (2) inorganic materials (e.g., CuI, CuSCN, NiO, etc.), and (3) conducting polymers (e.g., P3HT, PEDOT, PTAA, etc.) [32, 33]. **Figure 9** examines the proposed band alignment for the commonly used materials for ETL and HTL which is helpful for understanding interface properties and constructing high-efficiency perovskite-structured photovoltaic devices.

5. Conclusion

Perovskite-structured photovoltaic materials attract a lot of interest due to its facile fabrication process and rapid progress in device performance. A series of perovskite-structured

photovoltaic materials with high power conversion efficiency, including (1) organolead halide perovskite-structured materials, (2) lead-free perovskite-structured materials, (3) lead-reduced perovskite-structured materials, and (4) two-dimensional perovskite-structured materials, are reported herein in detail. Many problems that occur with these materials must be overcome before commercialization. It has been proved that the element in perovskite-structured material plays an important role in enhancing stability under humidity or constant irradiation and achieving high power conversion efficiency. Numerous alternative materials for ETL and HTL have been discovered to facilitate carrier transport at perovskite-structured material interface/ETL and perovskite-structured material/HTL interface. If there is a breakthrough development in fabrication methods, enhancement of stability, and optimized device structure can be realized, the commercialization of environmental-friendly high-efficiency PSC will be in the near future.

Acknowledgements

The authors appreciate Prof. Wei-Fang Su, Prof. Yang-Fang Chen and Mr. Meng-Huan Jao at National Taiwan University for useful discussion and suggestions. The authors acknowledge the financial support from the Ministry of Science and Technology, Taiwan (MOST 106-2221-E-182-057-MY3, MOST 106-2119-M-002-030 and MOST 106-2632-E-182-001) and Chang Gung Memorial Hospital, Linkou (CMRPD2F0161 and BMRPC74).

Conflict of interest

There are no conflicts of interest to declare.

Author details

Ming-Chung Wu* and Yin-Hsuan Chang

*Address all correspondence to: mingchungwu@cgu.edu.tw

Department of Chemical and Materials Engineering, College of Engineering, Chang Gung University, Taoyuan, Taiwan

References

[1] Research Cell Record Efficiency Chart [Internet]. 2017. Available from: https://www.nrel.gov/pv/assets/images/efficiency-chart.png [Accessed: January 27, 2018]

[2] Kojima A, Teshima K, Shirai Y, Miyasaka T. Organometal halide perovskites as visible-light sensitizers for photovoltaic cells. Journal of the American Chemical Society. 2009;**131**: 6050-6051. DOI: 10.1021/ja809598r

[3] Giorgi G, Yamashita K. Organic-inorganic halide perovskites: An ambipolar class of materials with enhanced photovoltaic performances. Journal of Materials Chemistry A. 2015;**3**:8981-8991. DOI: 10.1039/C4TA05046K

[4] Johnsson M, Lemmens P. Crystallography and chemistry of perovskites. In: Kronmueller H, Parkin S, editors. Handbook of Magnetism and Advanced Magnetic Materials. Hoboken, New Jersey: John Wiley & Sons, Ltd; 2007. DOI:10.1002/9780470022184.hmm411

[5] Mehmood U, Al-Ahmed A, Afzaal M, Al-Sulaiman FA, Daud M. Recent progress and remaining challenges in organometallic halides based perovskite solar cells. Renewable and Sustainable Energy Reviews. 2017;**78**:1-14. DOI: 10.1016/j.rser.2017.04.105

[6] Son D-Y, Lee J-W, Choi YJ, Jang I-H, Lee S, Yoo PJ, Shin H, Ahn N, Choi M, Kim D, Park N-G. Self-formed grain boundary healing layer for highly efficient CH_3 NH_3 PbI_3 perovskite solar cells. Nature Energy. 2016;**1**:16081. DOI: 10.1038/nenergy.2016.81

[7] Heo JH, Im SH, Noh JH, Mandal TN, Lim C-S, Chang JA, Lee YH, Kim H-J, Sarkar A, Nazeeruddin MK, Grätzel M, Seok SI. Efficient inorganic–organic hybrid heterojunction solar cells containing perovskite compound and polymeric hole conductors. Nature Photonics. 2013;**7**:486-491. DOI: 10.1038/nphoton.2013.80

[8] Jeon NJ, Noh JH, Kim YC, Yang WS, Ryu S, Seok SI. Solvent engineering for high-performance inorganic–organic hybrid perovskite solar cells. Nature Materials. 2014;**13**:897-903. DOI: 10.1038/nmat4014

[9] Yang WS, Noh JH, Jeon NJ, Kim YC, Ryu S, Seo J, Seok SI. High-performance photovoltaic perovskite layers fabricated through intramolecular exchange. Science. 2015;**348**:1234-1237. DOI: 10.1126/science.aaa9272

[10] Yang WS, Park B-W, Jung EH, Jeon NJ, Kim YC, Lee DU, Shin SS, Seo J, Kim EK, Noh JH, Seok SI. Iodide management in formamidinium-lead-halide–based perovskite layers for efficient solar cells. Science. 2017;**356**:1376-1379. DOI: 10.1126/science.aan2301

[11] Liang L, Gao P. Lead-free hybrid perovskite absorbers for viable application: Can we eat the cake and have it too? Advanced Science. 2017;**5**:1700331. DOI: 10.1002/advs.201700331

[12] Noel NK, Stranks SD, Abate A, Wehrenfennig C, Guarnera S, Haghighirad A-A, Sadhanala A, Eperon GE, Pathak SK, Johnston MB, Petrozza A, Herz LM, Snaith HJ. Lead-free organic-inorganic tin halide perovskites for photovoltaic applications. Energy & Environmental Science. 2014;**7**:3061-3068. DOI: 10.1039/C4EE01076K

[13] Zhao Z, Gu F, Li Y, Sun W, Ye S, Rao H, Liu Z, Bian Z, Huang C. Mixed-organic-cation tin iodide for lead-free perovskite solar cells with an efficiency of 8.12%. Advanced Science. 2017;**4**:1700204. DOI: 10.1002/advs.201700204

[14] Liu C, Li W, Fan J, Mai Y. A brief review on the lead element substitution in perovskite solar cells. Journal of Energy Chemistry. 2017;**000**:1-13. DOI: 10.1016/j.jechem.2017.10.028

[15] Hao F, Stoumpos CC, Chang RPH, Kanatzidis MG. Anomalous band gap behavior in mixed sn and pb perovskites enables broadening of absorption spectrum in solar cells. Journal of the American Chemical Society. 2014;**136**:8094-8099. DOI: 10.1021/ja5033259

[16] Navas J, Sanchez-Coronilla A, Gallardo JJ, Hernandez NC, Pinero JC, Alcantara R, Fernandez-Lorenzo C, De los Santos DM, Aguilar T, Martin-Calleja J. New insights into organic-inorganic hybrid perovskite $CH_3NH_3PbI_3$ nanoparticles. An experimental and theoretical study of doping in Pb^{2+} sites with Sn^{2+}, Sr^{2+}, Cd^{2+} and Ca^{2+}. Nanoscale. 2015;**7**:6216-6229. DOI: 10.1039/C5NR00041F

[17] Chan S-H, Wu M-C, Lee K-M, Chen W-C, Lin T-H, Su W-F. Enhancing perovskite solar cell performance and stability by doping barium in methylammonium lead halide. Journal of Materials Chemistry A. 2017;**5**:18044-18052. DOI: 10.1039/C7TA05720B

[18] Chen S, Shi G. Two-dimensional materials for halide perovskite-based optoelectronic devices. Advanced Materials. 2017;**29**:1605448. DOI: 10.1002/adma.201605448

[19] Cao DH, Stoumpos CC, Farha OK, Hupp JT, Kanatzidis MG. 2D homologous perovskites as light-absorbing materials for solar cell applications. Journal of the American Chemical Society. 2015;**137**:7843-7850. DOI: 10.1021/jacs.5b03796

[20] Tsai H, Nie W, Blancon J-C, Stoumpos CC, Asadpour R, Harutyunyan B, Neukirch AJ, Verduzco R, Crochet JJ, Tretiak S, Pedesseau L, Even J, Alam MA, Gupta G, Lou J, Ajayan PM, Bedzyk MJ, Kanatzidis MG, Mohite AD. High-efficiency two-dimensional Ruddlesden–popper perovskite solar cells. Nature. 2016;**536**:312. DOI: 10.1038/nature18306

[21] Zhang X, Ren X, Liu B, Munir R, Zhu X, Yang D, Li J, Liu Y, Smilgies D-M, Li R, Yang Z, Niu T, Wang X, Amassian A, Zhao K, Liu S. Stable high efficiency two-dimensional perovskite solar cells via cesium doping. Energy & Environmental Science. 2017;**10**:2095-2102. DOI: 10.1039/C7EE01145H

[22] Cheacharoen R, Rolston N, Harwood D, Bush KA, Dauskardt RH, McGehee MD. Design and understanding of encapsulated perovskite solar cells to withstand temperature cycling. Energy & Environmental Science. 2018;**11**:144-150. DOI: 10.1039/C7EE02564E

[23] Matteocci F, Cinà L, Lamanna E, Cacovich S, Divitini G, Midgley PA, Ducati C, Di Carlo A. Encapsulation for long-term stability enhancement of perovskite solar cells. Nano Energy. 2016;**30**:162-172. DOI: 10.1016/j.nanoen.2016.09.041

[24] Niu G, Guo X, Wang L. Review of recent progress in chemical stability of perovskite solar cells. Journal of Materials Chemistry A. 2015;**3**:8970-8980. DOI: 10.1039/C4TA04994B

[25] Seethamraju S, Ramamurthy PC, Madras G. Encapsulation for improving the efficiencies of solar cells. In: Viswanathan B, Subramanian V, Lee JS, editors. Materials and Processes for Solar Fuel Production. New York: Springer-Verlag; 2014. pp. 23-40. DOI: 10.1007/978-1-4939-1628-3_2

[26] Chen B, Yang M, Priya S, Zhu K. Origin of J–V hysteresis in perovskite solar cells. The journal of physical chemistry letters. 2016;**7**:905-917. DOI: 10.1021/acs.jpclett.6b00215

[27] Unger EL, Hoke ET, Bailie CD, Nguyen WH, Bowring AR, Heumuller T, Christoforo MG, McGehee MD. Hysteresis and transient behavior in current-voltage measurements of hybrid-perovskite absorber solar cells. Energy & Environmental Science. 2014;**7**:3690-3698. DOI: 10.1039/C4EE02465F

[28] Correa Baena JP, Steier L, Tress W, Saliba M, Neutzner S, Matsui T, Giordano F, Jacobsson TJ, Srimath Kandada AR, Zakeeruddin SM, Petrozza A, Abate A, Nazeeruddin MK, Gratzel M, Hagfeldt A. Highly efficient planar perovskite solar cells through band alignment engineering. Energy & Environmental Science. 2015;**8**:2928-2934. DOI: 10.1039/C5EE02608C

[29] Wang J-F, Zhu L, Zhao B-G, Zhao Y-L, Song J, Gu X-Q, Qiang Y-H. Surface engineering of perovskite films for efficient solar cells. Scientific Reports. 2017;**7**:14478. DOI: 10.1038/s41598-017-14920-w

[30] Zhou H, Chen Q, Li G, Luo S, Song T-B, Duan H-S, Hong Z, You J, Liu Y, Yang Y. Interface engineering of highly efficient perovskite solar cells. Science. 2014;**345**:542-546. DOI: 10.1126/science.1254050

[31] Mohamad Noh MF, Teh CH, Daik R, Lim EL, Yap CC, Ibrahim MA, Ahmad Ludin N, ARb MY, Jang J, Mat Teridi MA. The architecture of the electron transport layer for a perovskite solar cell. Journal of Materials Chemistry C. 2018;**6**:682-712. DOI: 10.1039/C7TC04649A

[32] Yu Z, Sun L. Recent progress on hole-transporting materials for emerging Organometal halide perovskite solar cells. Advanced Energy Materials. 2015;**5**:1500213. DOI: 10.1002/aenm.201500213

[33] Vivo P, Salunke J, Priimagi A. Hole-transporting materials for printable perovskite solar cells. Materials. 2017;**10**:1087. DOI: 10.3390/ma10091087

Chapter 7

Degradation Monitoring of Photovoltaic Plants: Advanced GIS Applications

Miguel de Simón-Martín, Ana-María Diez-Suárez, Laura-Álvarez de Prado, Alberto González-Martínez, Álvaro de la Puente-Gil and Jorge Blanes-Peiró

Additional information is available at the end of the chapter

http://dx.doi.org/10.5772/intechopen.75650

Abstract

In order to evaluate a photovoltaic (PV) plant performance, payback time, profitability and environmental impact, an analysis must be made of plant maintenance needs, module and wiring degradation, mismatches and dust effects and PV cell defects and faults. Although a wide range of studies can be found that show the theory and laboratory testing of how these circumstances may affect PV production, very few studies in the field have covered or quantified real degradation effects and faults using a systematic procedure. The authors have therefore reviewed the conditions of PV plants operating in Southern Europe, examining the most frequently found faults and types of degradation, and they look at how novel technologies, such as geographic information system (GIS) applications, can help maintainers, owners, and promoters to supervise and locate damaged PV modules and monitor their evolution and impact on plant working conditions. GIS applications in this field allow the organization of a geo-referenced database of the system, locating and supervising the thirds of each PV cell in the power plant. With this information, investors and maintainers can exert increased control on the PV plant performance and conduct better preventive maintenance measures. The examples given demonstrate that these sorts of applications can be applied both to large PV plants and to domestic installations.

Keywords: photovoltaics, PV plants, PV faults, geographic information system, PV supervision, maintenance

1. Introduction

The operation and maintenance of a photovoltaic (PV) power plant is of extreme importance to guarantee its optimal performance. Effective maintenance involves at the least semi-automatic analysis and alerts. In this way, the maintenance operator is capable of making immediate decisions to solve safety problems and minimize power losses [1].

Moreover, monitoring is not just a regular recording of data but involves a more detailed analysis in order to prevent possible malfunctions associated with power and, in the end, economic losses.

Thus, the development of automatic supervision tools to help maintainers to carry out an effective supervision of the power plant and, what is more important, to monitor the evolution of the modules behavior in an easy and feasible way is of great interest in the industry. Furthermore, the detection of operating failures in a timely fashion through the evaluation of panels over time means that automated monitoring is, in fact, absolutely necessary. Such monitoring will lead to the early replacement of poorly performing components, preventive maintenance policies, and better management of plants.

For device manufacturers, performance evaluations of their products can be used as a benchmark of their quality manufacturing processes. On the other hand, researchers and R&D divisions from companies can take advantage of such evaluations, using that information to identify future needs in the industry and to test real working conditions. For PV plant promoters and owners, realistic performance data is essential for investment decision-making.

Although several techniques for the detection of real and/or potential failures in the PV field can be found in the literature [2–4], few of them attempt to detect anomalies such as power loss, module failure, or health and safety dangers until after they occur and the effects are felt. These techniques, moreover, do not address preventative maintenance strategies or effective economical programs for the replacement of components. In addition, these systems do not integrate geo-references that may help to improve the application of preventative maintenance strategies.

New methodologies are needed to locate and analyze performance and malfunction of plant components on a global scale. Despite the great value of analysis carried out in the laboratory, it can often be of little help when applied to the real operation of maintenance plans. Test conditions in a laboratory may allow for a complete analysis of PV components, but owners can ill afford to close an entire installation or part thereof for equivalent testing in the field. Besides, laboratory test conditions are unlikely to fully typify working conditions in a real field. As such, laboratory test results and, more importantly, any conclusions drawn from them are likely to be decontextualized. On the other hand, carrying out systematic procedural techniques in the field under changing environmental and climatic conditions is in no way easy.

Integrated geographic information system (GIS) platforms will allow test-related information to be comprehensively organized and geo-referenced, providing significant benefits. One such benefit is the fact that the impact of a single defective component on the overall

performance of a plant can be analyzed. Predictive techniques can then be used to analyze deviations in the behavior of supposedly viable components and forecast possible outage in areas of the PV plant.

This chapter is organized into four further sections. First, a systematic review of the most common PV faults is undertaken. Then, the fundamentals of GIS and how they can be applied to PV maintenance and fault supervision are presented. In section three, the application of a GIS tool to both a large PV plant (100 kWp) and a domestic installation (9 kWp) is fully described and results of the implementation of both examples are shown. Finally, the last section includes the main conclusions and some future research directions.

2. Photovoltaic module defects and faults

Prior to going deeper into this topic, the term "failure" in the PV context must be properly defined. The bibliography defines a failure in a photovoltaic module as *an effect that degrades the module power output which is not reversed by normal operation or which, on the other hand, creates a safety issue.* Evidently, both of these effects can occur at the same time.

As such, degradation of wiring or modules, PV cell defects and malfunctions, dust, and mismatches can be considered to be failures of PV modules [5] and purely esthetic problems are not.

The following subsections describe briefly all potential PV module failures.

2.1. Delamination

This consists of the loss of adhesion between the glass, the encapsulation, the active layers, and the subsequent layers [6], which can cause loss of current (power) in the photovoltaic modules. Loss of adhesion may occur for various reasons. Large thin film modules and certain other types of modules sometimes contain an additional transparent conductive oxide (TCO) layer, which may lose adhesion with the adjacent glass layer [6]. If the loss of adhesion is due to contamination, perhaps from cleaning, or environmental factors, then delamination will often take place, followed by moisture entering and, in due course, corrosion. Delamination leads to reflection of light and a subsequent loss of power in the modules.

In most cases delamination can be detected by visual inspection, with the degree of layer detachment being quantified by use of a reflectometer. Some delaminations, however, cannot be identified in this way and so methods such as pulsed active thermography or lock-in thermography can be used, while smaller delaminations can be detected with ultrasound scanners and X-ray tomography. The latter methods are slow [7] but provide a much higher resolution.

2.2. Loss of adhesion in backsheet films

The multilayer composites that make up PV module backsheet films comprise three or more polymer layers. Outer layers provide resistance to weathering factors such as sunlight and humidity and are often made from fluoropolymers with polyvinyl fluoride (PVF), polyamide (PA), or polyethylene terephthalate (PET) [8] being popular choices.

Backsheet failures include yellowing, brittleness that leads to cracking, and delamination within the multilayer composite. Delamination and cracking allow water vapor and oxygen into the PV module and are considered to be the worst kind of failures within backsheets as they cause problems with isolation and subsequently can cause safety issues [9]. Water vapor critically affects degradation phenomena such as decomposition of the encapsulation, corrosion of the metal parts, and potential induced degradation (PID) of the PV modules. Such failures impact on the performance of a PV module and shorten its lifespan. Yellowing, on the other hand, has not been reported as having an influence on the electrical performance of modules.

2.3. Junction box faults and mechanical breakage

Junction boxes are attached to the back of modules and protect the connections to the external terminals. Bypass diodes in the junction boxes protect cells in a series when hot spots occur due to partial shadowing of the module [5]. The formation of moisture due to faulty adhesive can lead to wiring degradation that can be the cause of electrical arcing resulting in the potential for fire or threat to human life.

Mechanical breakages usually consist of cracks in the frame produced by poor handling or extreme winter snow loads.

2.4. Discoloration of the encapsulation material and bubble formation

Degradation of the encapsulation material (normally ethylene vinyl acetate or EVA) is an esthetic issue that does not usually affect the performance of a module. It can, however, lead to an average current loss of 0.5%/year or 0.8%/year for Si PV modules [10].

Rising temperatures, the photo-degradation of EVA by UV radiation, and the existence of molecular oxygen lead to the production of acetic acid and volatile gases, that are trapped within the module, and can produce delamination or the formation of bubbles [11].

The presence of acetic acid in a PV module is linked to several PV module failures due to its corrosive effects on cell metal, which may lead to an increased series resistance and hence losses in module performance [12, 13].

Some studies refer to discoloration as degradation rather than failure, as discoloration leads typically to lower performance but not necessarily to failure [6].

On the other hand, inappropriate temperatures or an excessively long lamination procedure [14] during the manufacturing of the photovoltaic module can cause bubbles of gas to be formed either as a direct or as an indirect consequence of melting and solidification processes (**Figure 1**). In **Figure 1(a)** an EVA discoloration can be appreciated while in **Figure 1(b)** we can observe an example of a bubble formed over a metal contact.

2.5. Cell cracks

PV cells are made of silicon so they are very brittle. Cell cracks are formed in different lengths and orientations in the substrate of the photovoltaic cells and often cannot be seen easily.

http://dx.doi.org/10.5772/intechopen.75650

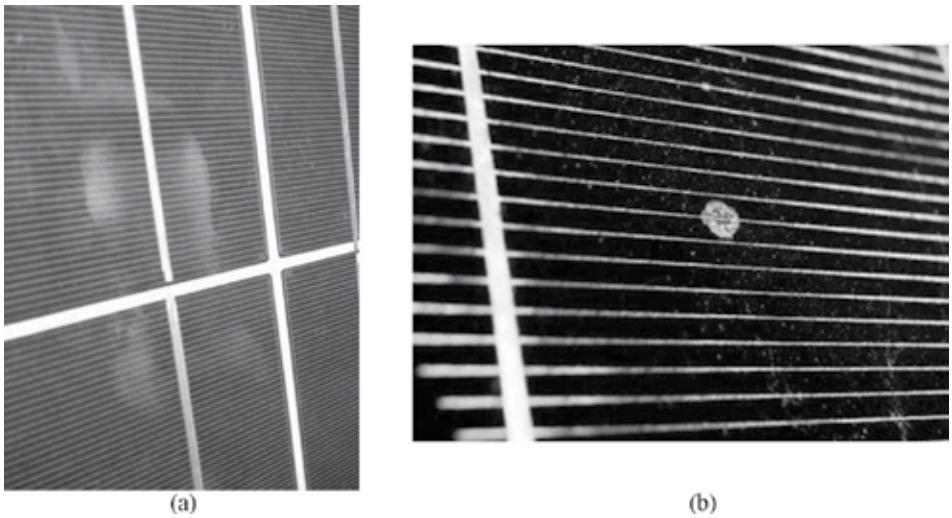

Figure 1. Examples of (a) EVA discoloration and (b) bubble formation.

Figure 2 shows a clear example. Cell cracks may occur during or after production. Major sources of cell cracks are during packaging and transport or during the reloading of PV modules and installation in the field.

Small cell cracks show a great tendency to develop into larger, wider cracks during operation of the solar module due to mechanical stress [15] from wind or snow load and thermomechanical stress [16] from temperature variations due to changes in weather and intermittent cloud cover.

An inactive cell area of 8% or more is unacceptable. Apart from the risk of power loss there is also the chance of hot spots being formed. This can happen when a cracked cell has a localized

Figure 2. Example of cracks in a PV cell.

reverse current path in the still active cell part. The cell may reverse bias and the full current will be able to flow along the localized path as a consequence of the missing cell area. This can cause hot spots and subsequently burn marks [17].

2.6. Snail tracks

Snail tracks are discolorations of the silver fingers on solar cells. A significant example can be seen in **Figure 3**. The effect looks like a snail has passed across the front glass of the PV module. The discoloration takes place on cell cracks that are not visible at the edge of the solar cell. This typically happens between 3 months and 1 year after installation of the PV modules [18]. Discoloration speed is initially dependent on seasonal and environmental conditions, such that snail tracks seem to spread faster during summer months and in hot climates [5]. PV modules affected by snail tracks have been compared with reference modules under laboratory conditions [19] and results showed a 40% reduction in maximum power under standard conditions with a 25% lower yield than expected when measured over a 30-day period.

2.7. Hot spots and burn marks

A typical and very common failure in silicon PV modules is burn marks. This failure occurs due to part of the module becoming very hot and can be because of ribbon breakage, solder bond failure, or localized heating from reverse current flow or other hot spots [5]. Burn marks can produce power losses and serious safety problems. They are usually located on or closed to the metal contacts of the PV solar cells, such as it can be seen in **Figure 4**.

Hot spots are areas in a photovoltaic module that have very high operating temperatures when compared to surrounding areas. This may be due to interconnection failures, defects in the cell, dispersion of characteristics between modules of a generator and between cells of the same module connected in series, potential-induced polarization in modules manufactured with novel techniques, or when a cell generates less current than other cells connected in series as a consequence of intermittent cloud cover or partial shading [20]. As a consequence, the cell becomes polarized (the voltage between the terminals becomes negative) and starts to dissipate the power generated by the other serial cells in the form of heat.

Figure 3. Example of a snail track over a PV cell.

http://dx.doi.org/10.5772/intechopen.75650

Recently, a new maximum power point tracking (MPPT) method was proposed to avoid the consequences of hot spots. It is based, firstly, on a bidirectional buck converter to control the operating point of each module and uses a boost converter to control the terminal voltage of each branch. Secondly, MPPT is modeled as an large-scale global optimization (LGSO), and a novel, multicontext, cooperatively coevolving particle swarm optimization (PSO) algorithm (CCPSO-m) is proposed to solve this large-scale problem [21].

2.8. Potential-induced degradation

Potential-induced degradation gives rise to power losses owing to the presence of eddy currents in the PV modules. Its effect can potentially reduce the power of the equipment [22].

The principal cause of these currents is reported to be voltage gaps between the ground and the module. In photovoltaic systems without a grounding system, this effect occurs when modules have a non-zero voltage, which is normally negative especially under high ambient humidity and/or temperatures and high voltage conditions [23].

2.9. Disconnected cells and string interconnected ribbons

Cell strings can become disconnected if string interconnected ribbons are weak, which may be caused by large deformations, by the quality of the welds during the production process, or by weak connections between the string and the ribbon. Small distances between cells can also contribute to interconnected ribbon breakage [5].

The consequences of this may be a broken cell interconnected ribbon and a subsequent decrease in maximum power point current [24] or a shunt by a cell interconnected ribbon and a subsequent decrease of open circuit voltage.

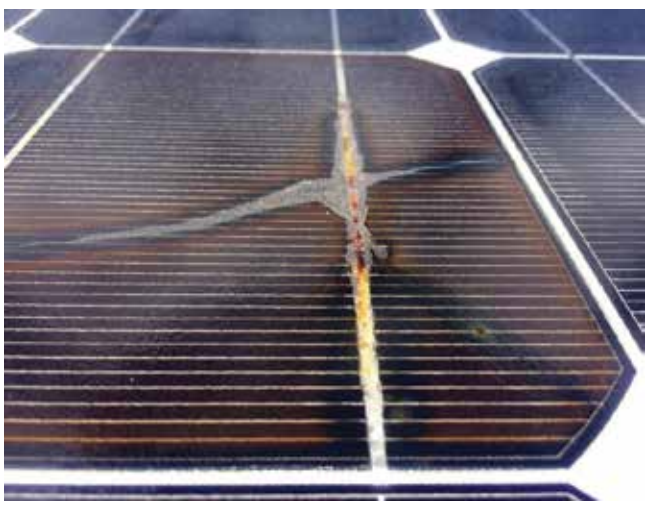

Figure 4. Example of a burn mark on a PV cell.

2.10. Defective bypass diode

Bypass diodes reduce the effects of intermittent cloud cover and partial shading on power generation by limiting reverse voltage potentials [5]. Power output is decreased significantly without bypass diodes and partial shading may cause local overheating, hot spots, and damage [25].

A new bypass system has been designed [26] allowing significant hot spot temperature reduction in both partial and full shading conditions. It relies on a series-connected power metal oxide semiconductor field effect transistor (MOSFET) that subtracts part of the reverse voltage from the shaded solar cell, thus acting as a voltage divider. The authors claim that it would be possible to cool up to 24°C with respect to the case in which standard bypass diodes are adopted.

2.11. Blue cells

This consists of the lightening of the dark blue tone of certain cells in the PV module. Some authors classify this as an esthetic defect, but others have noted that its appearance can cause a 17% yield loss under certain conditions [27].

3. Energy geographic information system applications

A geographic information system or GIS consists of a set of applications and programs that manage spatially referenced databases, which can be visualized through the use of maps [28]. It is a powerful and dynamic tool for the analysis of geographical and spatial data, which can also include non-spatial data.

A correctly implemented GIS tool provides comprehensive analysis of an area for any activity that entails a spatial component, meaning that GIS technology has wide application in resource management and can be an important tool in any decision-making task with a spatial element. GIS can thus be found applied to the development of solar atlas, resource location tools, and so on. Some authors have used GIS together with global positioning systems (GPS) and unmanned aerial vehicles (UAV) to propose efficient inspection and maintenance of PV plants [29].

3.1. Development of geographic information system tools for advanced photovoltaic plant supervision and management

The collection and compilation of a dataset of a number of PV power generation variables into a GIS tool for the easy visualization, location, and prediction of current problems in a PV power plant is of great worth. This involves the creation of a database and base map, and adequate procedures for systemizing data introduction and analysis, which in turn should lead to the simplification of the study of existing electrical and thermal defects.

Furthermore, the application of a GIS tool allows for the novel correlation of cell defects with not only power losses on the affected PV module but also with overall performance of the power plant.

http://dx.doi.org/10.5772/intechopen.75650

The complete PV power plant should first be introduced into the GIS software (ESRI ArcGIS) through aerial orto-photography before geometrical parameters are projected. The geographical position of the PV serial strings and limitation of plots can thus be set.

Furthermore, it is necessary to identify the exact position within the panel of any possible faults that may appear. For this reason, split installation of photovoltaic panels and the thirds of cells within each panel are taken into account. The maps have been geo-referenced by assigning them projected coordinates ETRS89 UTM 30 N.

PV modules are identified by their rack number and by a code that includes the serial string and the relative position of the string within the series.

A systematic procedure needs to be set up to identify the geographical position of a defect within a panel. A photovoltaic module is made up of 180 thirds of cells so the following nomenclature is suggested. Each cell in the panel can be split into 6 columns (A–F) and 10 rows (0–9). Each cell is, in turn, split into three thirds (X, Y, or Z). In this way, the position of a defect can be indicated in the third of the cell where it is located by an alphanumerical code (e.g., 4EY). **Figure 5** shows such an identifying code applied to a panel.

With the graphical part of the GIS tool delimited and the identification procedure for each PV cell established, a geo-referenced database or geo-database can be implemented. The geo-database consists of a set of various kinds of geographical datasets in a common file system folder. From this a comprehensive information model can be created to represent and manage all the geographical information related to the power plant. This information model is realized as a series of tables storing entity classes, raster datasets, and attributes.

The model can be divided into three sorts of information: measurements of electrical variables, graphic information (pictures and thermographs), and defects and their description. **Figure 6** shows the schematic diagram of the relational database that has been created. According to

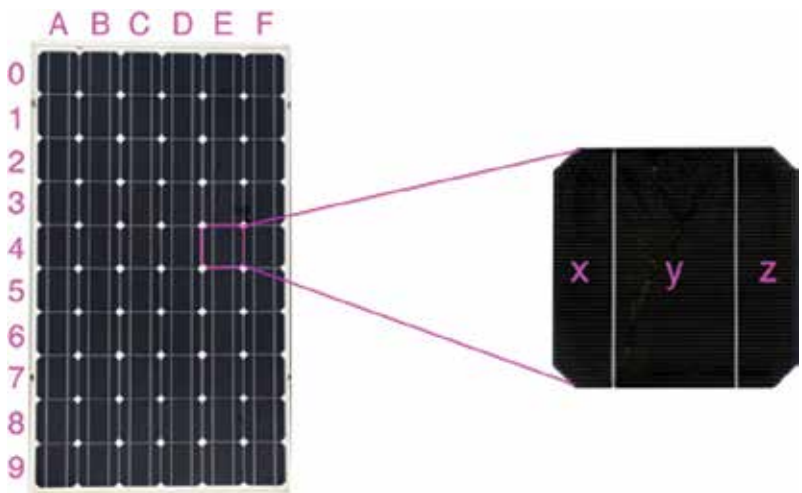

Figure 5. Adopted nomenclature for PV defect identification.

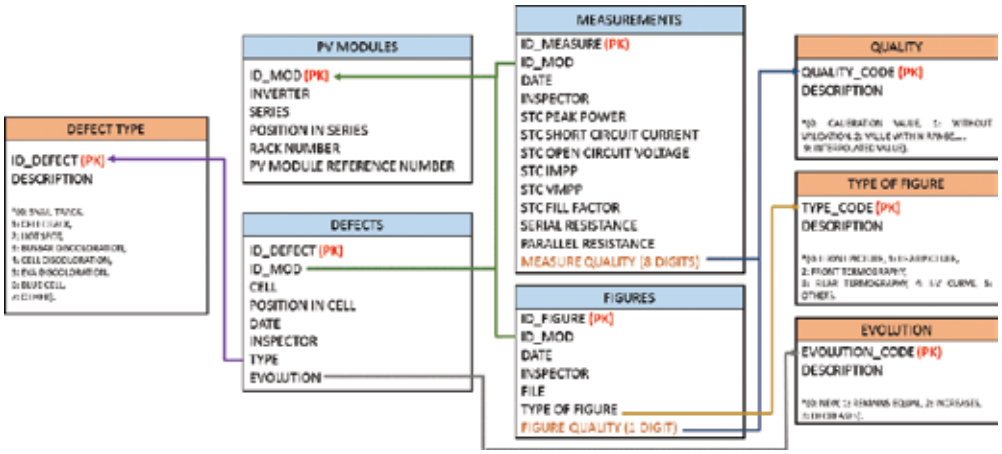

Figure 6. Schematic diagram of the database organization and relations.

the three sorts of information, the model has been organized into four main tables and four additional tables. The PV MODULES main table includes information related to a given PV module, such as its identifier code (ID_MOD) which is the primary key and uniquely identifies each record, the string series (SERIES), the inverter associated with the module (INVERTER), its relative position in the series (POSITION IN SERIES), its rack number (RACK NUMBER), and its manufacturing reference code (PV MODULE REFERENCE NUMBER).

The MEASUREMENTS main table includes the measured electrical variables that allow for analysis of the performance. Each measurement is assigned a unique identifier (ID_MEASURE) that relates each measurement record to the PV module using the ID_MOD. The date of the measurement (DATE) and the inspector who took the measurement (INSPECTOR) are also included. The installation date and factory settings of the module (FACTORY) can be included under the INSPECTOR setting. In order to assure an adequate analysis, the measurement quality (MEASURE QUALITY) is also included in the form of metadata, an eight-digit code described in the QUALITY auxiliary table. The quality code is a number between 0 and 9, that describes if the record is a calibration value (0), if the record has no validation (1), if the record has been checked for being in a suitable range (2), and so on. There is one digit for each measured electrical value.

The DEFECTS table records PV defects and faults. Each record shows the module affected (ID_MOD), the location code of the cell (CELL), which third of the cell is affected (POSITION IN CELL) along with the date (DATE), inspector recording the defect (INSPECTOR), type of defect (TYPE), and defect evolution within the module (EVOLUTION). The DEFECT TYPE auxiliary table records identifiers for the type of defect found in the form of a digit—0: snail track, 1: cell crack, 2: hot spot, 3: busbar discoloration, 4: cell discoloration, 5: EVA discoloration, 6: blue cell, and 7: other. The EVOLUTION field in the DEFECTS table is associated with the EVOLUTION auxiliary table. The following descriptors show the defect evolution in the PV module in this table—0: new defect or not detected before, 1: already detected but remains the same as the previous inspection, 2: has increased from the previous inspection, and 3: has decreased from the previous inspection.

Finally, graphic information can also be included in the form of front and rear photographs and thermographs of each analyzed module. Furthermore, diagrams and figures can also be stored such as the I-V curve obtained by a PV curve tracer. This information is recorded in the FIGURES table, which includes hyperlinks to files (FILE), the type of graphic information (TYPE OF FIGURE), and its quality (FIGURE QUALITY). The type of figure is also related to the TYPE OF FIGURE auxiliary table. Figure quality is especially pertinent in the case of thermographs and consists of a one-digit code with the same description as is found in the previously described QUALITY auxiliary table.

As shown in **Figure 7**, pictures, thermographs, and I-V curves are spatially referenced and associated with each module. This is extremely useful as it means graphic information can be spatially related to the measured attributes in each panel. Furthermore, all graphic information is available both from the geo-database and through the GIS map.

Inspection entails the characterization of the performance of a PV module by measurement of its I-V curve within normal working conditions and its extrapolation to standardized standard test conditions (STC) conditions (cell temperature of 25°C, incident global irradiance of 1000 W/m^2, and air mass of 1.5).

There must be absolutely no shadow on the PV modules during this process, as it can cause irregular thermal areas leading to a misinterpretation of the results. Furthermore, windy conditions should be avoided as thermal exchange by convection may also cause a diffuse thermal image.

The most favorable conditions for taking quality, representative thermal images is when the panel is working at maximum power, which generally occurs at noon with clear sky conditions [30]. This means that thermographs should be taken only when there is a minimum of 700 W/m^2 of

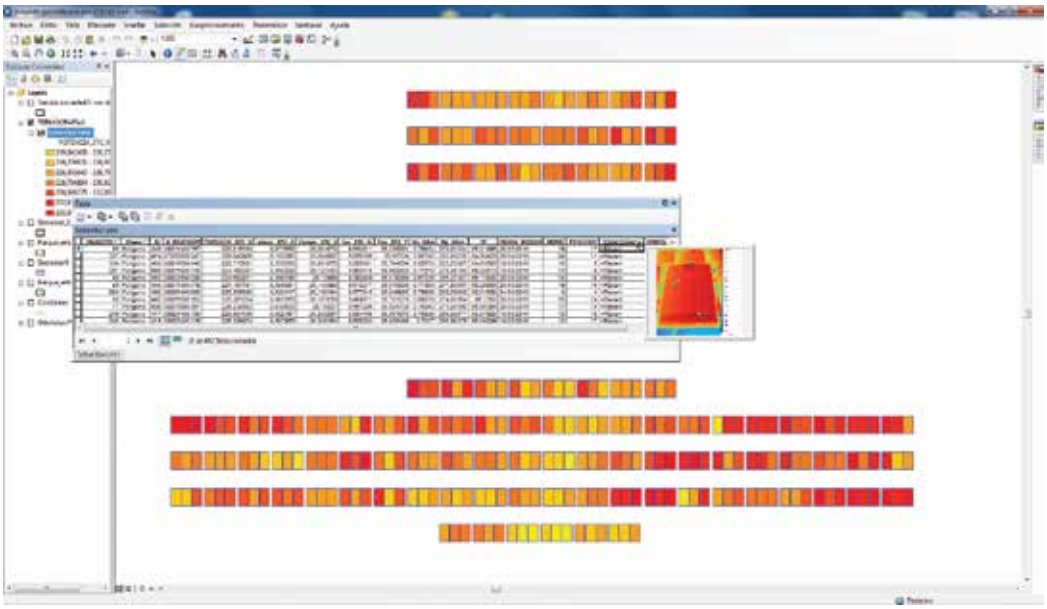

Figure 7. Instantaneous access to a PV module frontal thermography.

global irradiance on the horizontal surface. Furthermore, frontal and rear thermographs should be taken in order to minimize interference on the measurements due to reflections from the front of the PV module. However, special care needs to be taken when using rear thermographs for corrections, as temperatures may be higher due to a lack of thermal dissipation when compared to the front part [31].

Once the electrical measurements, fault detection, and graphic information have been obtained, all data can be compiled into a complete project constituting a GIS.

4. Examples

The GIS tool was applied to two case studies in Spain. The first was a fixed 108 kW peak power PV plant connected to the grid, which has been operating since mid-2008. The second was a fixed domestic 9 kW peak power PV plant installed on the rooftop of a family home. This installation has been in operation since the beginning of 2017.

4.1. Geographic information system applied to a 108 kWp PV power plant

The first case study is a commercial plant with 100 kW nominal power on the inverters and 108 kW peak power on the PV modules, operated by the Spanish company Sobarriba Leon 0. The PV modules are installed on fixed structures, pointing south, and inclined at 28 degrees to the horizontal. The PV field consists of 432 GFM 220-250 monocrystalline 250 Wp silicon modules manufactured by Wuxi Guofei Green Energy Source Co. Ltd. They are organized in 24 strings with 18 modules on each string. There are six electrical protection boxes for the strings in total. **Figure 8** shows all electrical parameters for each PV module, while **Figure 9** shows the PV faults log.

The effective application of the GIS tool allows the observation of all electrical parameters in a holistic way. As shown in **Figure 8(a)**, critical peak power performances can be easily detected among more than 400 PV modules. Other electrical parameters, such as fill factor, open circuit voltage, or short circuit current dispersion, can also be observed in the context of the facilities.

4.2. Geographic information system applied to a 9 kWp PV power plant

This is a home PV power plant operated by Himalaya Sol, a Spanish company. It consists of a fixed 9 kW peak power plant on the roof of a family home. It began operating in February 2017 and is made up of 36 GFM 220-250 monocrystalline silicon modules manufactured by Wuxi Guofei Green Energy Source Co. Ltd. The modules are fixed with a tilt of 32 degrees oriented to 6 degrees east and have a peak power of 250 W per unit. A P300 optimizer from Solar Edge is used to optimize power output given that the installation is affected by shadows due to the architectural configuration. The PV modules are arranged in 3 serial strings of 13, 13, and 10 modules, respectively.

Figure 10 shows all electrical parameters for each PV module, while **Figure 11** shows the PV faults log.

http://dx.doi.org/10.5772/intechopen.75650

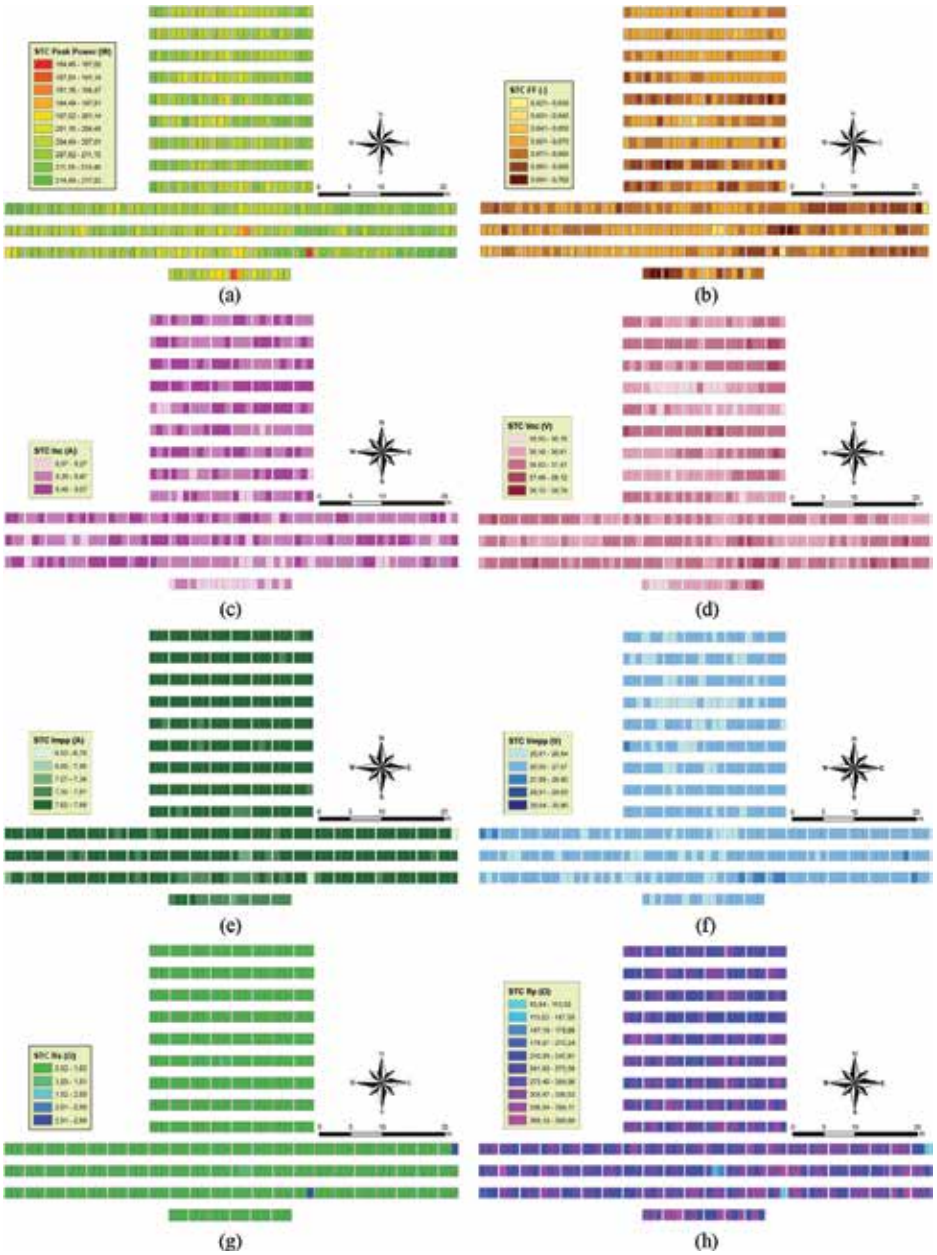

Figure 8. Electrical parameter distributions: (a) STC peak power, (b) STC fill factor (c) max. power voltage, (d) max. power current, (e) open circuit voltage, (f) short circuit current, (g) serial resistance, (h) parallel resistance (108 kWp PV plant).

Once again, it is considerably easier for staff to supervise and monitor the PV plant state. However, distribution of electrical parameters may be less significant as only 36 PV panels are included in this installation.

Results for the GIS implementation in the 9 kWp home power plant do not have much relevance as of the moment. Due to the fact that the installation only recently started working,

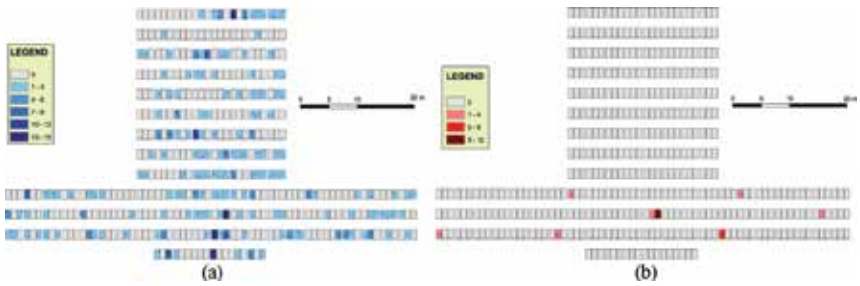

Figure 9. PV faults and defects in the 108 kWp PV plant: (a) snail tracks (b) hot spots and burn marks.

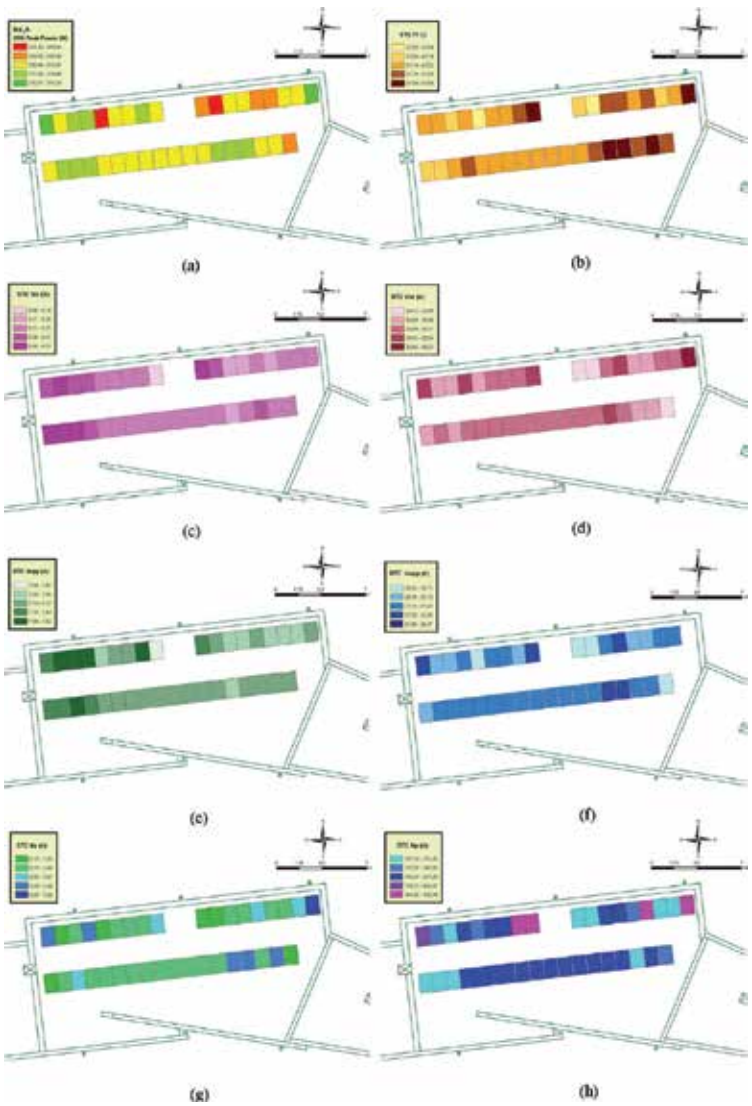

Figure 10. Electrical parameter distributions: (a) STC peak power, (b) STC fill factor (c) max. power voltage, (d) max. power current, (e) open circuit voltage, (f) short circuit current, (g) serial resistance, (h) parallel resistance (9 kWp PV plant).

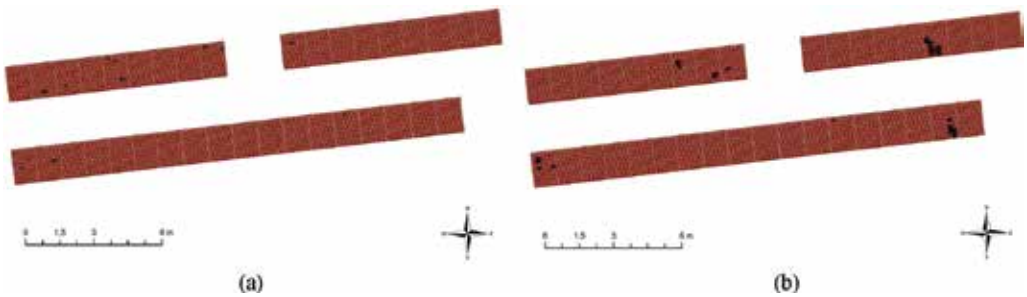

Figure 11. PV faults and defects in the 9 kWp PV plant: (a) snail tracks (b) cell discolorations.

almost no degradation has yet been observed. However, **Figure 11(a)** and **(b)** show some snail tracks and cell discoloration that might lead to the modules needing future maintenance. The distribution of these defects does not appear homogeneous and seems to be concentrated at string series extremes.

5. Conclusions

The GIS tool presented here has shown itself to be of great use when analyzing degradation effects on a PV field, the location of the most common PV defects, and their overall correlation with the plant. Although useful information was found in both case studies, the application of GIS to large plants seems to be more viable than for small installations.

The GIS tool is extremely useful for supervising the degradation of electrical parameters in a power plant and the evolution and distribution of defects in a PV field. Researchers and maintainers are encouraged to use it on their installations and compare results. We will continue to add periodical measurements and inspections to the geo-database and the real degradation effects of the PV field will then be completely analyzed. Such analysis will lead to more economical and effective maintenance and replacement strategies.

A systematic organization and analysis of measurements thanks to the implementation of GIS applications not only allows preliminary preventive maintenance actions to be carried out, such as replacing damaged PV modules, redistributing PV modules according to their performance, and developing specific supervision, cleaning, and maintenance procedures for modules affected by PV faults, but also makes feasible the supervision of the degradation of electrical parameters in the power plant and the evolution and distribution of defects in the PV field.

Acknowledgements

This chapter has been published in open access thanks to the support and funding of the Laboratorio de Inspección Técnica de la Escuela de Minas (LITEM) and the University of León (Spain). The authors wish to thank everybody who contributed to the project, especially

Sobarriba León 0 and Himalaya Sol, and to the reviewers for increasing the overall quality of the manuscript with their valuable comments.

Conflict of interest

The authors affirm that there are no conflicts of interest with regard to this research.

Author details

Miguel de Simón-Martín*, Ana-María Diez-Suárez, Laura-Álvarez de Prado, Alberto González-Martínez, Álvaro de la Puente-Gil and Jorge Blanes-Peiró

*Address all correspondence to: miguel.simon@unileon.es

Mines Engineering School, University of León, León, Spain

References

[1] Woyte A, Goy S. 11-large grid-connected photovoltaic power plants: Best practices for the design and operation of large photovoltaic power plants. In: Pearsall N, editor. The Performance of Photovoltaic (PV) Systems. Duxford, United Kingdom: Woodhead Publishing; 2017. pp. 321-337

[2] Ventura C, Tina GM. Utility scale photovoltaic plant indices and models for on-line monitoring and fault detection purposes. Electric Power Systems Research. 2016;**136**:43-56

[3] Bizzarri F, Brambilla A, Caretta L, Guardiani C. Monitoring performance and efficiency of photovoltaic parks. Renewable Energy. 2015;**78**:314-321

[4] Shariff F, Rahim NA, Hew WP. Zigbee-based data acquisition system for online monitoring of grid-connected photovoltaic system. Expert Systems with Applications. 2015; **42**:1730-1742

[5] Köntges M, Kurtz S, Packard C, Jahn U, Berger KA, Kato K, Friesen T, Liu H, Van Iseghem M. IEA-PVPS T13-01 2014 Review of Failures of Photovoltaic Modules Final [accessed: Mar 17, 2017]

[6] Jansen KW, Delahoy AE. A laboratory technique for the evaluation of electrochemical transparent conductive oxide delamination from glass substrates. Thin Solid Films. 2003;**423**:153-160

[7] Veldman D, Bennett IJ, Brockholz B, de Jong PC. Non-destructive testing of crystalline silicon photovoltaic back-contact modules. In: 2011 37th IEEE Photovoltaic Specialists Conference. 2011. pp. 003237-003240

[8] Knausz M, Oreski G, Eder GC, Voronko Y, Duscher B, Koch T, Pinter G, Berger KA. Degradation of photovoltaic backsheets: Comparison of the aging induced changes on module and component level. Journal of Applied Polymer Science. 2015;**132**:42093

[9] Trout TJ, Hu H, Wang CF, Garreau-Iles L, Heta Y, Stika KM, Yu B-L, Hamzavy B, Bradley A, MacMaster S, Felder T, Kopchick J, Gambogi W. Backsheet designs critical to PV module performance, safety and durability. In: 31st Eur. Photovolt. Sol. Energy Conf. Exhib. 2015. pp. 1930-1934

[10] Jordan DC, Kurtz SR. Photovoltaic degradation rates—An analytical review. Progress in Photovoltaics: Research and Applications. 2013;**21**:12-29

[11] Oliveira MCCD, Diniz C, Viana MM, Lins VDFC. The causes and effects of degradation of encapsulant ethylene vinyl acetate copolymer (EVA) in crystalline silicon photovoltaic modules: A review. Renewable and Sustainable Energy Reviews. 2018;**81**:2299-2317

[12] Peike C, Hülsmann P, Blüml M, Schmid P, Weiß K-A, Köhl M. Impact of permeation properties and Backsheet-Encapsulant interactions on the reliability of PV modules. ISRN Renewable Energy. 2012;**2012**:5 p

[13] Czanderna AW, Pern FJ. Encapsulation of PV modules using ethylene vinyl acetate copolymer as a pottant: A critical review. Solar Energy Materials & Solar Cells. 1996;**43**:101-181

[14] Montserrat DM, Saldaña-Mayor D, Dieste-Velasco MI, González-Peña D, Alonso-Tristán C. Degradation in silicon PV modules: Fault distribution analysis in grid connected facilities over long period of operation. In: Amsterdam, Niederlande, 2014

[15] Kajari-Schröder S, Kunze I, Eitner U, Köntges M. Spatial and orientational distribution of cracks in crystalline photovoltaic modules generated by mechanical load tests. Solar Energy Materials & Solar Cells. 2011;**95**:3054-3059

[16] Sander M, Dietrich S, Pander M, Schweizer S, Ebert M, Bagdahn J. Investigations on crack development and crack growth in embedded solar cells. 2011;**8112**:811209-811209-10

[17] Köntges M, Kunze I, Kajari-Schrder S, Breitenmoser X, Bjørneklett B. The risk of power loss in crystalline silicon based photovoltaic modules due to micro-cracks. Solar Energy Materials & Solar Cells. 2011;**95**:1131-1137

[18] Struwe R, Wang E, Chi S, Huang SY, Chien YC, Shiu S-M, Chou WY, Chou YH. Chemical analysis and proposed generating mechanism for snail tracks contamination of EVA encapsulated modules. In: 27th Eur. Photovolt. Sol. Energy Conf. Exhib. 2012. pp. 3132-3136

[19] Dolara A, Leva S, Manzolini G, Ogliari E. Investigation on performance decay on photovoltaic modules: Snail trails and cell microcracks. IEEE Journal of Photovoltaics. 2014;**4**:1204-1211

[20] Martinez Moreno F. Caracterización y modelado de grandes centrales fotovoltaicas. Telecomunicacion. 2012

[21] Tang R-L, Wu Z, Fang Y-J. Maximum power point tracking of large-scale photovoltaic array. Solar Energy. 2016;**134**:503-514

[22] Pingel S, Frank O, Winkler M, Daryan S, Geipel T, Hoehne H, Berghold J. Potential induced degradation of solar cells and panels. In: 2010 35th IEEE Photovoltaic Specialists Conference (PVSC); 2010; pp. 002817-002822

[23] Luo W, Khoo YS, Hacke P, Naumann V, Lausch D, Harvey SP, Singh JP, Chai J, Wang Y, Aberle AG, Ramakrishna S. Potential-induced degradation in photovoltaic modules: A critical review. Energy & Environmental Science. 2017;**10**:43-68

[24] Köntges M. Reviewing the practicality and utility of electroluminescence and thermography images; Photovoltaic Power Systems Programme. Hamelin: Institute for Solar Energy Research

[25] Green MA, Hasyim ES, Wenham SR, Willison MR. Silicon solar cells with integral bypass diodes. 1984. pp. 513-517

[26] Daliento S, Di N, Guerriero P, d'Alessandro V. A modified bypass circuit for improved hot spot reliability of solar panels subject to partial shading. Solar Energy. 2016;**134**:211-218

[27] de Simón-Martín M, Diez-Suárez AM, Álvarez de Prado L, González-Martínez A, de la Puente Gil Á, Blanes-Peiró J. Development of a GIS tool for high precision PV degradation monitoring and supervision: Feasibility analysis in large and small PV plants. Sustainability. 2017;**9**:965

[28] Moldes Teo FJ. Tecnología de los Sistemas de Información Geográfica. Madrid: Rama; 1995

[29] Shiota A, Fuchino G, Koyamatsu Y, Kakumoto Y, Tanoe K, Qudaih Y, Mitani Y. Guide construction of an efficient inspection, maintenance and asset management of photovoltaic power generation system using GIS. Energy Procedia. 2016;**100**:69-77

[30] FLIR Thermal Imaging Cameras: A Fast and Reliable Tool for Testing Solar Panels. 2015

[31] FLIR Thermal imaging guidebook for building and renewable energy applications. Infrared Training Center (ITC). 2011

Chapter 8

Multicell Design for Concentrated Photovoltaic (CPV) Module

Muhammad Burhan,
Muhammad Wakil Shahzad and Kim Choon Ng

Additional information is available at the end of the chapter

http://dx.doi.org/10.5772/intechopen.78000

Abstract

Despite its highest efficiency, concentrated photovoltaic (CPV) technology is still finding its way into the current photovoltaic market which is saturated with conventional flat-plate photovoltaic systems. CPV systems have a great performance potential as they utilize third-generation multi-junction solar cells. In the CPV system, the main aspect is its concentrating assembly design which affects not only its overall performance but also its operation and fabrication. Conventional CPV design targets to use individual solar concentrator for each solar cell. The main motivation of this chapter is to propose a novel concentrating assembly design for CPV that is able to handle multiple solar cells, without affecting their size, using single solar concentrator. Such proposed design, named as multicell concentrating assembly (MCA), will not only reduce the assembly efforts during CPV module fabrication, but it will also lower the overall system cost with simplified design. In this chapter, a detailed design methodology of multicell concentrating assembly (MCA) for CPV module is presented and developed with complete verification through ray tracing simulation and field experimentation.

Keywords: novel concentrator, homogenizer, CPV, concentrator photovoltaic, multi-junction solar cell

1. Introduction

Due to dependency of global energy need on fossil fuels, the global warming situation is hitting to an alarming level with record amount of greenhouse gas emissions. Under such circumstances, renewable energy resources are seen to be able to provide sustainable energy source to

meet global energy needs [1–4]. However, solar energy, being the energy source with the highest energy potential [5–7], can provide a sustainable source of future primary energy supply if captured with high efficiency and simple configuration. Photovoltaic system provides the most simple configuration to convert solar energy into high-grade energy form, i.e., electricity. However, in the current photovoltaic market with 99% share of single-junction solar cells, the multi-junction solar cells (MJCs) have yet to exploit their potential of the highest solar energy conversion efficiency. This is due to the fact that the multi-junction solar cell (MJC) can respond to a full spectrum of solar radiation, with less loss and as a result higher efficiency [8–12]. On the other hand, due to their high material cost, MJCs are not available in the form of flat-plate panels like conventional single-junction solar cells. But rather, they are utilized in the form of concentrated photovoltaic (CPV) system where low-cost solar concentrators concentrate solar radiations onto the small area of solar cell material, thereby reducing the use of expensive solar cell material by 500 or 1000 times [13–17]. This is possible because MJC can withstand high concentrations. However, all of the commercial CPV modules, available hitherto, can only accommodate single solar cell per concentrator [18, 19]. Such conventional system requires increased assembly efforts. Therefore, by keeping the cell size same, this chapter discusses a novel CPV module design which can accommodate multiple MJCs with single solar concentrator.

2. Multicell concentrating assembly (MCA)

The simple concept of proposed multicell concentrating assembly (MCA) is shown in **Figure 1**, for novel CPV module design. The concentrating assembly is based upon a multi-leg homogenizer concept which allows the rays, collected from specially arranged pair of solar concentrators, to be uniformly distributed and transferred to four MJCs. In a simple form, received parallel solar radiations are transformed into a concentrated collimated beam, with the help of a pair of parabolic concentrators which are arranged in Cassegrain form. The concentrated collimated beam strikes at the inlet aperture of multi-leg homogenizer where it is uniformly split and distributed among MJCs, placed at the four outlet apertures of the homogenizer. In conventional CPV module design, the homogenizer is placed to accommodate the tracking errors

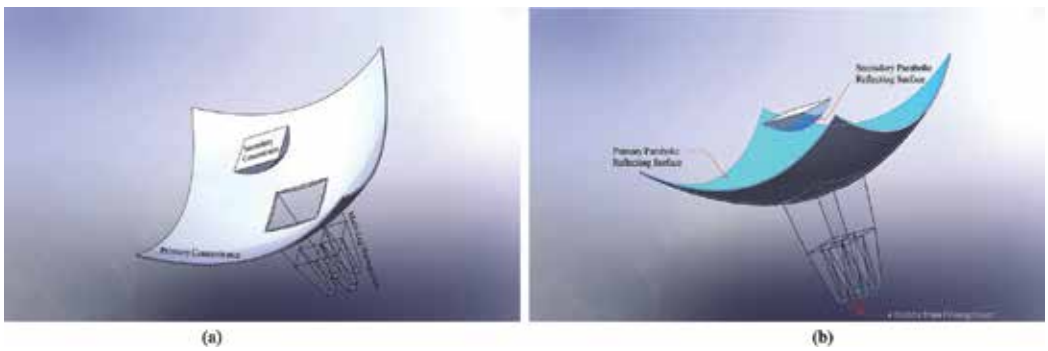

Figure 1. Schematic of novel multicell concentrating assembly (MCA) for CPV module.

associated with the two axis solar tracking, during CPV operation. However, in the proposed novel multicell concentrating assembly (MCA) design, the homogenizer not only serves as part of conventional homogenizer, but it also helps to split the collimated beam received from a pair of parabolic concentrators. Such ray splitting is achieved because of the fact that the collimated beam, at the inlet aperture of homogenizer, makes an area concentration unlike conventional concentrating assembly design in which point concentration is achieved. By using the concept of concentrator photovoltaics (CPV), the expensive semiconductor multi-junction solar cell material was replaced with cheap solar concentrators. However, with the proposed multicell concentrating assembly design, the cost and assembly efforts of CPV modules will be reduced as a less number of solar concentrators will be needed for same capacity of the system.

3. Theoretical design of MCA

The theoretical design of proposed multicell concentrating assembly (MCA) is explained in **Figure 2**. It can be seen that the design is based upon the Cassegrain arrangement of two parabolic concentrators, with the intention of achieving the area concentration. Such concentrating assembly acts as a collimating reflector where the parallel solar radiations are converted into concentrated collimated beam. Both parabolic reflectors are arranged such that their focal points coincide with each other. In addition, one of the reflectors uses its inner surface for reflection, while the other uses its outer surface. The primary reflector converges the incoming parallel rays at its focal point. However, these converging rays interact with the outer surface of secondary parabolic reflector which is placed in their way to the focal point. The secondary reflector introduces the cancelation effect which converges rays and diverges them as parallel rays. However, due to smaller contact surface of secondary reflector, the diverged collimated rays become concentrated before they hit the inlet aperture of homogenizer. In order to design multicell concentrating assembly (MCA), the edge ray is traced such that it hits point 'b' of secondary concentrator after being reflected by point 'a' of primary concentrator. As the foci of both reflectors are coinciding, therefore, the edge ray become parallel again after being reflected by the outer surface of secondary reflector and enter the homogenizer through its inlet aperture. This edge ray, after entering into the homogenizer, hits point 'c', which is located at its lower tapered portion. This lower tapered portion of multi-leg homogenizer is designed such that the edge ray, after being reflected by total internal reflection from point 'c', hits point 'e' of outlet aperture of homogenizer and falls on the MJC, placed there. The distribution of such parallel ray distribution is easily explained in simple schematic shown in **Figure 2(b)**. The back surface of MJC is attached to the heat spreader and heat sink assembly, to effectively dissipate the heat during CPV operation. It can be seen that the rays, after being reflected by secondary reflector, become concentrated over an area and size of such area concentration depends upon the size of secondary reflector.

There are three phases in which the design of proposed multicell concentrating assembly (MCA) is divided. The first phase is related to the calculations needed for the sizing of primary reflector. The main factor determining the size of primary reflector is the concentration requirement, depending upon the MJC specifications. The second phase is related to the form

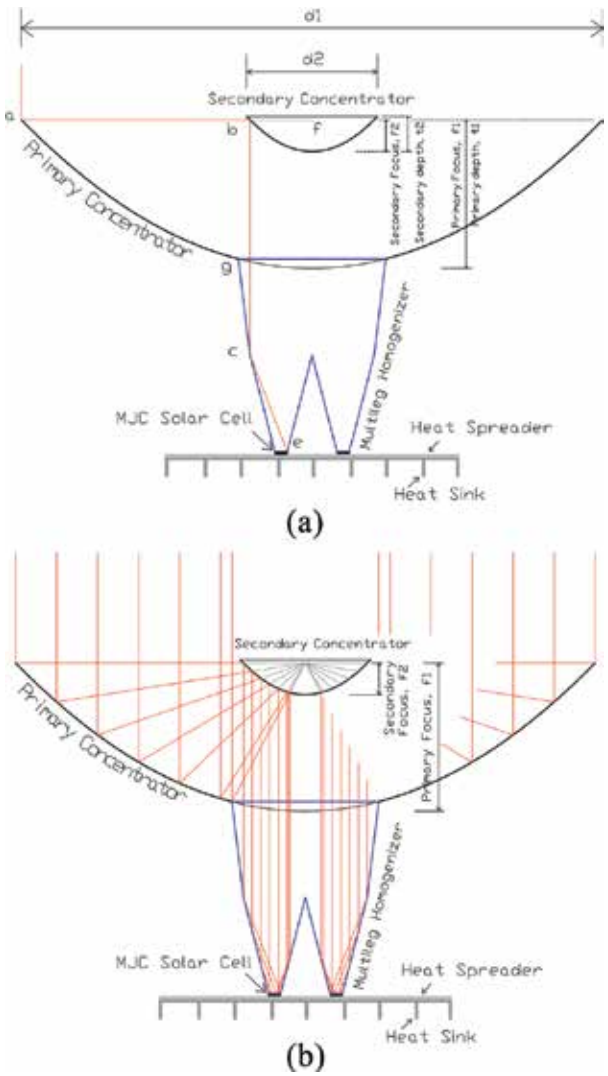

Figure 2. (a) Design and (b) ray distribution of proposed multicell concentrating assembly (MCA).

and the design of multi-leg homogenizer, which is also depending upon the specification of MJC as the outlet apertures of homogenizer must have dimensions same as MJC size. After finalizing the design of multi-leg homogenizer, the third phase is related to the secondary reflector sizing as it depends upon the size of inlet aperture of homogenizer. The detailed procedure associated with the overall design of multicell concentrating assembly (MCA) will be explained in this section.

The design parameters associated with the sizing of primary parabolic reflector are given in **Table 1**. It can be seen that the concentration ratio selected for the targeted prototype of MCA is 165, for the MJC of size (5.5 × 5.5 mm). Concentration ratio of 165 is only chosen to limit the overall size of the primary reflector due to budget limitations as larger reflector will cost

higher at the prototyping stage. Therefore, a reasonable concentration ratio of 165 is chosen to prove the concept. This concentration is only chosen for prototype design purpose, while the MCA can be designed for any concentration ratio of ×500 or ×1000, depending upon the specification of MJC. In order for the rays to enter homogenizer, a center hole of square size (50 × 50 mm) is cut in the primary parabolic reflector, as demonstrated in **Figure 3**.

From **Figure 3**, it can be seen that the effective area of MCA, to capture the solar radiations, is the one highlighted in white, which is calculated by Eqs. (1) and (2).

$$\text{Effective area of concentrating assembly } A_{CA} = CR_g \times A_M \times 4 \tag{1}$$

$$\text{Area of primary concentrator} = d_1^2 = A_{CA} + A_H \tag{2}$$

Parameter 'd' defines the dimension of square parabolic reflector. It must be noted that the square shape of primary reflector is firstly considered because of uniform distribution of

Sr. no.	Parameter	Symbol	Units	Value
1	Geometric concentration ratio	CR_g	—	165
2	Area of MJC	A_M	m^2	0.00003025 (5.5 × 5.5 mm)
3	Area of center square hole	A_H	m^2	0.0025 (50 × 50 mm)

Table 1. Primary reflector design parameters.

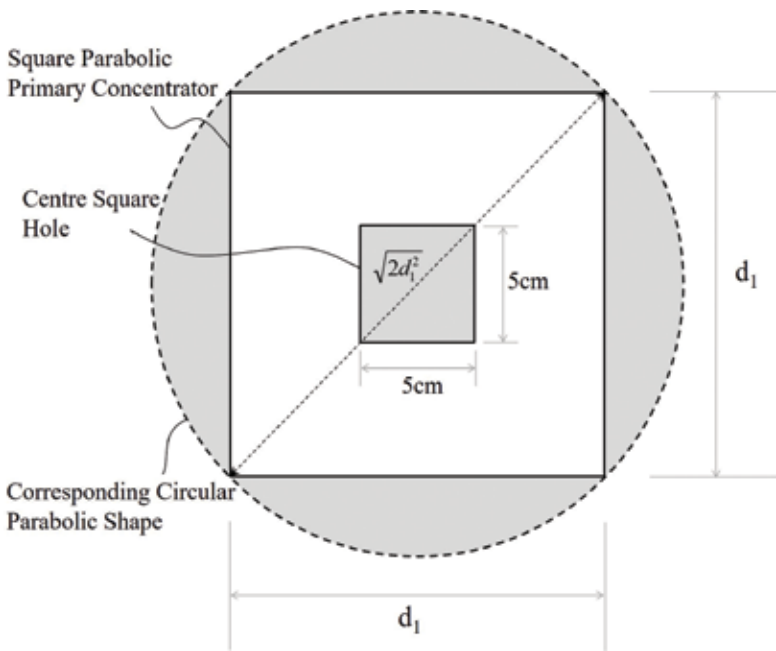

Figure 3. Simple schematic for primary reflector size calculations.

rays over cell area as MJC is of square shape. Secondly, the square shape primary reflector provides maximum packing density and perfect arrangement within CPV module, without leaving any empty pocket.

In Eq. (1), factor '4' is used because of four outlet apertures of homogenizer, with the size same as MJC. By using the concentration ratio of 164, the size of square primary parabolic reflector is calculated as 15 × 15 cm. Before proceeding to the design of multi-leg homogenizer, it is important to trace the position of edge ray. It must be noted that, as per **Figure 3**, the primary parabolic reflector is actually a square-cut piece of circular shape, and the diagonal of square reflector gives the diameter of the circular shape, as given by Eq. (3):

$$D_1 = \sqrt{d_1^2 + d_1^2} = \sqrt{2d_1^2} \tag{3}$$

Besides the size of primary reflector, it is also very important to keep the overall height of CPV modules minimum as it can make shipping and handling easy and cheap. It can also lessen the mechanical problems faced during CPV operation. Therefore, in order to keep the overall height of MCA minimum, the focal point of primary parabolic reflector is kept same as its depth 't'. By using the parabolic curve equation, the focal point 'f_1' of primary parabolic concentrator can be calculated by Eq. (4):

$$f_1 = \frac{(D_1/2)^2}{4t_1} = \frac{D_1^2}{16f_1} \quad (f_1 = t_1) f_1^2 = \frac{D_1^2}{16} \tag{4}$$

Diameter 'D_1' of corresponding circular shape of primary reflector can be calculated as 21.2132 cm, by using the 15 cm size in Eq. (3). As a result, Eq. (4) gives the focal point value of primary parabolic concentrator as 5.3033 cm. The simple parabolic Eq. (5) can now be used to calculate the coordinates of the parabolic surface of primary reflector:

$$x^2 = 4fy \tag{5}$$

The multi-leg homogenizer is consisting of four similar sections, joined together as a single unit. Therefore, for easy understanding, the design of single section will be explained in detail first, which will be combined together to form the proposed multi-leg homogenizer. The simple 2D schematic of multi-leg homogenizer is shown in **Figure 4** where only its two sections are shown. Each single section of multi-leg homogenizer has two tapered section, i.e., above and below line 'eb'. The tapered section below line 'eb' is designed such that it uniformly distributes solar radiations over the cell area in case of parallel rays. However, the tapered section above line 'eb' is designed to accommodate the tracking error by guiding the non-parallel incoming solar radiations towards the outlet aperture of homogenizer. In order to discuss the homogenizer design, it is better to discuss the case for parallel rays first, for easy understanding.

Edge ray 'j' which is parallel to the primary reflector axis, as shown in **Figure 4**, is the same edge ray explained in **Figure 2(a)** that is coming from secondary reflector. However, after entering into the homogenizer, it hits point 'b' located at the start of lowered tapered portion

http://dx.doi.org/10.5772/intechopen.78000

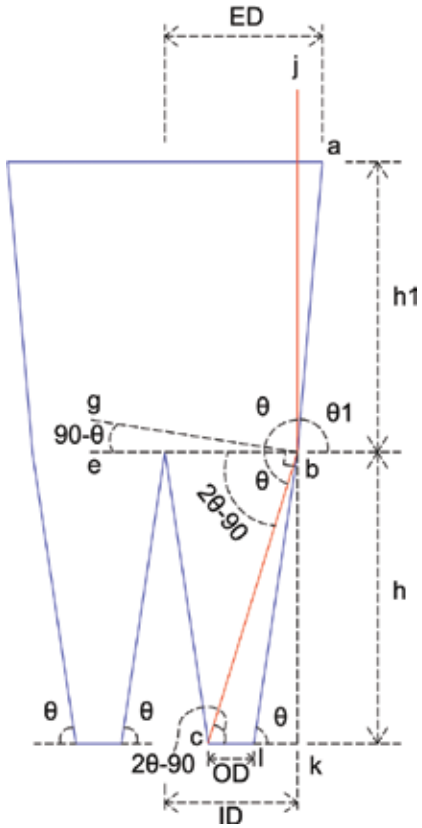

Figure 4. Multi-leg homogenizer design and schematic.

of homogenizer. Such a ray must exit through edge point 'c' of the outlet aperture of the homogenizer, to ensure uniform distribution of solar radiations over the cell area. Therefore, the dimensional parameters of lower tapered portion of homogenizer, i.e., height 'h' and slope angle 'θ' of side line 'bl', are of prime importance here. As explained, the value of these two parameters must be tuned such that the parallel edge rays, after passing through the homogenizer, must exit through end point 'c' of outlet aperture. **Figure 4** shows the angular position of such tapered portions as defined by the trigonometric laws. The angle between line 'bl' and the hypothetical line 'bg' is taken as 'θ'. As these lines are perpendicular to each other, therefore, the edge ray also makes same angle 'θ' with the hypothetical line 'bg'. By considering the triangular section Δckb, the height 'h' of lower tapered portion of homogenizer is given by Eq. (6):

$$h = \left[OD + \left(\frac{ID - OD}{2}\right)\right].\tan(2\theta - 90) \tag{6}$$

It can be seen that there are two unknowns in Eq. (6), i.e., 'θ' and 'h'. Therefore, such equation cannot be solved for the mentioned unknowns. For the solution of such equation, the triangle Δblk can be considered to get Eq. (7):

$$h = \left(\frac{ID - OD}{2}\right).\tan\theta \tag{7}$$

If Eqs. (6) and (7) are compared, then we can find the expression for the lower slope angle 'θ' as given by Eq. (8):

$$\left[OD + \left(\frac{ID - OD}{2}\right)\right].\tan(2\theta - 90) = \left(\frac{ID - OD}{2}\right).\tan\theta \tag{8}$$

Parameter 'OD' represents the dimension for the outlet aperture of homogenizer, which is same as the size of MJC, i.e., 5.5 mm. On the other hand, a suitable value of '16' is also considered for parameter 'ID' so that ray can easily be propagated to the outlet aperture. If the value of 'ID' is small, then the height 'h' will also be small, same for 'OD'. Otherwise, the ray will have multiple total internal reflections (TIR) inside the homogenizer if the value of 'h' is higher for smaller 'ID'. Or, there may be a chance that the ray can propagate back if the value of 'h' is very big. However, the large value of 'ID' also requires a larger value of 'h', same for 'OD'. For the given value of 'ID' and 'OD', the value of 'θ' and 'h' can be calculated as 81.33° and 34.43 mm, respectively.

After finalizing the design of lower tapered portion of the homogenizer, now the upper tapered portion of homogenizer is considered, which is needed to be designed to accommodate the rays which are not parallel to the axis of concentrating assembly. From the design point of view, a tracking error of 1° is selected which can be handled by the homogenizer. This means that the homogenizer design will be able to handle the deviated ray for maximum angle of 1°. By using the graphical method and trigonometric laws, it has been shown in **Figure 5** that if there

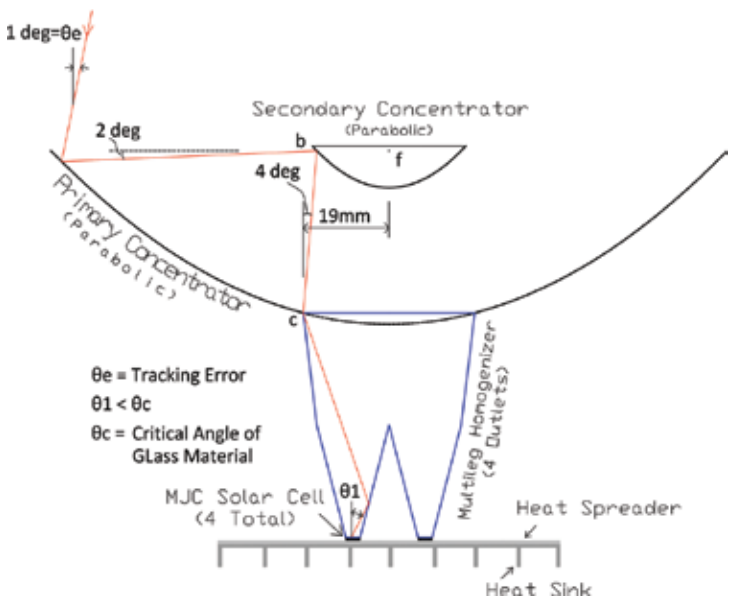

Figure 5. Acceptance angle calculation for multicell concentrating assembly.

is 1° deviation in the incident ray from the primary reflector axis, such deviation increases to 2° after being reflected by the primary reflector. Similarly, after being reflected by secondary reflector, this deviation increases to 4°. Therefore, to handle such 1° deviation in the incident ray, by the homogenizer, its half width is found to be 19 mm, by the graphical method.

In the third phase of MCA design, the size of secondary reflector is calculated. As shown in **Figure 2(A)**, the edge ray, after being reflected by point 'b' of secondary reflector, hits point 'c' of the homogenizer which is the edge point of lower tapered portion of 'ID'. Therefore, for the calculation of the focal point of secondary reflector, the value of D_1 = ID should be used in Eq. (4). The main reason for this consideration is that the focal point of both reflectors is coinciding as the parallel ray pattern is needed to be achieved after secondary reflection, which must hit the lower tapered portion of the homogenizer with size 'ID = 16 mm'. However, the radius of secondary reflector will be according to 'ED' which is found to be '19 mm'. The coordinates for parabolic surface of secondary reflector can be found using Eq. (5), for the value of 'x' being varied from 0 to 19. The size of secondary reflector is same as that of the inlet aperture of the homogenizer, to account for the tracking error.

4. Development of MCA-based CPV prototype

To verify and analyze the field performance of proposed and designed MCA, a prototype of CPV is fabricated as per designed concentration ratio of ×165. The prototype of fabricated MCA is shown in **Figure 6** and the MCA-based novel CPV unit is shown in **Figure 7**. The primary and secondary reflectors are machined from aluminum blocks. However, to improve the surface quality and reflection characteristics, the reflecting surface of both reflectors was coated with thin optical graded reflecting aluminum layer, using sputter-coating method. The multi-leg homogenizer was fabricated in the form of four symmetrical pieces which were joined together to form a single unit. Each homogenizer piece is similar to the half of schematic shown in **Figure 4**. The individual pieces of homogenizer were machined using N-BK7 glass material. To form a single homogenizer unit, all four pieces were joined together using optical graded UV glue. It must be noted that the machining method of fabrication is an expensive fabrication technique, and that is why smaller concentration ratio was chosen at the start to keep the overall cost minimum. However, for mass production of reflectors and homogenizers, injection molding techniques for plastic and glass materials are used.

Four MJCs were attached at the four outlet apertures of the homogenizer. However, the back side of MJCs was attached to the heat spreader and heat sink to dissipate the heat during CPV operation and to keep the cell temperature within optimum limit.

In order to test the performance of developed novel MCA-based CPV module, a two-axis solar tracking unit was used with tracking accuracy of 0.1° [20, 21]. The developed CPV module was mounted onto the top frame of solar tracker. The tracking system is based upon the hybrid tracking algorithm which defines the solar position through both active and passive techniques. After calculating the position of sun, based upon the solar geometry model, the actual position of the sun is verified by taking the real-time feedback

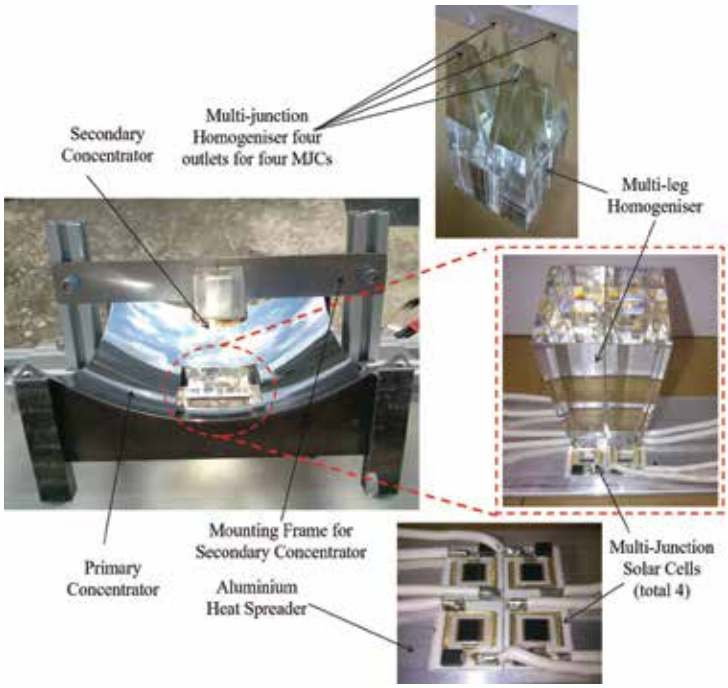

Figure 6. Developed prototype of multicell concentrating assembly (MCA)-based CPV module.

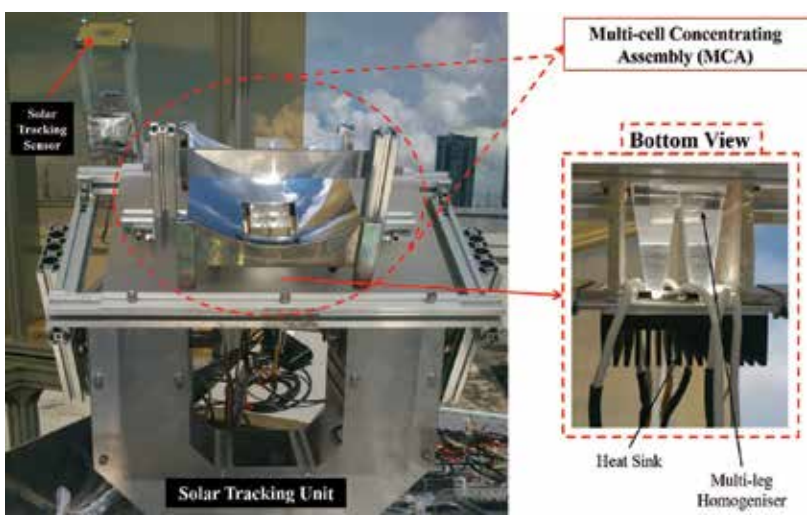

Figure 7. Experimental prototype of MCA-based novel CPV unit.

from solar tracking sensor. Such real-time optical feedback avoids any chance of tracking error which may arise due to passive tracking method and possible backlash in the driving assembly.

5. Results and discussion

In order to analyze the optical performance of proposed multicell concentrating assembly (MCA), the ray tracing simulation was conducted using TracePro software. The concentrating assembly was analyzed in terms of division of rays among four outlet apertures, uniformity of rays at the outlet aperture and investigation of deflected path of incident rays. The simulation model for proposed MCA, according to the discussed design, is shown in **Figure 8**. To conduct ray tracing simulation, a square grid of parallel rays was selected as the primary reflector is also of square shape. As the received solar radiation is not exactly parallel in nature, that is why the simulated MCA model was not only investigated for parallel ray grid but also for the grid with angle same as the solar subtended angle. The ray tracing simulation results of proposed MCA design with parallel ray grid are shown in **Figure 9**. It can be seen that a perfect division of rays among four outlet apertures of homogenizer is experienced. In addition, the rays are also uniformly distributed over the whole surface area of outlet aperture. Moreover, a concentrated collimated beam is also achieved after reflection of parallel incident rays from secondary reflector. As per discussed design, this concentrated collimated beam is being divided among four sections of homogenizer and also hitting the lower tapered portion of the homogenizer.

In order to simulate the optical performance of proposed MCA in real field environment, the simulation results for grid of rays with solar subtended angle are shown in **Figure 10**. These rays are not exactly parallel to the axis of primary reflector but have a small deviation which is same as the actual solar radiations, received during real field operation. It can be seen that there is still a perfect division of received radiations among four sections of the homogenizer and uniform distribution of these radiations over the outlet apertures of homogenizer. However, one of the differences which can be seen here is that the rays are also hitting the upper tapered portion of the homogenizer, without any induced ray deviation. The reason

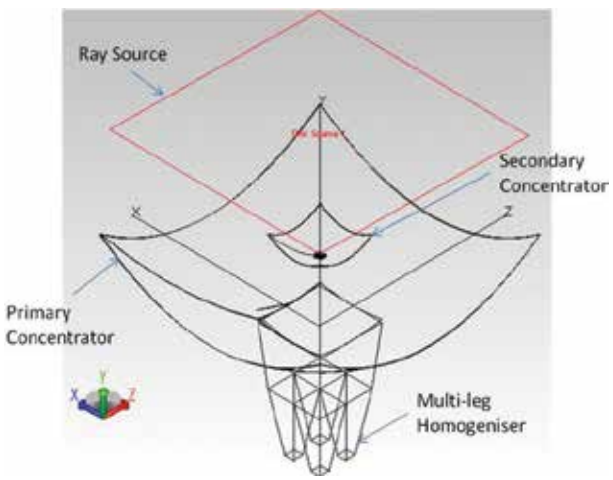

Figure 8. TracePro model of multicell concentrating assembly (MCA) for ray tracing simulation.

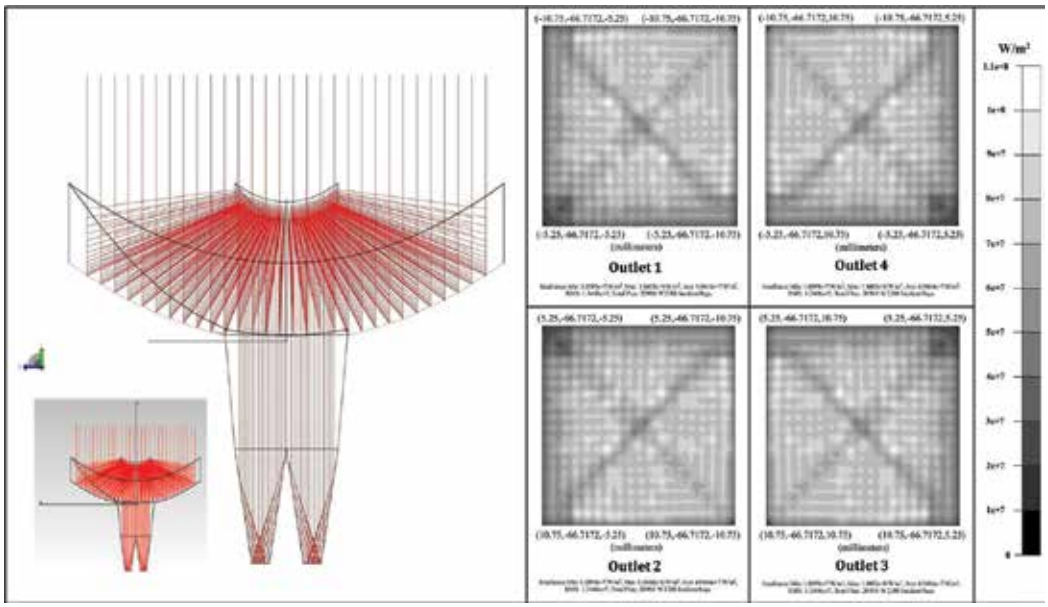

Figure 9. Ray tracing simulation of multicell concentrating assembly for parallel rays.

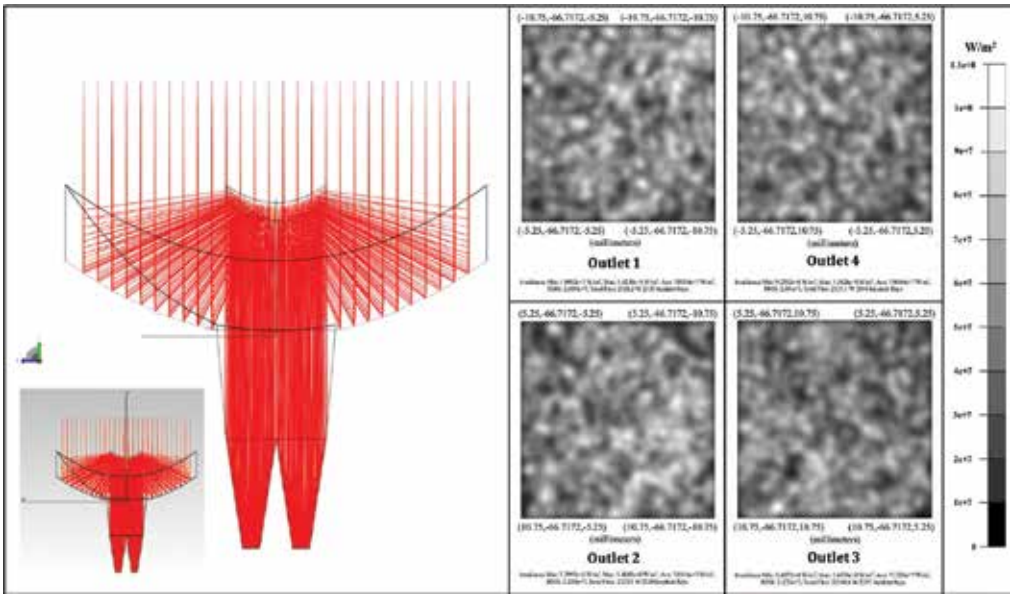

Figure 10. Ray tracing simulation of multicell concentrating assembly for solar subtended angle.

is that the incoming rays are already not parallel to the axis of primary reflector, and that is why they are reflected by the upper tapered portion which is designed to accommodate the tracking error or rays which are not parallel to the primary reflector axis.

http://dx.doi.org/10.5772/intechopen.78000

After verifying the design of developed multicell concentrating assembly (MCA) through ray tracing simulation, it is also important to verify its performance under real conditions during field testing. The developed prototype of CPV system, with MCA-based design, was tested under field condition, and the output from each of the MJC, at four outlet apertures of homogenizer, was logged in real time using data logging unit. The power and voltage output of each of four MJCs is shown in **Figures 11** and **12**. From both figures, it is clear that there is equal distribution of solar radiations among four MJCs, during whole-day operation as their power and voltage plot look similar. It must be noted that the solar tracking unit was operated with tracking accuracy of 0.3°, instead of 0.1°. The equal output of all four MJCs, with such tracking accuracy, verifies the proposed design of multicell concentrating assembly (MCA) and its compatibility in fulfilling the objective.

Another important test to investigate the response of concentrating assembly against different angular deviations of incident rays is expressed in the form of normalized power curve. So far, the performance of MCA, either simulated or experimental, is tested for parallel rays or rays with smaller deviations. In order to test the maximum response limit of concentrating assembly over different deviation angles, the normalized power output of the system is plotted against the angular deviation. Such normalized power curve also helps to predict the acceptance angle of concentrating assembly for efficient operation. The normalized power curve for developed multicell concentrating assembly (MCA)-based CPV is shown in **Figure 13**. The red line indicates the normalized power curve obtained from ray tracing simulation against different deviation angles of parallel rays. The simulated normalized power is obtained by taking the ratio of the total number of rays at the outlet apertures to the total incident rays. However, the blue line indicates the true normalized power output curve obtained through

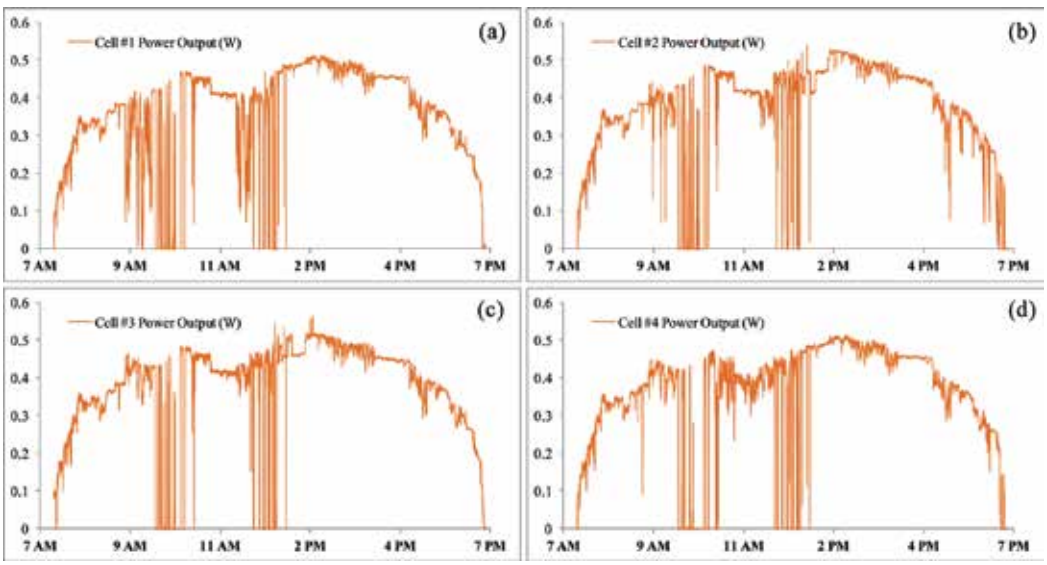

Figure 11. Power output for individual cell of MCA-based CPV system.

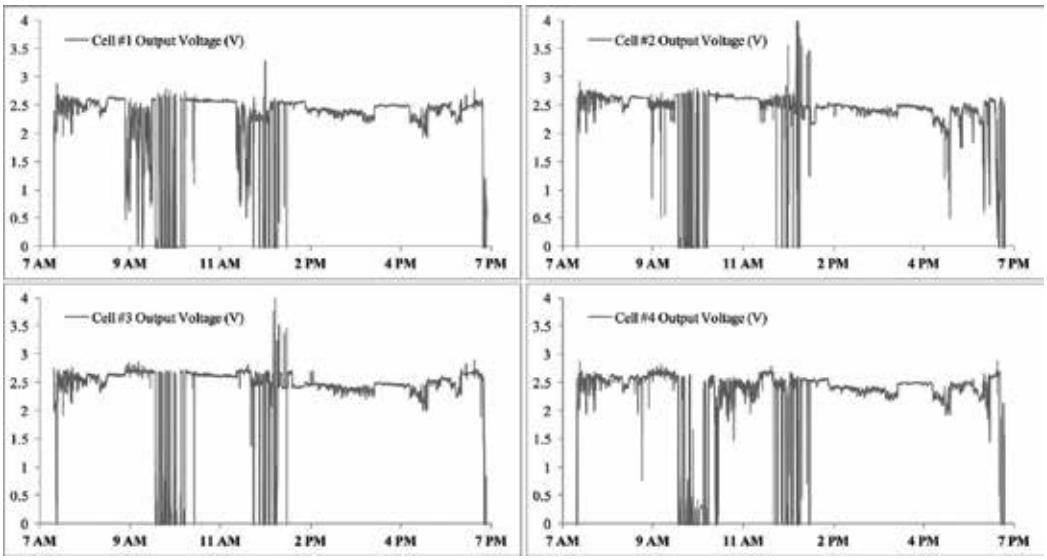

Figure 12. Voltage output for individual cell of MCA-based CPV system.

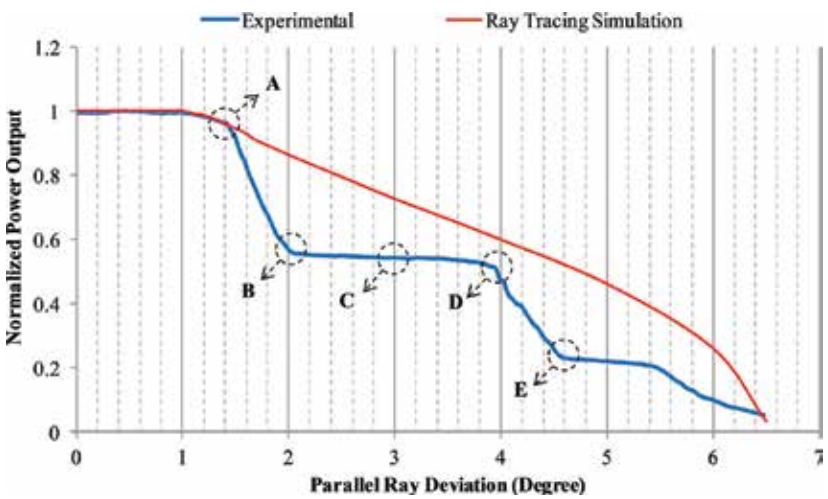

Figure 13. Normalized power curves for multicell concentrating assembly-based CPV system.

experimentation. In order to obtain such plot, the tracker movement was stopped, while the CPV module was exactly facing the sun, during noontime. The angular deviation was calculated by taking the difference in the initial and current position of sun. The power output of all four MJCs, connected in series, was logged under real time for constant output load. It is clear from **Figure 13** that the simulated normalized power output is almost 100% for angular deviations up to 1°. It is also true for experimental results, which verifies the proposed design of MCA. If there is further increase in the incident ray deviation, than 1°, the normalized power starts to drop.

It can be seen that there is a good agreement between simulated and experimental normalized power curves, until point 'A'. However, the experimental curve starts deviating from simulated curve after point 'A'. There is gradual decrease in the simulated power curve. However, a stepwise drop is observed for experimental curve. Such a different response of simulated

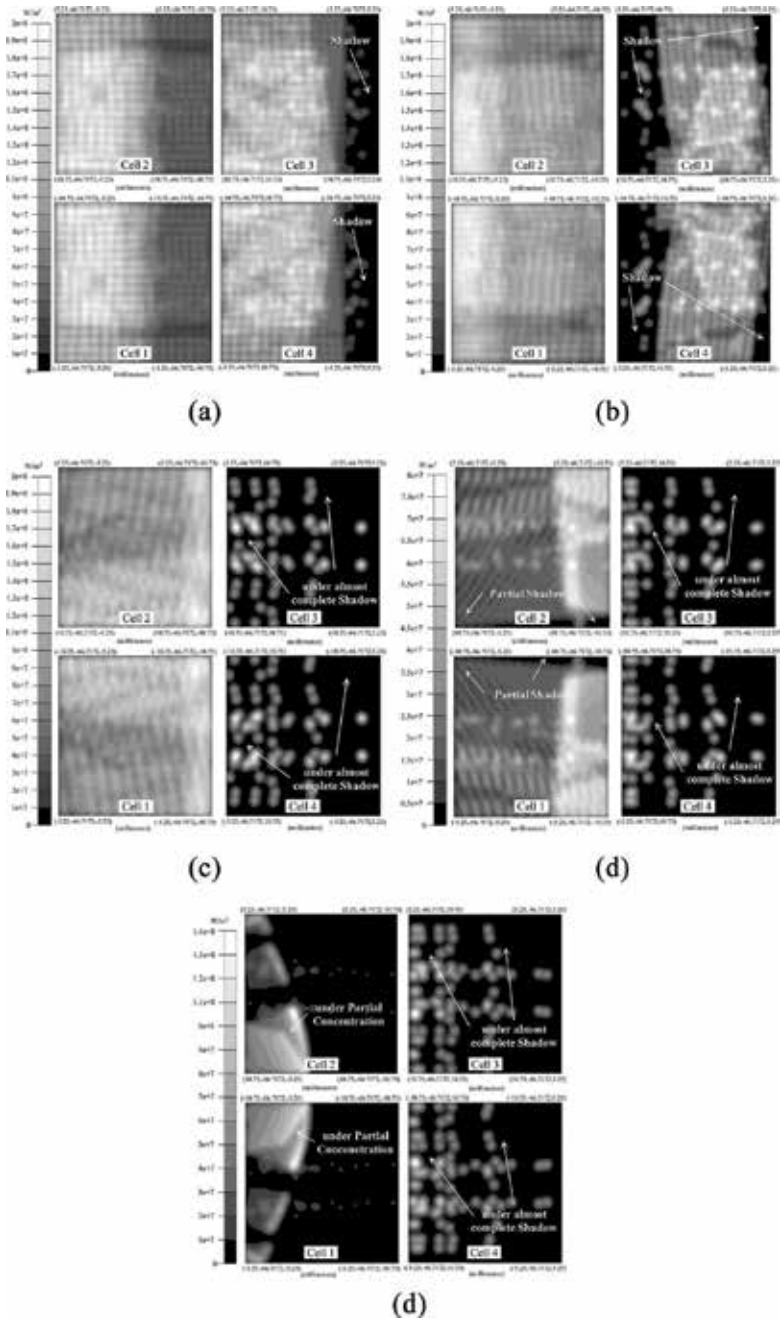

Figure 14. Simulated irradiance map at outlet apertures of multi-leg homogenizer for different angular deviations of parallel rays.

and experimental normalized power curves can be explained with the fact that the simulated power output is just based upon the number of radiation received at the outlet apertures of homogenizer. However, for experimental curve, the power output is the actual electrical power obtained from CPV module but at a constant load. As the load across CPV module is constant, therefore, excessive ray loss causes its maximum power point to shift, resulting in a decrease in its output and performance. That is why it also deviates from the simulated curve. To carefully understand the varying trend of simulated and experimental normalized power curves, the simulated irradiance map at all four outlet apertures of homogenizer is shown in **Figure 14**. The irradiance maps are plotted against different points mentioned on experimental normalized curve. It can be seen from **Figure 14(A)**, which shows the irradiance map at point 'A', that the solar cells 3 and 4 are coming under shadow. For simulated curve, this shadow is just a decrease in the number of rays coming out of the homogenizer. However, in actual system, the electrical output of the CPV system is greatly disturbed as all MJCs are connected in series. The maximum power point for cells under shadow changes, and they also pulls down the performance of other MJCs due to their series connection. Therefore, overall electrical output of complete CPV module decreases. At points 'B', 'C' and 'D', the normalized electrical power output of CPV system is almost same as 50%. This is because of the fact that at this point, only two cells are operating, while the other two cells are under complete shadow, as shown in **Figure 14(B)–(D)**. However, for simulated power curve, there is still a gradual decrease for these points which implies that the net flux output is not reduced to 50% for all these three points, i.e., 'B', 'C' and 'D'. The main reason for half of electrical output is because of the shift in the maximum power point for the entire CPV system, which is effected by the two cells under shadow.

After increasing deviation angle beyond point 'D', the experimental curve again starts to drop till point 'E'. This is because of the fact that now the other two cells are also coming under shadow, as can be seen in **Figure 14(D)**. At point 'E', the remaining two cells are under only partial concentration. That is why the power output reduced to a low value. The power output remains stable for a while after point 'E' which is just because of partial concentration that moves around the cell area due to leftover and scattered radiations. With further increase in the deviation angle, the power output slowly dies to zero. The normalized power output curve shows that the develop CPV system, based upon the proposed MCA, has acceptance angle of 1° as designed. However, it has a capability of operation for deviation angle as high as 6.5°. However, the power output drops significantly, but the system can still respond to the received radiations.

6. Summary of the chapter

In the current photovoltaic market, with dominating share of single-junction solar cells, the highly efficient concentrated photovoltaic systems (CPV), utilizing third-generation multi-junction solar cells, have yet to exploit their market potential due to their design complexities. The conventional CPV module design utilizes individual concentrator for each MJC. This chapter has introduced a novel design of CPV concentrating assembly where single

concentrator can handle four MJCs, named as multicell concentrating assembly (MCA). Such proposed design will not only reduce the overall cost of the system, but it will also reduce the assembly and alignment efforts during CPV module fabrication.

In this chapter, a detailed design of such multicell concentrating assembly is discussed and explained. For prototype purpose, the detailed calculation of concentrating assembly size is presented for concentration ratio of ×165. Such proposed design is transformed into working prototype of CPV module for actual field testing. The design was targeted to handle angular deviations of 1° without any loss in performance.

A detailed performance investigation strategy was adopted to verify the proposed design with its prototype and its limitation during field operation. An optical simulation was conduction in TracePro to verify the optical performance of MCA. An equal division and uniform distribution of rays were observed at the outlet apertures of homogenizer. From the field testing, equal and uniform power output of each MJC verified the proposed design of multicell concentrating. However, to analyze the response of MCA against angular deviation of incident ray, normalized power output curve was presented against angular deviation, for both experimental and simulated performances. The system showed 100% power output for angular deviations up to 1°, as designed. However, the system showed maximum capability of handling 6.5° angular deviations. A great agreement was observed among simulated and experimental results.

Nomenclature

d_1	dimension of square primary reflector of multi-leg homogenizer concentrating assembly (mm)
t_1	depth of primary reflector of multi-leg homogenizer concentrating assembly (mm)
f_1	focal length of primary reflector of multi-leg homogenizer concentrating assembly (mm)
A_M	area of multi-junction solar cell (mm^2)
D_1	corresponding diameter of primary reflector of multi-leg homogenizer concentrating assembly (mm)
θ_e	tracking error (degree)
CR_g	geometric concentration ratio
d_2	dimension of square secondary reflector of multi-leg homogenizer concentrating assembly (mm)
t_2	depth of secondary reflector of multi-leg homogenizer concentrating assembly (mm)
f_2	focal length of secondary reflector of multi-leg homogenizer concentrating assembly (mm)
A_{CA}	area of concentrating assembly (mm^2)

A_H area of center hole in primary reflector of multi-leg homogenizer concentrating assembly (mm^2)

θ_c critical angle of glass material (degree)

MJC multi-junction solar cell

Author details

Muhammad Burhan*, Muhammad Wakil Shahzad and Kim Choon Ng

*Address all correspondence to: muhammad.burhan@kaust.edu.sa

Water Desalination and Reuse Centre, Biological and Environmental Science and Engineering Division, King Abdullah University of Science and Technology, Saudi Arabia

References

[1] Najibi F, Niknam T. Stochastic scheduling of renewable micro-grids considering photovoltaic source uncertainties. Energy Conversion and Management. 2015;**98**:484-499

[2] Burhan M, Shahzad MW, Ng KC. Development of performance model and optimization strategy for standalone operation of CPV-hydrogen system utilizing multi-junction solar cell. International Journal of Hydrogen Energy. 2017;**42**(43):26789-26803

[3] Burhan M, Chua KJE, Ng KC. Electrical rating of concentrated photovoltaic (CPV) systems: Long-term performance analysis and comparison to conventional PV systems. International Journal of Technology. 2016;**7**(2):189-196. DOI: 10.14716/ijtech.v7i2.2983

[4] Ng KC, Burhan M, Shahzad MW, Ismail AB. A universal isotherm model to capture adsorption uptake and energy distribution of porous heterogeneous surface. Scientific Reports. 2017;**7**(1):10634

[5] Burhan M, Chua KJE, Ng KC. Sunlight to hydrogen conversion: Design optimization and energy management of concentrated photovoltaic (CPV-hydrogen) system using micro genetic algorithm. Energy. 2016;**99**:115-128

[6] Chantana J, Ueno S, Ota Y, Nishioka K, Minemoto T. Uniqueness verification of direct solar spectral index for estimating outdoor performance of concentrator photovoltaic systems. Renewable Energy. 2015;**75**:762-766

[7] Burhan M, Oh SJ, Chua KJE, Ng KC. Double lens collimator solar feedback sensor and master slave configuration: Development of compact and low cost two axis solar tracking system for CPV applications. Solar Energy. 2016;**137**:352-363

[8] Burhan M, Oh SJ, Chua KJ, Ng KC. Solar to hydrogen: Compact and cost effective CPV field for rooftop operation and hydrogen production. Applied Energy. 2017;**194**:255-266

[9] Burhan M, Shahzad MW, Ng KC. Long-term performance potential of concentrated photovoltaic (CPV) systems. Energy Conversion and Management. 2017;**148**:90-99

[10] Shockley W, Queisser HJ. Detailed balance limit of efficiency of p-n junction solar cells. Journal of Applied Physics. 1961;**32**(3):510-519

[11] Burhan M, Shahzad MW, Choon NK. Hydrogen at the rooftop: Compact CPV-hydrogen system to convert sunlight to hydrogen. Applied Thermal Engineering. 2018;**132**:154-164

[12] Burhan M, Chua KJE, Ng KC. Long term hydrogen production potential of concentrated photovoltaic (CPV) system in tropical weather of Singapore. International Journal of Hydrogen Energy. 2016;**41**(38):16729-16742

[13] Baig H, Sellami N, Mallick TK. Trapping light escaping from the edges of the optical element in a concentrating photovoltaic system. Energy Conversion and Management. 2015;**90**:238-246

[14] Burhan M, Chua KJE, Ng KC. Simulation and development of a multi-leg homogeniser concentrating assembly for concentrated photovoltaic (CPV) system with electrical rating analysis. Energy Conversion and Management. 2016;**116**:58-71

[15] Wang C, Abdul-Rahman H, Rao SP. A new design of luminescent solar concentrator and its trial run. International Journal of Energy Research. 2010;**34**(15):1372-1385

[16] Muhammad B, Seung JO, Ng KC, Chun W. Experimental investigation of multijunction solar cell using two axis solar tracker. Applied Mechanics and Materials. 2016;**819**: 536-540. Trans Tech Publications

[17] Burhan M, Shahzad MW, Oh SJ, Ng KC. A pathway for sustainable conversion of sunlight to hydrogen using proposed compact CPV system. Energy Conversion and Management. 2018;**165**:102-112

[18] Garboushian V, Stone KW, Slade A. The Amonix high-concentration photovoltaic system. Concentrator Photovoltaics. 2007;**130**:253

[19] Burhan M, Shahzad MW, Ng KC. Sustainable cooling with hybrid concentrated photovoltaic thermal (CPVT) system and hydrogen energy storage. International Journal of Computational Physics Series. 2018;**1**(2):40-51

[20] Oh SJ, Burhan M, Ng KC, Kim Y, Chun W. Development and performance analysis of a two-axis solar tracker for concentrated photovoltaics. International Journal of Energy Research. 2015;**39**(7):965-976

[21] Burhan M. Theoretical and Experimental Study of Concentrated Photovoltaic (CPV) System with Hydrogen Production as Energy Storage (Doctoral Dissertation); 2015

Chapter 9

Single-Switch Differential Power Processing PWM Converter to Enhance Energy Yield of Photovoltaic Panels under Partial Shading

Masatoshi Uno, Toru Nakane and Toshiki Shinohara

Additional information is available at the end of the chapter

http://dx.doi.org/10.5772/intechopen.74307

Abstract

The partial shading on a photovoltaic (PV) panel consisting of multiple substrings poses serious issues of decreased energy yield and occurrence of multiple maximum power points (MPPs). Although various kinds of differential power processing (DPP) converters have been proposed to prevent the partial shading issues, multiple switches and/or magnetic components in proportion to the number of substrings are necessary, hence increasing the circuit complexity and volume. This chapter proposes a novel single-switch DPP PWM converter to achieve simplified circuit. The proposed DPP converter is essentially the combination of a forward/flyback resonant inverter (FFRI) and voltage multiplier (VM). The fundamental operation analysis is performed, and the current sensorless control strategy suitable for the proposed DPP converter is also discussed. A 30-W prototype of the proposed DPP converter was built, and various kinds of experimental verification tests were performed emulating partial shading conditions. With the proposed DPP converter, local MPPs of a partially shaded PV panel were successfully eliminated, and energy yield was significantly enhanced, demonstrating the efficacy and performance of the proposed DPP converter.

Keywords: differential power processing converter, forward-flyback inverter, partial shading, voltage equalization, voltage multiplier

1. Introduction

Efficient power conversion and high energy utilization are of great importance in photovoltaic (PV) power systems. Efficient power converters and inverters with maximum power point tracking (MPPT) capability have been commercialized to extract as much energy from PV

panels as possible. However, even with such efficient converters, energy yield from PV panels are known to be significantly reduced due to partial shading. A standard PV panel comprising three substrings and its characteristics under a partially shaded condition are shown in **Figure 1**. A shaded substring, PV_3, is less capable of generating current is bypassed by a parallel-connected bypass diode, and therefore, it no longer contributes to power generation, though it can potentially generate power to some extent. In addition, a partially shaded panel exhibits multiple power point maxima including global and local MPPs, which likely confuse ordinally MPPT tracking algorithms.

Partial shading issues originate from characteristic mismatch among series-connected substrings. With differential power processing (DPP) converters, power differences among substrings are transferred so that all substring characteristics are virtually unified, thus precluding the partial shading issues. Various kinds of DPP architectures have been proposed. The most straightforward architecture is the adjacent substring-to-substring equalization system, shown in **Figure 2(a)**, in which adjacent substrings exchange power difference through a DPP converter, depending on shading conditions. Bidirectional converters, such as PWM

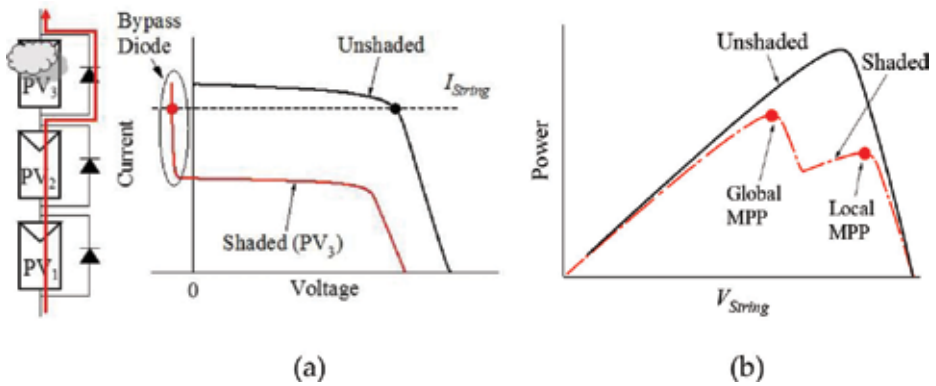

Figure 1. Characteristics of (a) substrings and (b) string under partial shading.

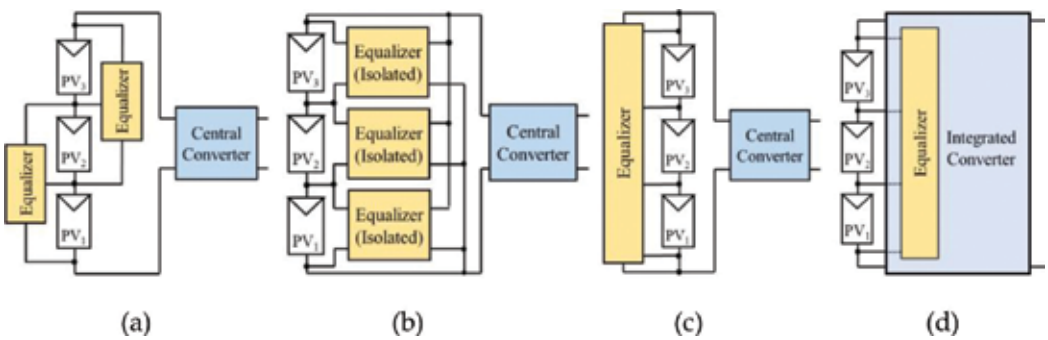

Figure 2. DPP architectures based on (a) adjacent substring-to-substring equalization, (b) substring-to-bus equalization, (c) string-to-substring equalization, and (d) integrated converter.

http://dx.doi.org/10.5772/intechopen.74307

converters [1–3] and switched capacitor converters [4, 5], are used as DPP converters in the adjacent equalization architecture. With the substring-to-bus equalization architecture shown in **Figure 2(b)**, respective bidirectional isolated flyback converter-based DPP converters transfer power between the bus and each substring [6–8]. The architectures in **Figure 2(a)** and **(b)** require multiple DPP converters in proportion to the number of substrings, likely increasing the system complexity and cost. The string-to-substring equalization architecture, on the other hand, can reduce the DPP converter count, as shown in **Figure 2(c)**. Single-input multi-output converters, such as a multi-winding flyback converter [9], multi-stacked buck-boost converters [10, 11], and LLC resonant voltage multiplier [12], can be employed as a DPP converter in this architecture. Integrated converters having a DPP converter function have also been proposed [13, 14]. The simplified system and reduced cost of the integrated converters are appealing features, but the performance as a DPP converter cannot be optimized because two converters are combined into a single unit to form the integrated converter.

From the perspective of the performance and cost, string-to-substring DPP converters are considered the most viable solution to the partial shading issues. Representative circuit topologies of the string-to-substring DPP converters are shown in **Figure 3**. Although the multi-winding flyback converter [9] (**Figure 3(a)**) is very simple as it needs only one switch, the design difficulty of the multi-winding transformer is a top concern. The multi-stacked buck-boost converter-based DPP converter is also a single-switch circuit [10, 11], but it may be bulky as multiple inductors are necessary. From the viewpoint of magnetic components, the DPP converter based on the LLC resonant voltage multiplier (VM) [12] (**Figure 3(c)**) would be the best solution, but the switch count is doubled compared to that of other string-to-substring DPP converters.

A string-to-substring single-switch DPP PWM converter based on the forward-flyback resonant inverter (FFRI) and VM is proposed in this chapter. In addition to the single-switch topology, the magnetic component count is also one, realizing the simple, easy-to-design, and miniaturized circuit. The circuit derivation and description of the proposed single-switch DPP converter are presented in Section 2, followed by the detailed operation analysis in Section 3. The current sensorless control strategy suitable for the proposed single-switch DPP converter

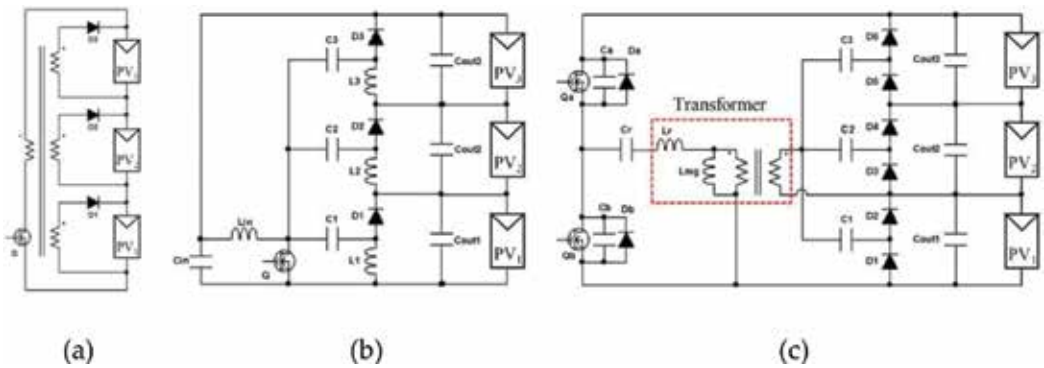

Figure 3. String-to-substring equalizers based on (a) multi-winding flyback converter, (b) multi-stacked buck-boost converters, and (c) LLC resonant voltage multiplier.

will be discussed in Section 4. The experimental results of the laboratory and field testing for a standard 72-cell PV panel consisting of three substrings will be presented in Section 5.

2. Proposed single-switch DPP converter

2.1. Key elements for proposed DPP converter

The proposed string-to-substring DPP converter is essentially the combination of the FFRI and VM, shown in **Figure 4(a)** and **(b)**, respectively. As the switch Q is turned on, the FFRI operates in the forward mode, in which the leakage inductance of the transformer, L_{kg}, resonates with the resonant capacitor C_r placed on the secondary side. At the same time, the magnetizing inductance L_{mg} stores energy. As Q is turned off, the FFRI operates in the flyback mode, and the stored energy in L_{mg} is released to the secondary side. The energy stored in L_{kg} is absorbed in a snubber circuit in order to prevent a voltage spike applied to Q. In summary, AC voltage/current is generated across the secondary winding. The detailed operation analysis will be discussed in Section 3.

The VM basically comprises multiple voltage doublers stacked in series—three voltage doublers, each consisting of a coupling capacitor, diode pair, and a smoothing capacitor, are stacked in **Figure 4(b)**. The VM is driven by AC current/voltage produced by the FFRI. The upper and lower diodes (i.e., the even- and odd-numbered diodes) alternately conduct as AC current/voltage is applied. Voltages of smoothing capacitors C_{out1}–C_{out3} are automatically unified without feedback control, and therefore, voltages of PV substrings that are connected in parallel with respective smoothing capacitors are automatically equalized. Detailed voltage equalization mechanisms can be found elsewhere [12, 14].

2.2. Circuit description of single-switch DPP converter and its features

The proposed single-switch DPP converter for three substrings is shown in **Figure 5**. The output of the FFRI is connected to the input of the VM, and therefore, the VM is driven by AC voltage/current produced by the FFRI [15]. A bias resistor R_{bias} is added to stabilize voltages of the resonant capacitor C_r and coupling capacitors C_1–C_3; C_r and coupling capacitors C_1–C_3 are connected in series, and therefore, their voltages become unstable if without a bias resistor. Although a lossless LCD snubber is employed in **Figure 5**, any snubber circuits, including traditional lossy RCD snubbers, can be used to protect the switch Q. The input of the FFRI is tied to the string, whereas the outputs (i.e., C_{out1}–C_{out3}) of the VM are connected in parallel with respective substrings. Therefore, a fraction of the string power is redistributed to shaded substrings through the proposed DPP converter so that all the substring characteristics are virtually unified even under partial shading conditions.

In addition to the single-switch topology, the magnetic component count is also only one, realizing not only simplified circuit but also miniaturized circuit design. Although the circuit shown in **Figure 5** is for three substrings, the number of substrings can be arbitrarily extended by adding diodes and capacitors in the VM, allowing a flexible design.

http://dx.doi.org/10.5772/intechopen.74307

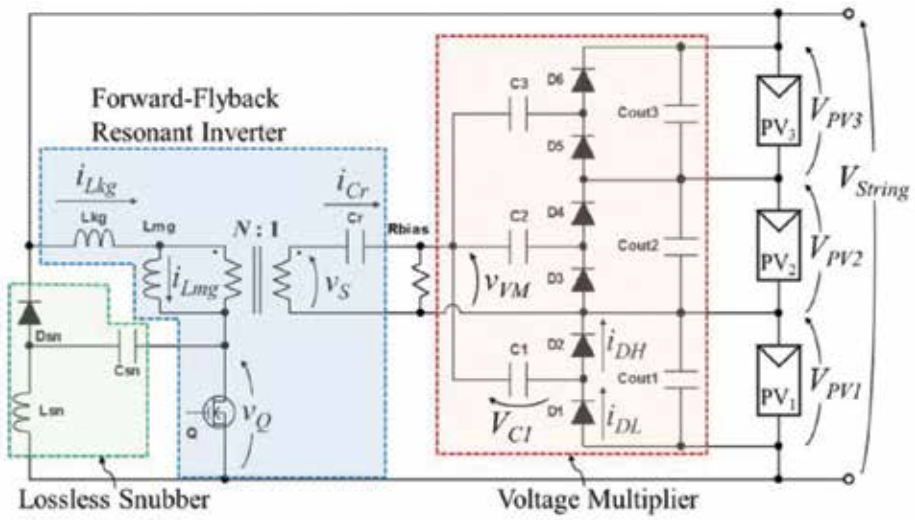

Figure 4. Proposed single-switch DPP PWM converter based on FFRI and VM.

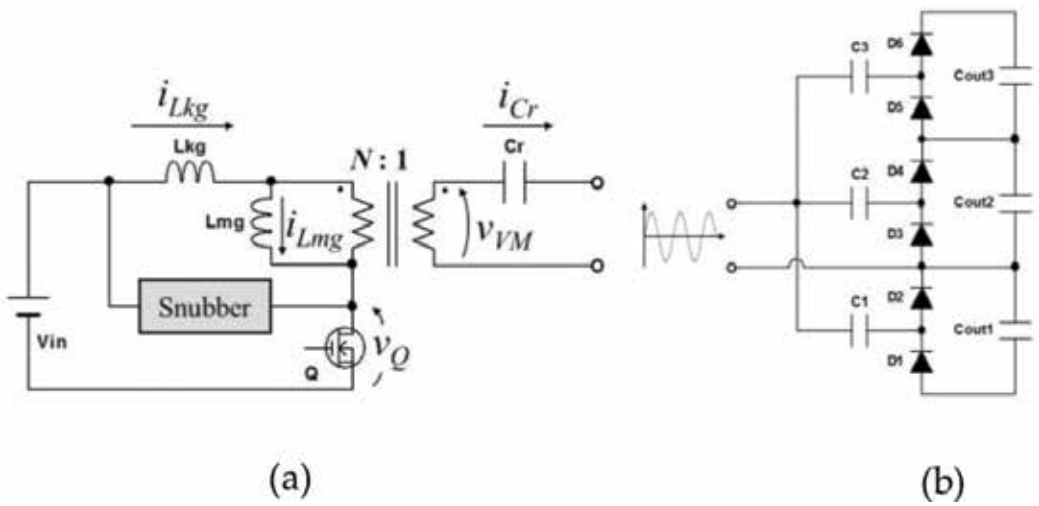

Figure 5. Key elements for proposed single-switch DPP PWM converter: (a) forward-flyback resonant inverter (FFRI) and (b) voltage multiplier (VM).

3. Operation analysis

3.1. Automatic voltage equalization mechanism

As mentioned in Section 2.2, the voltages of substrings are automatically nearly unified with the VM in the proposed DPP converter. The VM is driven by AC voltage/current generated by the FFRI, as illustrated in **Figure 4(b)**. Since capacitors C_1–C_3 are connected to the AC terminal, these

capacitors can be regarded as AC-coupling capacitors that allow AC components only to flow through them. Hence, substrings as well as parallel-connected voltage doublers, each comprising diode pairs and a coupling capacitor, can be equivalently separated and grounded, as shown in **Figure 6**. All the substrings with respective voltage doublers in this equivalent circuit are connected in parallel, and therefore, AC current preferentially flows through a voltage doubler that is connected to a shaded substring whose voltage tends to be lower than the others.

3.2. Operation principle

This section discusses the operation analysis in the case that PV_1 is partially shaded. The proposed DPP converter operates either in continuous conduction mode (CCM) or discontinuous conduction mode (DCM). The DCM operation, which contains more operation modes, is discussed in this section. Key operation waveforms and current flow directions are shown in **Figures 7** and **8**, respectively. The lossless snubber is depicted as a voltage source V_{sn} with a diode D_{sn}, in **Figure 8**, for the sake of clarity.

The average voltage of C_r is zero thanks to R_{bias} and the transformer secondary winding whose average voltage must be zero under steady-state conditions. Hence, the input voltage of the VM, v_{VM}, is nearly identical to the voltage of secondary winding, v_S.

Mode 1 (T_0–T_1) (**Figure 8(a)**): The switch Q is turned on, and the DPP converter operates in the forward mode. The current of L_{mg}, i_{Lmg}, starts linearly increasing from zero, as

$$i_{Lmg} = \frac{V_{string}}{L_{mg} + L_{kg}}(t - T_0) \tag{1}$$

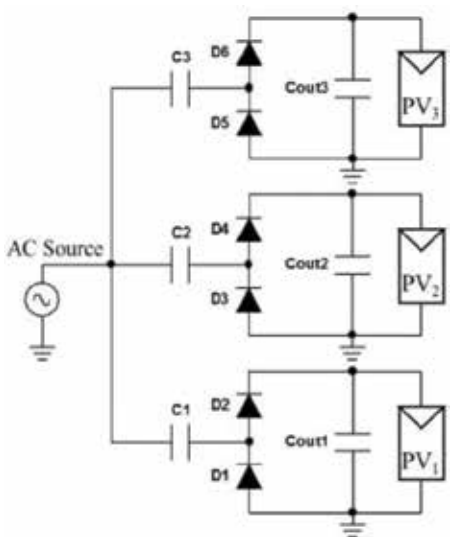

Figure 6. Equivalent circuit of voltage multiplier.

http://dx.doi.org/10.5772/intechopen.74307

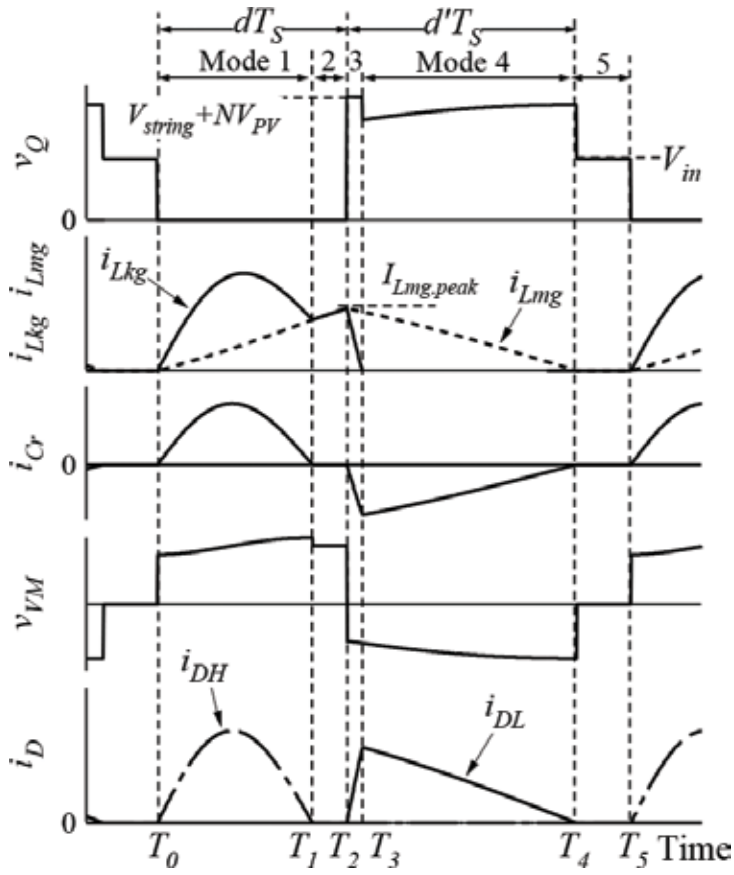

Figure 7. Key operation waveforms when PV_1 is partially shaded.

Meanwhile, L_{kg} resonates with C_r on the secondary winding, and sinusoidal current i_{Cr} flows;

$$i_{Cr} = \frac{\frac{V_{string}}{N} - V_{VM.O}}{|Z_r|} \sin \omega_r (t - T_0) \tag{2}$$

where Z_r and ω_r are the characteristic impedance of the resonant tank and resonant angular frequency given by

$$Z_r = N\sqrt{\frac{L_{kg}}{C_r}}, \omega_r = 2\pi f_r = \frac{N}{\sqrt{L_{kg}C_r}} \tag{3}$$

The current of L_{kg}, i_{Lkg}, is equal to the sum of i_{Lmg} and i_{Cr} reflected on the primary side. In the VM, the upper diode corresponding to PV_1, D_2, conducts whereas other diodes are off. Since the voltage of C_r can be approximated to be zero, v_{VM} during the even-numbered diodes are on, $V_{VM.E}$, is given by

$$V_{VM.E} = V_{C1} + V_f = \frac{L_{mg} V_{string}}{N(L_{kg} + L_{mg})} \tag{4}$$

As i_{Cr} reaches zero, this mode ends, and the operation moves to the next mode.

Mode 2 (T_1–T_2) (**Figure 8(b)**): Q is still on, but all resonant currents become zero. Since i_{Cr} is zero, i_{Lkg} is identical to i_{Lmg}. No current flows in the VM, except for the current from the smoothing capacitor C_{out1} to PV_1. In order for Mode 2 to exist, Mode 1 must be longer than half the resonant period. Hence, the following equation needs to be satisfied;

$$d \geq \frac{f_S}{2f_r} \tag{5}$$

where d is the duty cycle of Q. The peak value of i_{Lmg} at the end of this mode, $I_{Lmg.peak}$ is

$$I_{Lmg.peak} = \frac{V_{string} d T_S}{L_{mg} + L_{kg}} \tag{6}$$

Mode 3 (T_2–T_3) (**Figure 8(c)**): Q is turned off, and the DPP converter starts operating in the flyback mode. The energy stored in L_{kg} in Modes 1 and 2 is absorbed by the snubber. Meanwhile,

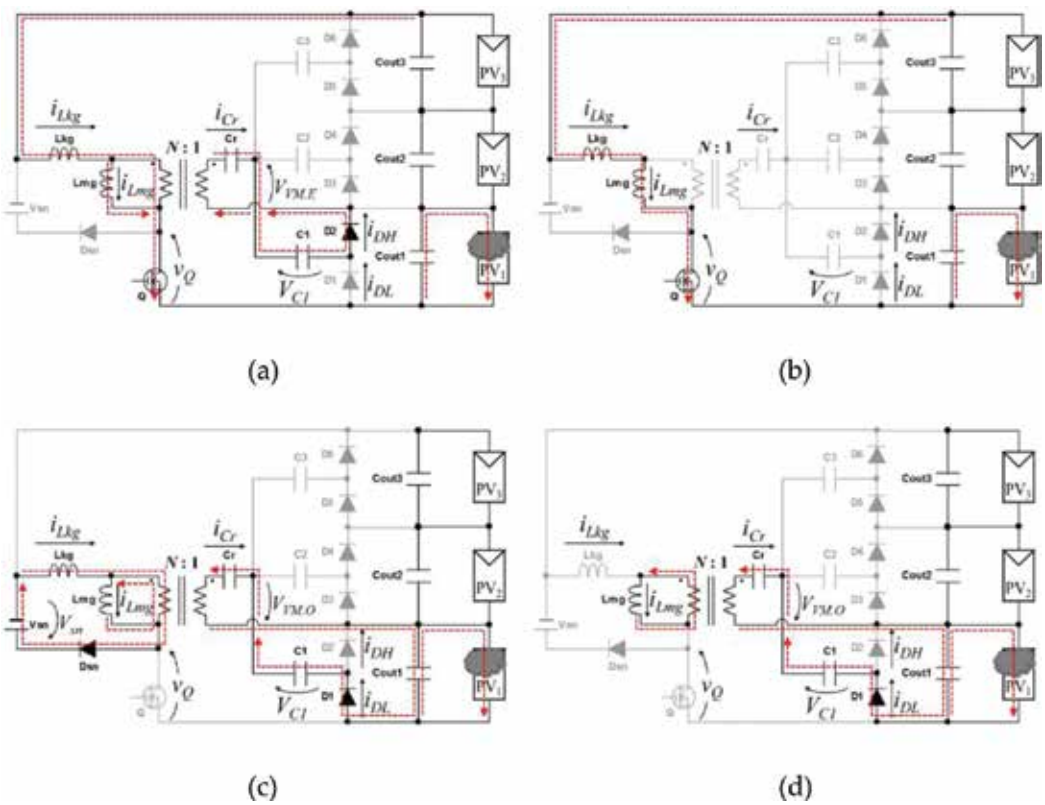

Figure 8. Current flow directions in (a) mode 1, (b) mode 2, (c) mode 3, and (d) mode 4.

i_{Lmg} begins to decrease as L_{mg} starts releasing its energy stored in the first two modes. i_{Lmg} is transferred to the secondary side, and the lower diode corresponding to PV_1, D_1, conducts. This mode ends as i_{Lkg} becomes zero—the length of this mode is practically very short compared to other modes.

Mode 4 (T_3–T_4) (**Figure 8(d)**): i_{Lmg} keeps decreasing, and its energy is released to the secondary side. i_{Lmg} in this mode is expressed as

$$i_{Lmg} = I_{Lmg.peak} - \frac{NV_{VM.E}}{L_{mg}}(t - T_3) \tag{7}$$

v_{VM} during odd-numbered diodes are on, $V_{VM.O}$, is expressed using (4) as

$$V_{VM.O} = V_{PV1} + V_f - V_{C1} = V_{PV1} + 2V_f - \frac{L_{mg}V_{stringmg}}{N(L_{kg} + L_{mg})} \tag{8}$$

The duty cycle of Mode 4, $d' = (T_3–T_4)/T_S$, is

$$d' = \frac{dV_{string}}{N(V_{PV1} + 2V_f)\frac{L_{mg}+L_{kg}}{L_{mg}} - V_{string}} \tag{9}$$

If the operation meets $d' < (1 - d)$, the DPP converter operates in DCM. The critical duty cycle for DCM operation, $d_{critical}$, is given by

$$d_{critical} < 1 - \frac{V_{string}L_{mg}}{N(L_{mg} + L_{kg})(V_{PV1} + 2V_f)} \tag{10}$$

Mode 5 (T_4–T_5) (not shown): This mode is unique to the DCM operation. No currents flow in the DPP converter, except for C_{out1} providing a current to the shaded substring PV_1.

In summary, the upper and lower diodes that are connected in parallel with the shaded substring alternately conduct. The shaded substring PV_1 receives the current from the DPP converter, whereas no current flows toward unshaded substrings.

Since the average voltage of C_r is nearly zero, v_{VM} can be assumed equal to v_S. Based on volt-second balance on the transformer secondary winding with Eqs. (4) and (8), the voltage conversion ratio of the proposed DPP converter in DCM can be yielded as

$$V_{PV1} = \frac{L_{mg}V_{string}(d + d')}{Nd'(L_{kg} + L_{mg})} - 2V_f \tag{11}$$

The voltage conversion ratio in CCM can be obtained by applying $d' = 1 – d$ into (11), as

$$V_{PV1} = \frac{L_{mg}V_{string}}{N(1 - d)(L_{kg} + L_{mg})} - 2V_f \tag{12}$$

Eqs. (11) and (12) suggest that the voltage conversion ratio is PWM-controllable, and d should be properly adjusted depending on the degree of shading. The control strategy suitable for the proposed DPP PWM converter is discussed in the next section.

4. Control strategy

There is only one single switch in the proposed DPP converter, whereas it has three outputs for PV_1–PV_3. Hence, the DPP converter needs to be properly controlled so that shaded substrings only receive a current from the DPP converter while no currents flow toward unshaded ones. To this end, the current sensorless ΔV-controlled equalization strategy [11] is employed.

The mechanism of the ΔV-controlled equalization is illustrated in **Figure 9(a)**. The proposed single-switch DPP converter can be equivalently depicted as a single-input multi-output converter with V_e and blocking diodes. Based on the ΔV-controlled equalization, the DPP converter is operated so that the voltage difference among substrings $\Delta V = V_H - V_L$ (where V_H and V_L are the highest and lowest substring voltages, respectively) is controlled to be a non-zero positive value. In this scenario, the DPP converter supplies the equalization current only for the shaded substring PV_1 whose voltage is equal to the output voltage of the DPP converter V_e. Meanwhile, unshaded substrings' voltages are higher than V_e, and therefore, currents do not flow toward them.

The control block diagram of the ΔV-controlled equalization is illustrated in **Figure 9(b)**. All the substring voltages are individually measured to calculate ΔV. The reference of ΔV, ΔV_{ref}, is set to be slightly greater than zero to be unaffected by noise.

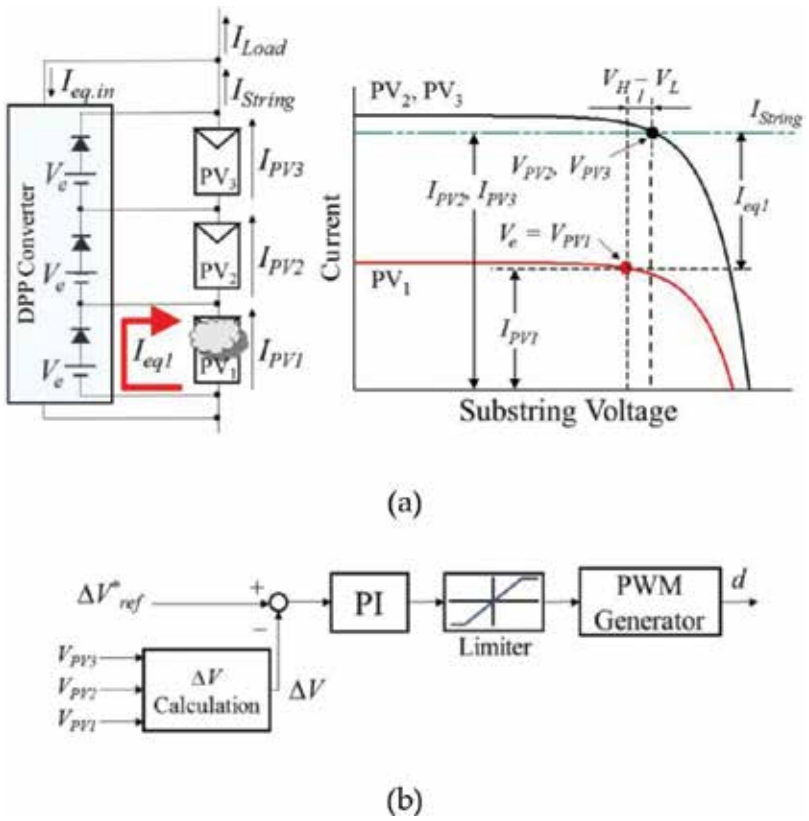

Figure 9. (a) Mechanism and (b) block diagram of ΔV-controlled equalization.

http://dx.doi.org/10.5772/intechopen.74307

5. Experimental results

5.1. Prototype

A 30-W prototype of the proposed single-switch DPP converter for standard 72-cell PV panels comprising three substrings was built, as shown in **Figure 10**. **Table 1** enlists the circuit elements used for the prototype. The prototype was operated at a switching frequency of 100 kHz, and a TMS320F28335 control card (Texas Instruments) was used to implement the ΔV-controlled equalization.

5.2. Fundamental performance

Key operation waveforms and power conversion efficiency were measured using the experimental setup shown in **Figure 11**. All substrings were removed, and the DPP converter was

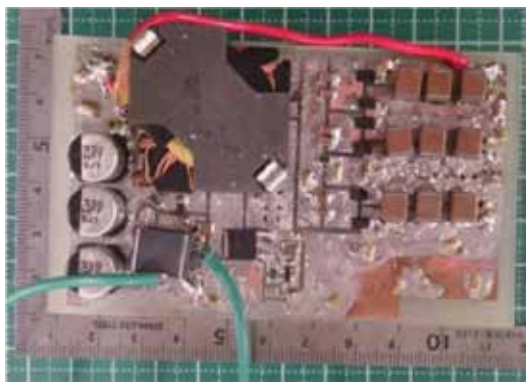

Figure 10. Photograph of the 30-W prototype.

Element	Value
Q	F390N15A, R_{on} = 33.5 mΩ
C_1–C_3	Ceramic Capacitor, 94 µF
C_{out1}–C_{out3}	Ceramic Capacitor, 300 µF
D_1–D_6	Schottkey Diode, V_f = 0.3 V
C_r	Ceramic Capacitor, 20 µF
Transformer	N_1:N_2 = 10:2, L_{kg} = 2 µH, L_{mg} = 450 µH
Snubber	C_{sn} = 2.2 µF, L_{sn} = 1 mH

Table 1. Circuit element list.

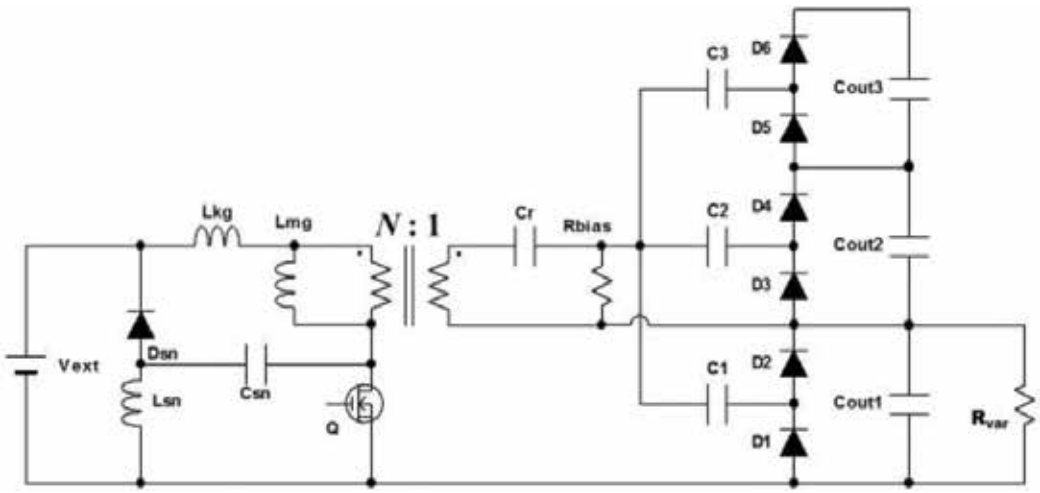

Figure 11. Experimental setup for waveform and efficiency measurement.

powered by an external power supply V_{ext}. A variable resistor R_{var} was connected to C_{out1} in order to emulate current flow directions under the PV_1-shaded condition shown in **Figure 8**.

The measured key operation waveforms in DCM are shown in **Figure 12**. Although oscillations due to the resonance between the output capacitance of the MOSFET and L_{mg} were observed in v_Q and v_{VM}, the measured waveforms matched well with the theoretical ones shown in **Figure 7**. The measured power conversion efficiency is shown in **Figure 13**. In the

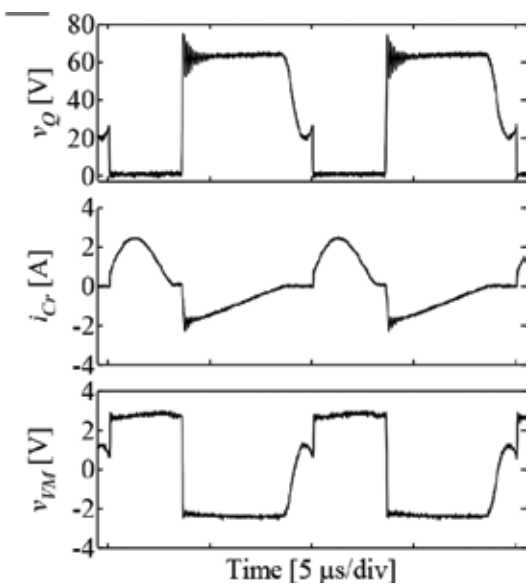

Figure 12. Measured key operation waveforms when PV_1 is partially shaded.

http://dx.doi.org/10.5772/intechopen.74307

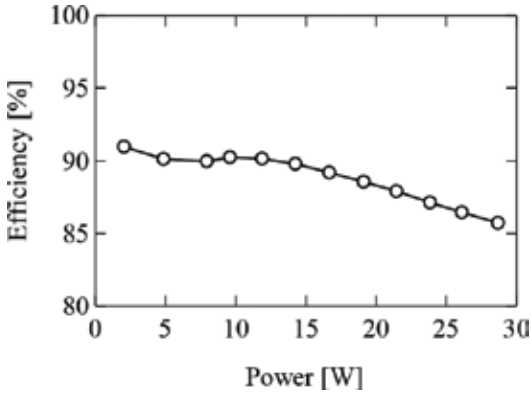

Figure 13. Measured power conversion efficiency.

light load region, the DPP converter operated in DCM and its efficiency was around 90%. The heavy load region corresponded to CCM, in which the efficiency gradually declined due to the increased Joule loss.

5.3. Laboratory testing

Solar array simulators (E4361A, Keysight Technologies) were used to emulate shaded and unshaded PV substring characteristics, as shown in **Figure 14(a)**. The short circuit current of the shaded substring PV_1 was set to be half that of unshaded substrings. String characteristics as a whole were manually swept using an electronic load operating in the resistance mode. The

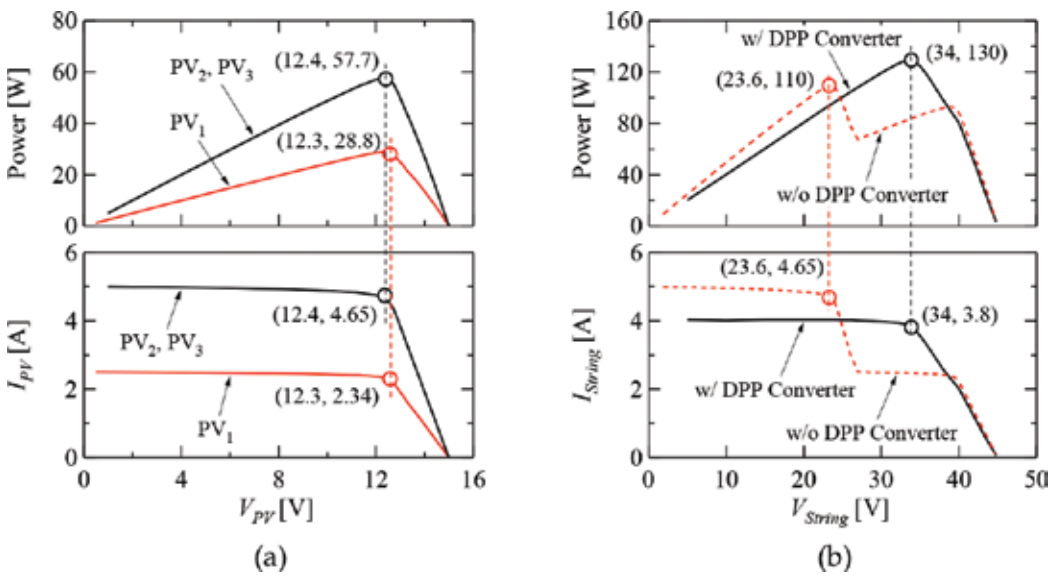

Figure 14. (a) Individual PV substring characteristics and (b) string characteristics with and without DPP converter.

ΔV-controlled equalization with ΔV_{ref} = 1.0 V was implemented. As a reference, the string characteristic without the proposed DPP converter was also measured.

Measured string characteristics with and without the DPP converter are shown and compared in **Figure 14(b)**. Without the DPP converter, two MPPs were observed, and the maximum power was merely 110 W at V_{string} = 23.6 V. With the proposed DPP converter, on the other hand, the local MPP disappeared, and maximum power increased to as high as 130 W at V_{string} = 34.0 V, corresponding to 18.2% improvement. Thus, the experimental results demonstrated the proposed DPP converter drastically increases the power yield from a partially shaded string.

The prototype of the proposed DPP converter was operated in conjunction with a commercial MPPT converter (SS-MPPT-15 L, Morningstar) to demonstrate its compatibility. The measured V_{string} and extracted power are shown in **Figure 15**. The MPPT converter periodically swept the string characteristic in search for the global MPP location and subsequently kept extracting the maximum power of approximately 130 W.

5.4. Field testing

The field test using a real PV panel was also performed emulating a partial shading condition, as shown in **Figure 16**. A standard 72-cell monocrystalline PV panel was used for the experiment, and one of the substrings was covered with a postcard to emulate a partial shading condition. The irradiance in the field test was measured using a pyranometer. The measured string characteristics with and without the proposed DPP converter prototype are shown in **Figure 17**. Without the DPP converter, two power maxima were observed, and the extractable maximum power was approximately 39 W at the irradiance level of 372 W/m^2. With the DPP converter, the maximum power increased to as high as 46.1 W, in spite of the lower irradiance level of 356 W/m^2.

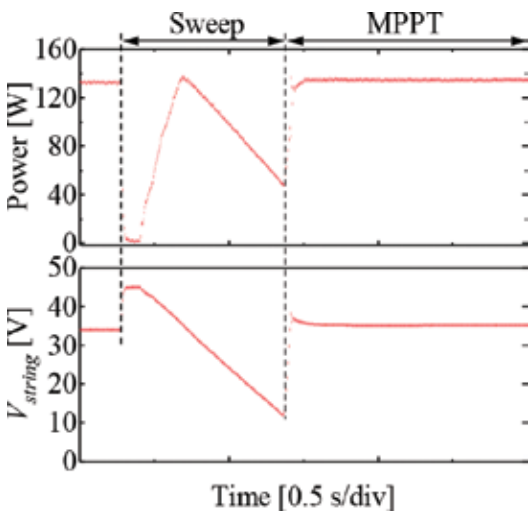

Figure 15. Measured power conversion efficiency.

http://dx.doi.org/10.5772/intechopen.74307

Figure 16. Field test setup.

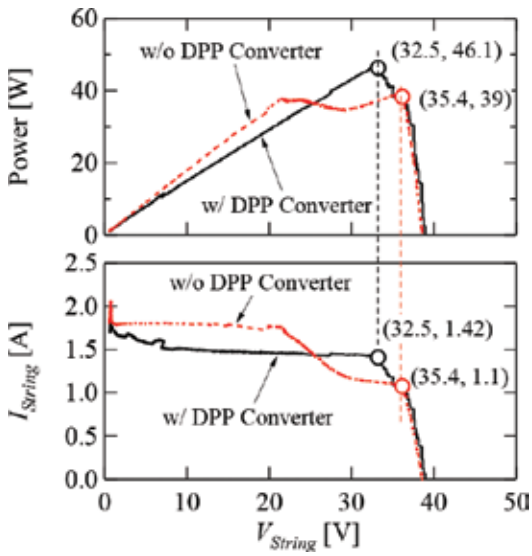

Figure 17. String characteristics with and without DPP converter in the field test.

6. Conclusions

The single-switch DPP PWM converter to preclude the partial shading issues has been proposed in this chapter. The proposed DPP converter can be derived by integrating the FFRI and VM into a single unit. The switch count of the proposed DPP converter is only one, thus achieving the simplified circuit. The operation analysis was performed, and the voltage conversion ratios in DCM and CCM were mathematically yielded.

The 30-W prototype of the proposed DPP converter was built, and its fundamental operation performance was measured. Experimental equalization tests emulating partial shading conditions were performed using solar array simulators or a real PV panel. With the prototype of the proposed DPP converter, local MPPs disappeared, and extractable maximum powers significantly increased, demonstrating the efficacy and performance of the proposed DPP converter.

Author details

Masatoshi Uno*, Toru Nakane and Toshiki Shinohara

*Address all correspondence to: masatoshi.uno.ee@vc.ibaraki.ac.jp

Ibaraki University, Hitachi, Japan

References

[1] Bergveld HJ, Büthker D, Castello C, Doorn T, Jong AD, Otten RV, Waal KD. Module-level dc/dc conversion for photovoltaic systems: The delta-conversion concept. IEEE Transactions on Power Electronics. 2013;**28**:2005-2013. DOI: 10.1109/TPEL.2012.2195331

[2] Shenoy PS, Kim KA, Johnson BB, Krein PT. Differential power processing for increased energy production and reliability of photovoltaic systems. IEEE Transactions on Power Electronics. 2013;**28**:2968-2979. DOI: 10.1109/TPEL.2012.2211082

[3] Shimizu T, Hashimoto O, Kimura G. A novel high-performance utility-interactive photovoltaic inverter system. IEEE Transactions on Power Electronics. 2003;**18**:704-711. DOI: 10.1109/TPEL.2003.809375

[4] Stauth JT, Seeman MD, Kesarwani K. Resonant switched capacitor converters for submodule distributed photovoltaic power management. IEEE Transactions on Power Electronics. 2013;**28**:1189-1198. DOI: 10.1109/TPEL.2012.2206056

[5] Chang AH, Avestruz AT, Leeb SB. Capacitor-less photovoltaic cell-level power balancing using diffusion charge redistribution. IEEE Transactions on Power Electronics. 2015;**30**: 537-546. DOI: 10.1109/TPEL.2014.2340403

[6] Olalla C, Clement D, Rodríguez M, Makisimović D. Architectures and control of submodule integrated dc-dc converters for photovoltaic applications. IEEE Transactions on Power Electronics. 2013;**28**:2980-2997. DOI: 10.1109/TPEL.2012.2219073

[7] Jeon YT, Lee H, Kim KA, Park JH. Least power point tracking method for photovoltaic differential power processing systems. IEEE Transactions on Power Electronics. 2017;**32**: 1941-1951. DOI: 10.1109/TPEL.2016.2556746

[8] Chua G, Wena H, Jiangb L, Hub Y, Lia X. Bidirectional flyback based isolated-port submodule differential power processing optimizer for photovoltaic applications. Solar Energy. 2017;**158**:929-940. DOI: 10.1016/j.solener.2017.10.053

[9] Du J, Xu R,Chen X, Li Y ,Wu J. A novel solar panel optimizer with self-compensation for partial shadow condition. In: Proceedings of the IEEE Applied Power Electronics Conference and Exposition. (APEC); 27 May 2013; Long Beach. California: IEEE; 2013. p. 92-96

[10] Uno M, Kukita A. Single-switch voltage equalizer using multi-stacked buck–boost converters for partially-shaded photovoltaic modules. IEEE Transactions on Power Electronics. 2015;**30**:3091-3105. DOI: 10.1109/TPEL.2014.2331456

[11] Uno M, Kukita A. Current sensorless equalization strategy for a single-switch voltage equalizer using multistacked buck–boost converters for photovoltaic modules under partial shading. IEEE Transactions on Industry Applications. 2017;**53**:420-429. DOI: 10.1109/TIA.2016.2615022

[12] Uno M, Kukita A. Two-switch voltage equalizer using an LLC resonant inverter and voltage multiplier for partially shaded series connected photovoltaics modules. IEEE Transactions on Industry Applications. 2015;**51**:1587-1601. DOI: 10.1109/TIA.2014.2336980

[13] Uno M, Kukita A. PWM converter integrating switched capacitor converter and series-resonant voltage multiplier as equalizers for photovoltaic modules and series-connected energy storage cells for exploration rovers. IEEE Transactions on Power Electronics. 2017; **32**:8500-8513. DOI: 10.1109/TPEL.2016.2645705

[14] Uno M, Kukita A. Single-switch single-magnetic PWM converter integrating voltage equalizer for partially-shaded photovoltaic modules in standalone applications. IEEE Transactions on Power Electronics. 2018;**33**:1259-1270. DOI: 10.1109/TIA.2014.2336980

[15] Uno M, Kukita A. Single-switch single transformer cell voltage equalizer based on forward–flyback resonant inverter and voltage multiplier for series-connected energy storage cells. IEEE Transactions on Vehicular Technology. 2014;**63**:4232-4246. DOI: 10.1109/TVT.2014. 2312381

Edited by Beddiaf Zaidi

Despite their wide availability and relatively low prices, the conventional energy sources have harmful consequences on the environment and are exhaustible. In order to circumvent these negative effects, the renewable energies in general and the photovoltaic energy in particular are becoming more and more attractive. Solar cell is an electrical device that converts light into electricity at the atomic level. These devices use inorganic or organic semiconductor materials that absorb photons with energy greater than their bandgap to promote energy carriers into their conduction band. They do not pollute the atmosphere by releasing harmful gases, do not require any fuel to produce electricity, and do not move parts so they are rugged. Solar panels have a very long life and do not need much maintenance.

Published in London, UK

IntechOpen

ISBN 978-1-83881-647-6